NASA/TP–2015-218785

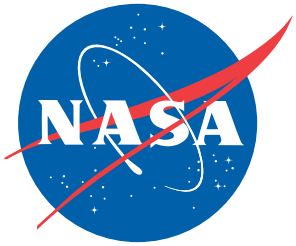

Buckling Test Results from the 8-Foot-Diameter Orthogrid-Stiffened Cylinder Test Article TA01

Test Dates: 19–21 November 2008

Mark W. Hilburger
Langley Research Center, Hampton, Virginia

W. Allen Waters, Jr.
Analytical Mechanics Associates, Inc., Hampton, Virginia

Waddy T. Haynie
Langley Research Center, Hampton, Virginia

August 2015

NASA STI Program . . . in Profile

Since its founding, NASA has been dedicated to the advancement of aeronautics and space science. The NASA scientific and technical information (STI) program plays a key part in helping NASA maintain this important role.

The NASA STI program operates under the auspices of the Agency Chief Information Officer. It collects, organizes, provides for archiving, and disseminates NASA's STI. The NASA STI program provides access to the NTRS Registered and its public interface, the NASA Technical Reports Server, thus providing one of the largest collections of aeronautical and space science STI in the world. Results are published in both non-NASA channels and by NASA in the NASA STI Report Series, which includes the following report types:

- TECHNICAL PUBLICATION. Reports of completed research or a major significant phase of research that present the results of NASA Programs and include extensive data or theoretical analysis. Includes compilations of significant scientific and technical data and information deemed to be of continuing reference value. NASA counter-part of peer-reviewed formal professional papers but has less stringent limitations on manuscript length and extent of graphic presentations.

- TECHNICAL MEMORANDUM. Scientific and technical findings that are preliminary or of specialized interest, e.g., quick release reports, working papers, and bibliographies that contain minimal annotation. Does not contain extensive analysis.

- CONTRACTOR REPORT. Scientific and technical findings by NASA-sponsored contractors and grantees.

- CONFERENCE PUBLICATION. Collected papers from scientific and technical conferences, symposia, seminars, or other meetings sponsored or co-sponsored by NASA.

- SPECIAL PUBLICATION. Scientific, technical, or historical information from NASA programs, projects, and missions, often concerned with subjects having substantial public interest.

- TECHNICAL TRANSLATION. English-language translations of foreign scientific and technical material pertinent to NASA's mission.

Specialized services also include organizing and publishing research results, distributing specialized research announcements and feeds, providing information desk and personal search support, and enabling data exchange services.

For more information about the NASA STI program, see the following:

- Access the NASA STI program home page at *http://www.sti.nasa.gov*

- E-mail your question to help@sti.nasa.gov

- Phone the NASA STI Information Desk at 757-864-9658

- Write to:
  NASA STI Information Desk
  Mail Stop 148
  NASA Langley Research Center
  Hampton, VA 23681-2199

NASA/TP–2015-218785

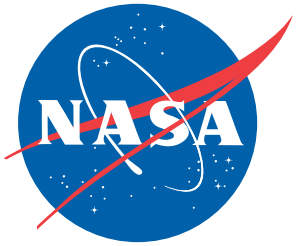

Buckling Test Results from the 8-Foot-Diameter Orthogrid-Stiffened Cylinder Test Article TA01

Test Dates: 19–21 November 2008

Mark W. Hilburger
Langley Research Center, Hampton, Virginia

W. Allen Waters, Jr.
Analytical Mechanics Associates, Inc., Hampton, Virginia

Waddy T. Haynie
Langley Research Center, Hampton, Virginia

National Aeronautics and
Space Administration

Langley Research Center
Hampton, Virginia 23681-2199

August 2015

Available from:

NASA Center for AeroSpace Information
7115 Standard Drive
Hanover, MD 21076-1320
443-757-5802

Preface

The Shell Buckling Knockdown Factor (SBKF) Project was established in the spring of 2007 by the NASA Engineering and Safety Center with the goal of developing improved (i.e., less-conservative, more robust), analysis-based shell buckling design factors (a.k.a. knockdown factors) for modern launch-vehicle structures. Preliminary design studies indicated that implementation of these new knockdown factors could help mitigate some of NASA's future launch vehicle development and performance risks by improving baseline designs, providing high-fidelity estimates of structural performance, reducing reliance on testing, and enabling increased payload capability. To this end, the SBKF project has been engaged in several technical work areas to support the development, validation, and implementation of the new design factors, including subscale and full-scale structural testing. The primary objectives of the test program are to:

1. Provide validation data for high-fidelity structural analysis models and new design knockdown factors.
2. Verify the performance and behavioral characteristics of a variety of buckling-critical structural designs subjected to relevant loading conditions.
3. Determine the effects of common structural details such as weld lands and joints on the buckling response.
4. Understand the effects of scale-up from subscale to full-scale on the buckling response.

To meet these objectives, tests on nine different subscale 8-foot-diameter, integrally stiffened aluminum-alloy barrels were planned in order to obtain the majority of the required validation data along with two full-scale, 27.5-foot-diameter, aluminum-lithium, integrally stiffened test articles to determine structural scaling trends. Data from these tests and the corresponding pretest analysis predictions and data archival information will be summarized in a series of NASA technical publications. The pretest predictions presented in these test reports were used to determine the testing and instrumentation requirements and are included for reference. Detailed test and analysis correlation will be presented in a separate series of NASA technical publications in which refined modeling and analysis results will be discussed thoroughly.

Table of Contents

List of Figures

List of Tables

Nomenclature

Symbols

δ_{D263AA}	measured displacement: subscript corresponds to specific LVDT channel
imp	measured geometric imperfection
L	cylinder length
M_{cr}	predicted linear bifurcation buckling load of a cylinder subjected to a bending moment
P	axial load
P_{cr}	predicted linear bifurcation buckling load of a compression-loaded cylinder
R	cylinder OML radius
r_u, r_v, r_w	rotations about the *x, θ, z axis*
u, v, w	axial, circumferential, and radial displacements
x, θ, z	axial, circumferential, and radial coordinate of a cylindrical coordinate system
$\mu\varepsilon$	microstrain or 1.0e-6 strain

Orthogrid design variables	See Figure 2.2
b_r	circumferential stiffener (ring) spacing
b_s	axial stiffener (stringer) spacing
h	stiffener height measured from the IML
H	stiffener height measured from the OML ($H = h + t$)
t	shell wall skin thickness
t_{eff}	effective shell wall thicknesses value
t_r	circumferential stiffener (ring) thickness
t_s	axial stiffener (stringer) thickness

Acronyms

2D	Two Dimensional
3D	Three Dimensional
Al-Li	Aluminum Lithium Alloy
CSS	Central Storage System
DAS	Data Acquisition System
DIC	Digital Image Correlation
EDI	Electronic Displacement Indicator
ET	External Tank
EU	Engineering Units
FOV	Field(s) of View
IML	Inner Mold Line (inner surface of structure)

IRIG	Inter-range Instrumentation Group
LaRC	Langley Research Center
LCS	Load Control System
LPS	Load Point Scans
LTA	Load Test Annex
LVDT	Linear Voltage Displacement Transducer (type of EDI)
MSFC	Marshall Space Flight Center
NESC	NASA Engineering and Safety Center
NSCKN	NASA Safety Center Knowledge Now
OML	Outer Mold Line (outer surface of structure)
SBKF	Shell Buckling Knockdown Factor
SLTMAS	Structural Loads Test Measurement Acquisition System
STAGS	STructural Analysis of General Shells
TA01	Cylinder Test Article SBKF-P2-CYL-TA01

Abstract

Results from the testing of cylinder test article SBKF-P2-CYL-TA01 (referred to herein as TA01) are presented. The testing was conducted at the Marshall Space Flight Center (MSFC), November 19–21, 2008, in support of the Shell Buckling Knockdown Factor (SBKF) Project.[i] The test was used to verify the performance of a newly constructed buckling test facility at MSFC and to verify the test article design and analysis approach used by the SBKF project researchers. TA01 is an 8-foot-diameter (96-inches), 78.0-inch-long, aluminum-lithium (Al-Li), orthogrid-stiffened cylindrical shell similar to those used in current state-of-the-art launch-vehicle structures and was designed to exhibit global buckling when subjected to compression loads. Five different load sequences were applied to TA01 during testing and included four sub-critical load sequences, i.e., loading conditions that did not cause buckling or material failure, and one final load sequence to buckling and collapse. The sub-critical load sequences consisted of either uniform axial compression loading or combined axial compression and bending and the final load sequence subjected TA01 to uniform axial compression. Traditional displacement transducers and strain gages were used to monitor the test article response at nearly 300 locations and an advanced digital image correlation system was used to obtain low-speed and high-speed full-field displacement measurements of the outer surface of the test article. Overall, the test facility and test article performed as designed. In particular, the test facility successfully applied all desired load combinations to the test article and was able to test safely into the postbuckling range of loading, and the test article failed by global buckling. In addition, the test results correlated well with initial pretest predictions.

1.0 Introduction

Results from the testing of cylinder test article SBKF-P2-CYL-TA01 (referred to herein as TA01) are presented. TA01 was the first in a series of nine subscale 8-foot-diameter, integrally stiffened cylindrical shells to be tested in the Shell Buckling Knockdown Factor project (SBKF) test program. The test was conducted at the Marshall Space Flight Center (MSFC), November 19–21, 2008. TA01 is an 8-foot-diameter (96-inches), 78.0-inch-long, aluminum-lithium (Al-Li), orthogrid-stiffened cylindrical shell similar to those used in current state-of-the-art launch-vehicle structures and was designed to exhibit global buckling when subjected to compression loads. The primary objectives of this test were to verify the performance of the test facility, the test procedures, and the test article design and analysis approach.

First, descriptions of the test article design, fabrication, and test are given in Section 2, and modeling and analysis methods used in support of the test article design and testing activities are described briefly in Section 3. Then, selected test results are presented and compared to pretest

[i] NASA Engineering and Safety Center (NESC) Assessment #: 07-010-E

predictions in Section 4, and concluding remarks are presented in Section 5. Finally, a complete listing of all test and analysis data, data files and drawings is provided in Appendix A. The listing includes archival directory names, file names, and file format descriptions. All references used to support the test are also provided and include test article design drawings, test article fabrication and test plans and procedures, and pretest analysis results.

2.0 Test Description

Cylinder test article TA01 was designed by SBKF project researchers at NASA Langley Research Center (LaRC) and was fabricated by the MSFC Metal Joining and Processing Branch (EM32). The testing of TA01 occurred on November 19–21, 2008 at MSFC in Building 4619 Load Test Annex (LTA) under the direction of the Structural Strength Test Group (ET30). A special-purpose test apparatus was designed and fabricated for this test effort. The test apparatus was designed to apply up to 1.5 million pounds of force in axial compression and bending and 10 psi internal pressure. A multi-channel load control system was used to apply the test loads and included load control and displacement control options. Traditional strain and displacement data were obtained from 294 locations on the test article and full-field displacement data were obtained on the test article outer mold line (OML) by using low-speed and high-speed digital image correlation systems. This section gives a brief overview of the test objectives, test article, instrumentation, test facility, and test load cases. Additional details on the testing of TA01 can be found in the test plan and test procedure (Refs. 1 and 2).

2.1 Test Objectives

Testing of TA01 was designed to provide data necessary to verify the test apparatus performance and the test article design approach with the following objectives:

1. Verify the operation and performance of the test system. Specifically, verify the adequacy of the test procedures, verify instrumentation, and low-speed and high-speed digital image correlation (DIC) systems and measurements, and assess test article/test fixture designs.
2. Obtain test data necessary to verify the test article design and analysis approach through detailed test and analysis correlation.

2.2 Test Article Design

TA01 is an 8-foot-diameter (96-inches), 78.0-inch-long, orthogrid-stiffened cylindrical shell and is constructed from three 2195 Al-Li integrally stiffened curved-panel segments (120° arc segments) that were friction-stir welded together to form a complete cylinder. The test article included similar design features and had similar response characteristics as those found in current state-of-the-art launch-vehicle tank structures in an effort to maximize the applicability of the test data to the design of modern launch vehicles. A post-test photo of TA01 is shown in Fig. 2.1. The internal grid pattern shown in the photo, comprised of the internal axial and circumferential stiffeners, is referred to herein as an orthogrid pattern.

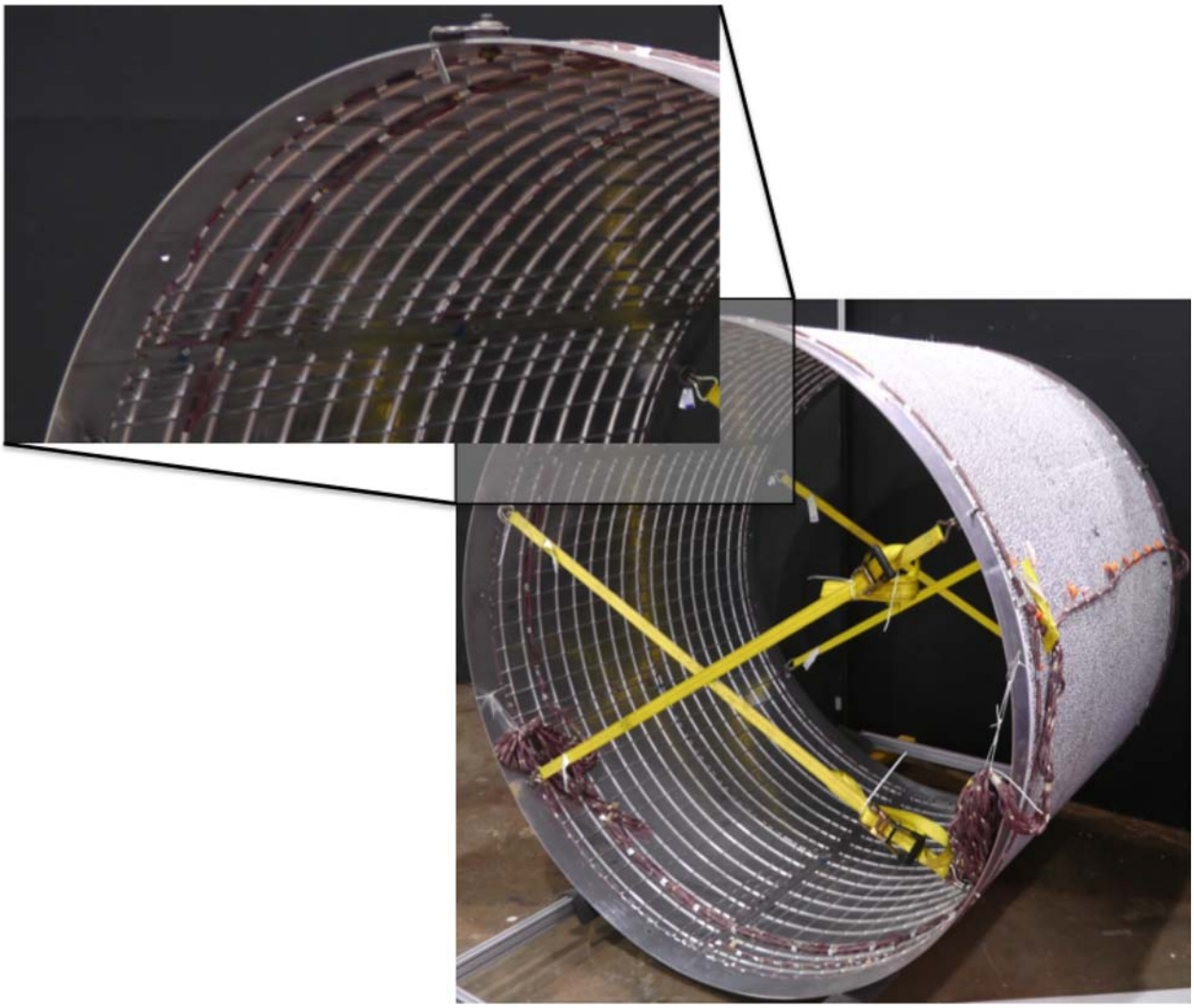

Figure 2.1. Al-Li orthogrid-stiffened cylinder test article, TA01 (post-test).

One of the primary objectives of the test was to verify the performance of the test system and thus, specific requirements on the test article response and test data were defined. In particular, the test article was designed to exhibit global buckling at a load level between 50% and 70% of the maximum loading capacity of the apparatus. In addition, it was required that the test article exhibit an unstable collapse response characterized by a sudden reduction in axial load and release of energy, which is common in the buckling and collapse of thin-walled cylinders, so the safe control of testing into the postbuckling range of loading could be demonstrated.

The test article was designed using a two-step process (Ref. 3). First, the acreage stiffener pattern was designed using closed-form solutions, assuming a uniform construction throughout the cylinder, i.e., the effects of the axial weld lands were excluded. Several design constraints were applied during the design process to ensure that the test article would fail due to global buckling only and would exhibit significant margins on all other critical failure modes, such as skin pocket buckling (buckling of the skin between stiffener elements), stiffener buckling, and material yielding, to minimize the potential for failure mode interaction. The design variables included the skin thickness t, stiffener height h, axial and circumferential stiffener thickness t_s and t_r, and axial and circumferential stiffener spacing b_s and b_r (see Fig. 2.2 for orthogrid schematic). The

resulting acreage design includes a skin thickness of 0.100 inches, axial and circumferential stiffener spacing of 4.0 inches, axial and circumferential stiffener thickness of 0.100 inches, and a stiffener height, H, of 0.400 inches as measured from the OML. The design corresponds to an $R/t_{eff} = 230.9$, where t_{eff} is an effective shell wall thicknesses value defined in Fig. 2.2. A_{11} and A_{22} are axial and circumferential membrane stiffnesses and D_{11} and D_{22} are axial and circumferential bending stiffnesses as defined in Ref. 4.

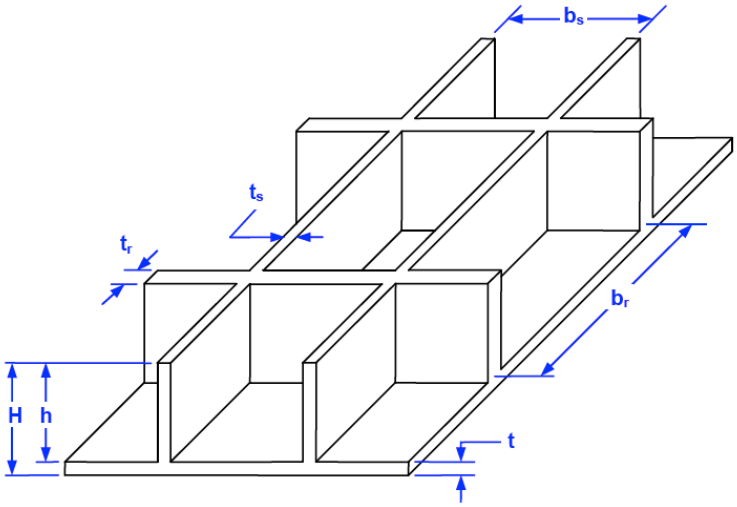

$t = 0.100$-inch $H = 0.4000$-inch $b_r = 4.000$-inch $t_r = 0.100$-inch

$b_s = 4.000$-inch $t_s = 0.100$-inch $h = 0.300$-inch

L/D: Barrel length to diameter ratio = 0.816

R/t_{eff}: Radius to effective wall thickness ratio = 230.9

$$t_{eff} = \sqrt[4]{\frac{144 D_{11} D_{22}}{A_{11} A_{22}}}$$

Figure 2.2. Orthogrid geometry definition.

Next, the three axial weld lands were introduced into the test article design and the shell response was analyzed using a geometrically nonlinear finite-element analysis. One of the design objectives was to include scaled versions of the weld land design used on the 27.5-foot-diameter space shuttle external tank (ET) (see Fig. 2.3-a). Scaling of the ET weld land geometry corresponded to a test article weld land thickness and half-width equal to 0.093 inches and 1.164 inches, respectively. However, the weld thickness was limited to a minimum of 0.25 inches, and weld land width was limited to a minimum of 2.5 inches due to restrictions on the welding process and fixtures that existed at the time of manufacturing.

Results from a detailed finite-element analysis of the preliminary test article design with three axial weld lands indicated that the test article was susceptible to local buckling along the weld lands due to the reduced bending stiffness in these locations (Ref. 3). Thus, additional reinforcement was added to the test article adjacent to the weld lands in order to minimize local buckling along the weld lands. Specifically, an additional axial stiffener was added on both sides of the weld land and the thickness of several of the stiffeners was increased as shown in Fig. 2.3-b and in Fig. 2.4. Finite element analysis results of this reinforced design indicated that these additional stiffeners eliminated the initiation of buckling in the weld land region and that the test article would exhibit similar behavioral characteristics as a uniform cylinder (Ref. 3). The final design drawing LaRC Drawing 1167189 is shown in Fig. 2.5 (Ref. 5).

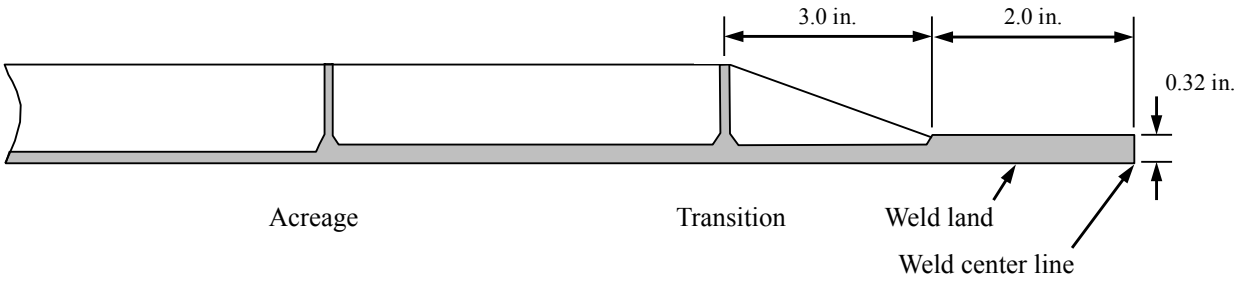

a) Typical space shuttle ET weld land design cross-section (not to scale).

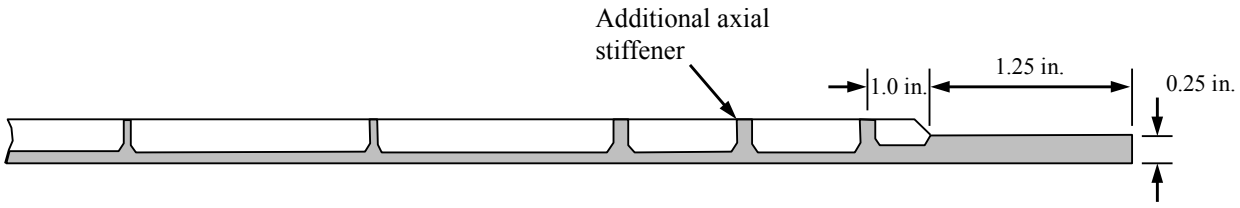

b) TA01 weld land design cross-section (not to scale).

Figure 2.3. Space shuttle ET and TA01 weld land designs shown in the flat condition for machining.

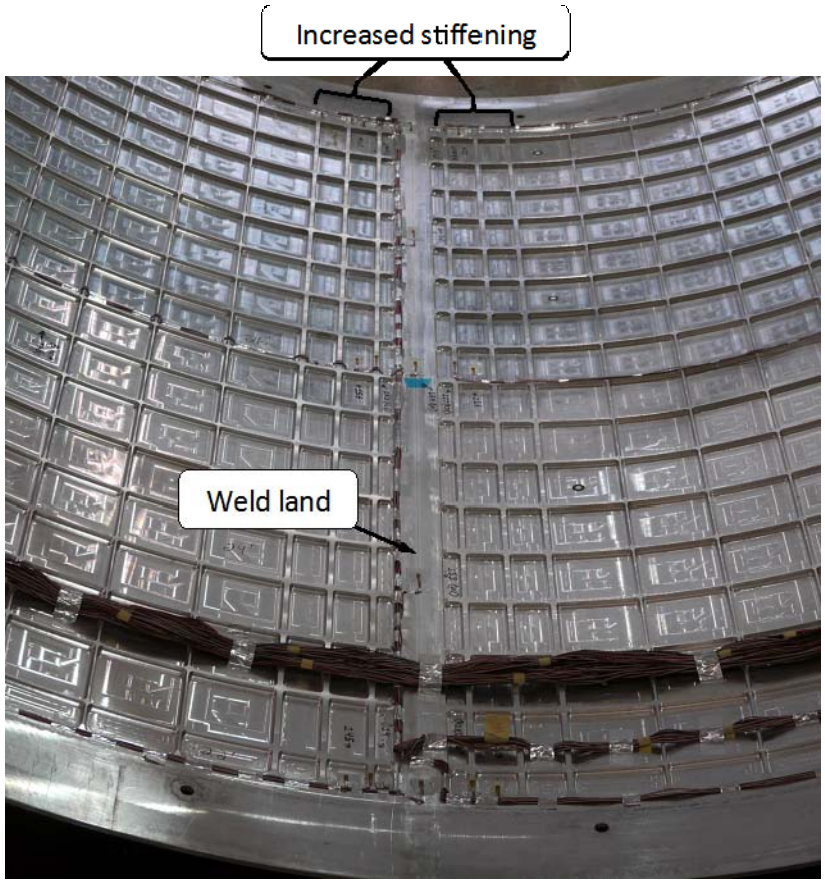

Figure 2.4. Typical weld land region in TA01.

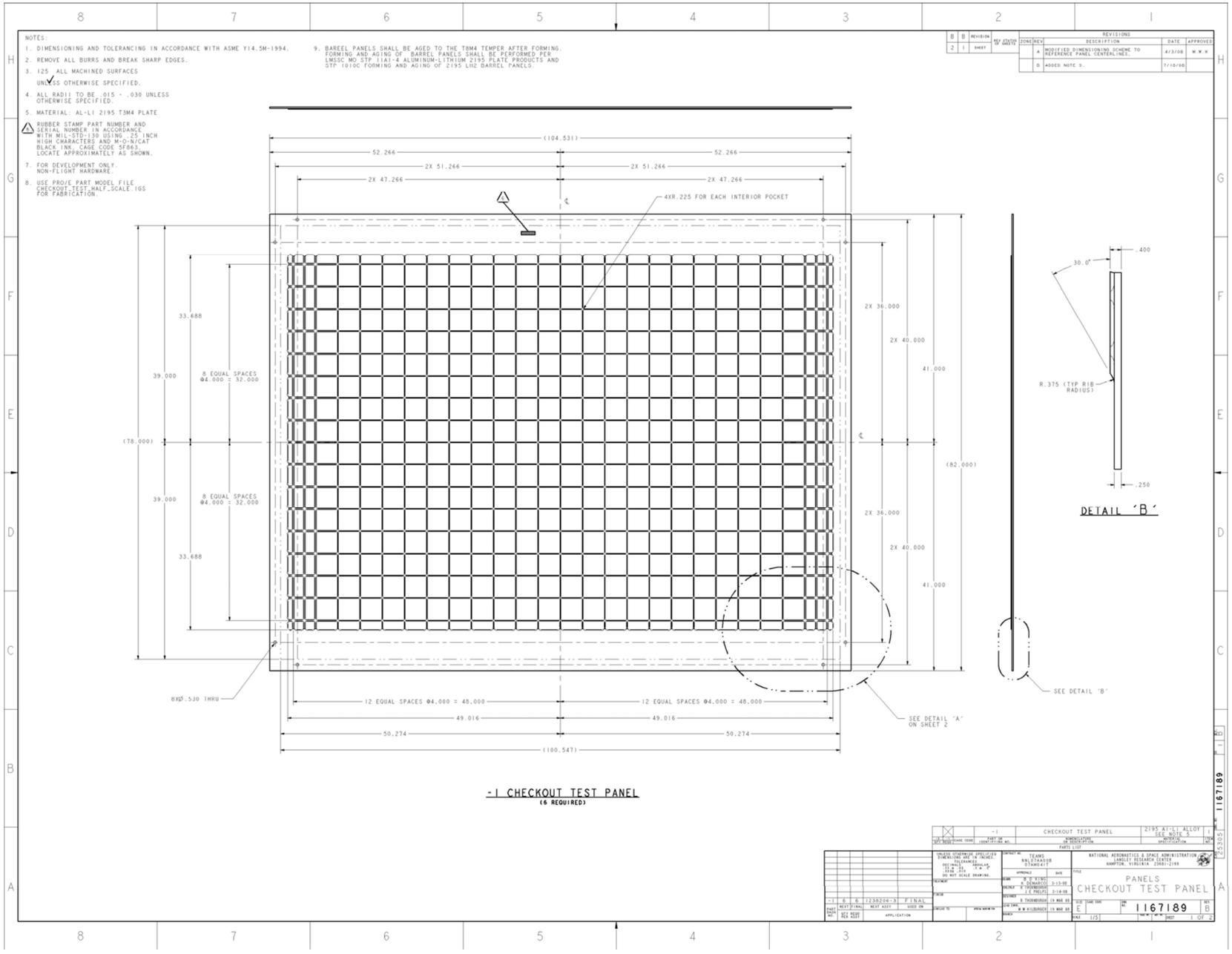

a) Inner mold line (IML) orthogrid stiffener pattern for a TA01 panel segment.

Figure 2.5. LaRC Drawing 1167189.

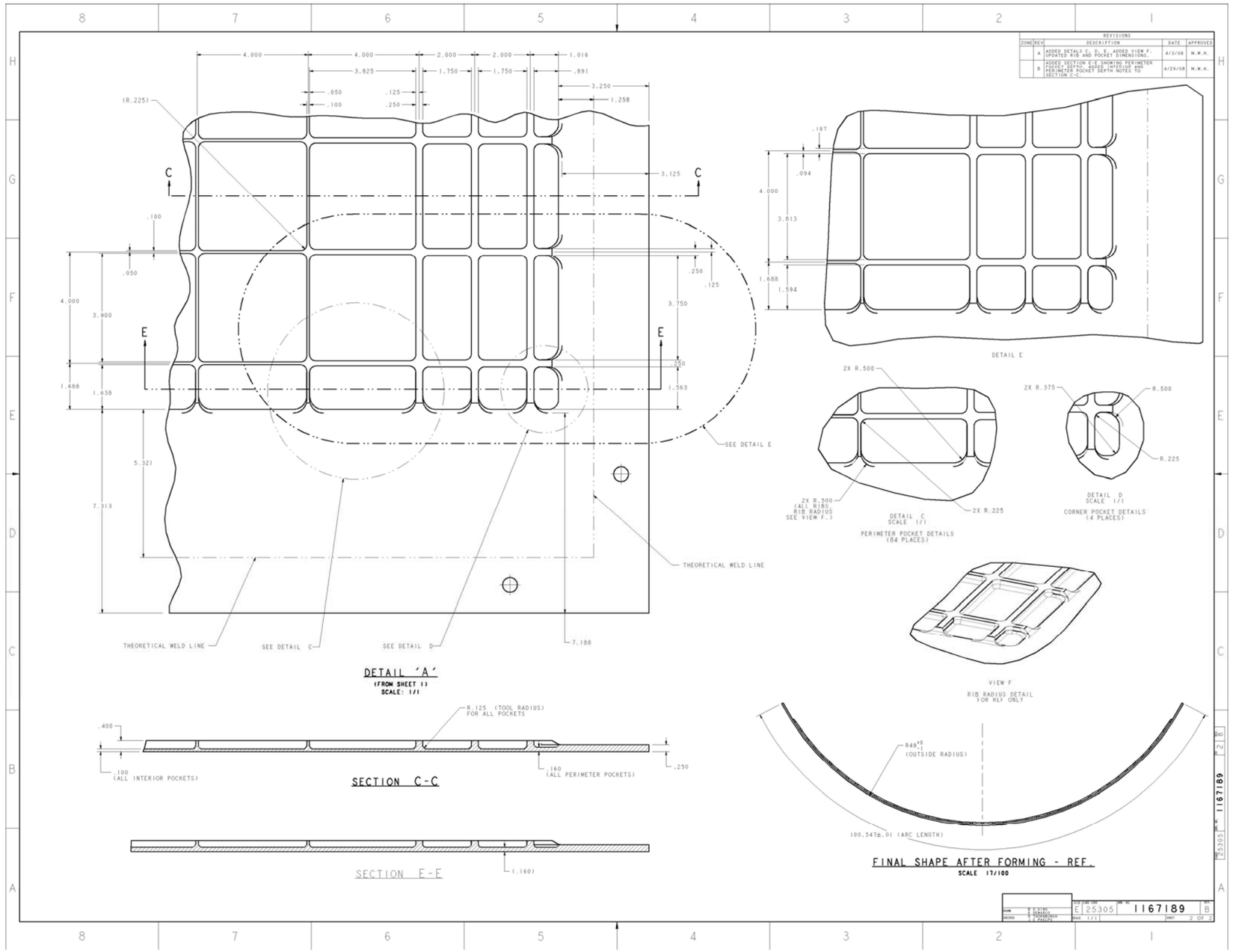

b) TA01 panel segment details.
Figure 2.5. Concluded.

2.3 Test Article Fabrication

Three curved panel segments were used to construct the barrel and were fabricated in a three-step process. First, the rectangular (orthogrid) stiffener pattern was machined into 2195-T3 Al-Li flat-plate material to form the pockets and weld land details. Then, the flat orthogrid panels were bump-formed (while in the –T3 temper) into curved panel segments with an OML radius of 48 inches using a brake press. Finally, the panels were heat treated and aged to a –T83 temper. Once machined, formed, and heat treated, the three orthogrid panels, referred to as Panels A, B, and C, were friction-stir welded together along the axial weld lands to form a cylinder with an 96.0-inch (8-foot) OML diameter and 78.0-inch length (dimensions are nominal). The three weld lands joining the three panels were 0.250 inches thick, and 1.25 inches wide on either side of the weld seam, resulting in a total weld-land width of 2.5 inches. Each weld was subjected to a series of visual and ultrasonic quality inspections (see Ref. 6). No defects or anomalies were identified in TA01.

The ends of the test article were machined flat and parallel to tolerances specified in the manufacturing and assembly drawing 1238206 (Ref. 7) in order to ensure uniform load introduction into the test article. Geometry inspection after machining indicated the top and bottom ends of the test article were flat to within 0.039 inches and 0.040 inches, respectively, and parallel to each other to within 0.064 inches.

Once machining and inspection were complete, the test article was potted in attachment rings with a low-melting-temperature alloy (Ref. 8). Concentricity and bolt-hole alignment specifications between the top and bottom attachment rings were defined so as to minimize any loads that would result from the misalignment of the test assembly. Shims were used to position the test article in the attachment rings and adjust concentricity. Ring alignment and concentricity were verified using a plumb bob.

Once potted, the geometry of the test article OML was measured using a GOM ATOS photogrammetry/white-light geometry measurement system[ii] with a measurement accuracy of ±0.001 inch. The deviation of the measured geometry from a best-fit cylinder was calculated and defined as the initial geometric imperfection (*imp*) and is shown in Fig. 2.6. The coordinate system used in the geometry measurement is shown in Fig. 2.7. The three longitudinal weld lands are located at –60°, 60° and 180° and the 0° circumferential location is aligned with the center of Panel A. The OML geometry data indicate that the test article is circular to within ±0.10 inches. The weld lands do not appear to have a strong influence on or correlation with the imperfection pattern. The top and bottom attachment ring loading surfaces of the test article assembly were measured using a Leica AT901 laser tracker system[iii] to verify the tolerances on flatness and parallelism. The top and bottom attachment ring loading surfaces were flat to within 0.014 inches and 0.009 inches, respectively, and were parallel to each other to within 0.004 inches. The orthogrid design, barrel assembly, and attachment ring design are presented in Drawings 1167189 (Ref. 5), 1238206 (Ref. 7) and 1238205 (Ref. 8), respectively, and in Section 2.1 of the test plan (Ref. 1).

[ii] http://www.gom.com/metrology-systems/3d-scanner.html

[iii] http://www.leica-geosystems.us/en/Leica-Absolute-Tracker-AT901_69047.htm

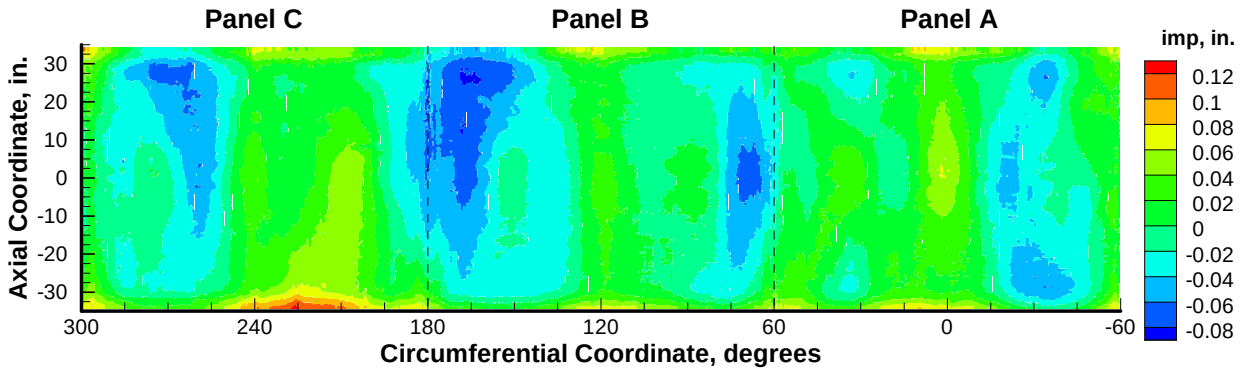

Figure 2.6. Measured geometric imperfection for TA01 from photogrammetry/white-light geometry scanning system.

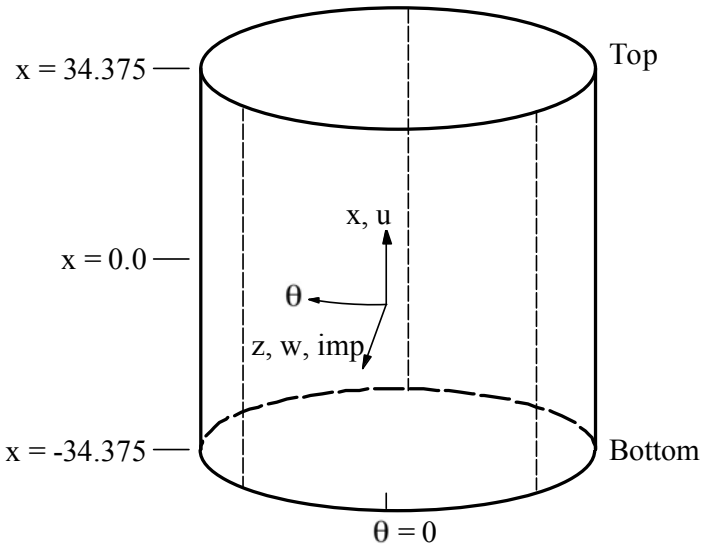

Figure 2.7. Coordinate system and displacement definitions. 0° circumferential location corresponds to the center of Panel A and the dashed lines indicate the location of longitudinal weld lands.

2.4 Test Facility

The test facility is comprised of the test assembly (test article, test fixtures), load control system, and data acquisition system (DAS). The test assembly is shown in Fig. 2.8 and engineering drawings are found in Drawing 90M12370 (Ref. 9). The test assembly is a self-reacting load system composed of an upper and lower load "spider", 16 load struts, upper and lower load-introduction cylinders (referred to in Ref. 9 and Fig. 2.8 as transition sections), the test article assembly, and eight load lines. Each load line consists of a hydraulic cylinder, a 4-inch-diameter loading rod, a load cell, and attachment hardware. Each load line attaches to the upper and lower loading spiders. The load lines can be controlled independently in load control or stroke (position) control to apply uniform compression or combined compression and bending with a maximum load capability of 1.5 million pounds of axial compression force and 80,000 pounds of axial tension force. The test fixtures were designed and analyzed to ensure uniform load introduction into the test article when subjected to uniform compression up to the maximum load

capability of the apparatus. It should be noted that the load lines are in tension when the test article is subjected to compression loads. Additional information on the loading structure is also documented in Drawing 90M12375 (Ref. 10). A top-view schematic of the test assembly is presented in Fig. 2.9 and indicates the test article orientation and load line locations (indicated by the filled circle symbols in the figure) with respect to the panel and weld locations. In addition, the three panel sections that comprise the barrel test article are labeled as Panels A, B, and C.

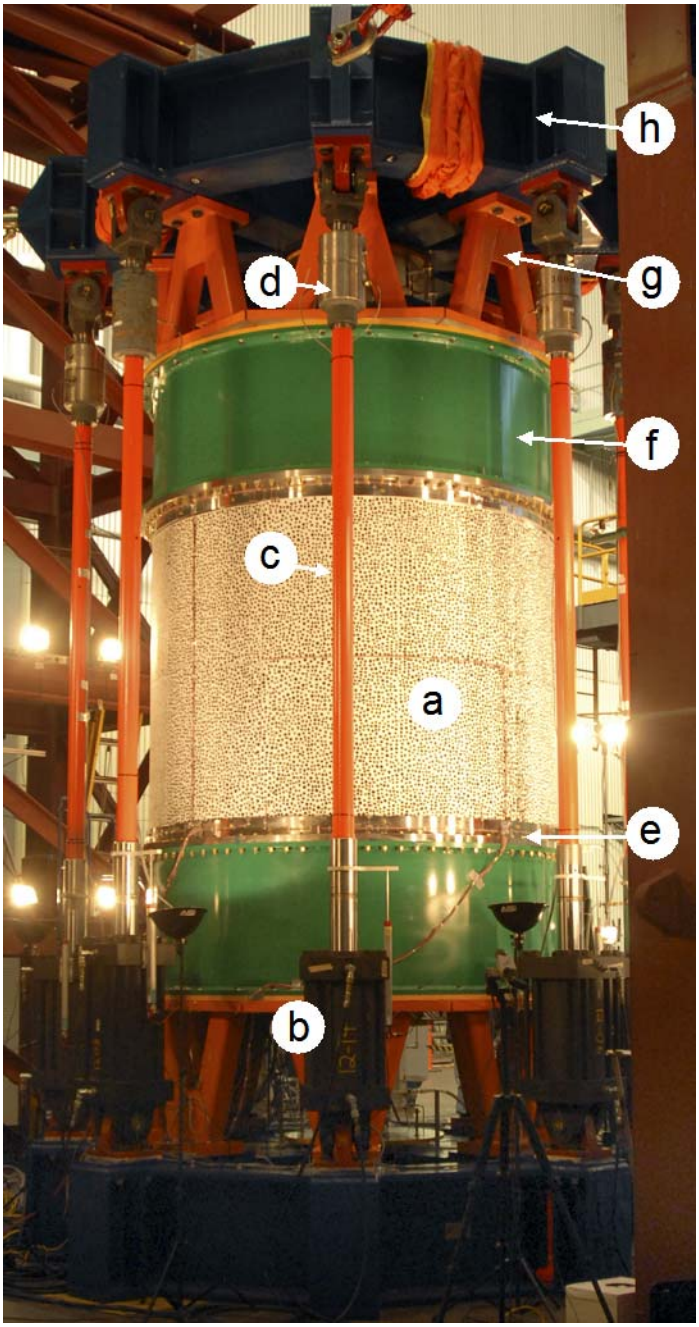

Figure 2.8. Eight-foot-diameter shell buckling test facility at MSFC: a) test article assembly, b) hydraulic actuator, c) loading rod, d) load cell, e) attachment ring, f) transition section, g) load strut, and h) loading spider.

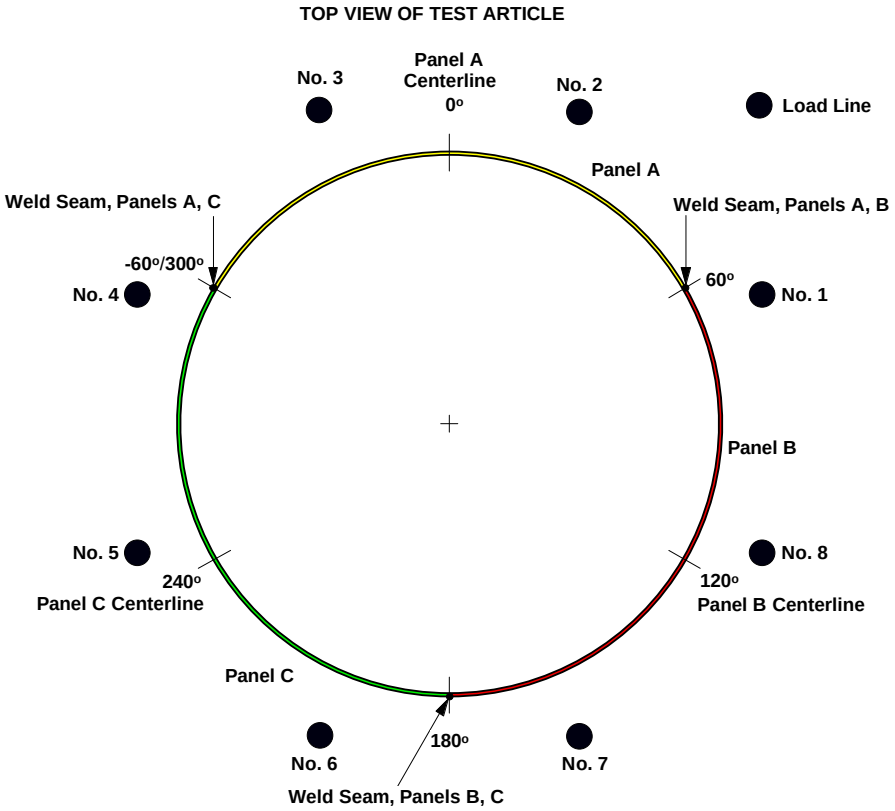

Figure 2.9. Test article orientation and panel, weld land, and load line locations.

The DAS was a custom-built Structural Loads Test Measurement Acquisition System (SLTMAS) developed by MSFC/ET30 that can record up to 4792 analog inputs and 192 digital inputs. The DAS uses National Instruments SCXI-1520 signal conditioners for the strain gages, load cells, and linear voltage displacement transducers (LVDTs).

The load control system (LCS) was an MTS FlexTest® 60 multi-channel system. It was programmed to use a combination of load control and displacement control during the testing. More specifically, during sub-critical load sequences, the LCS applied loads to TA01 in load control to ensure uniform loading. However, during the final load sequence to failure, the LCS was programmed to apply loads in load control up to 60% of the expected buckling load. Then, the LCS was transitioned to displacement (stroke) control so that the test could proceed safely through any unstable buckling events and into the postbuckling range of loading. In all load cases, the LCS was programmed such that the load rate never exceeded 10,000 lbf per minute. Specific load control requirements are defined in the test plan and test procedure.

2.5 Testing

2.5.1 Test Article Installation and Alignment Verification

Once the test article was installed into the test fixture and the load lines were mounted between the upper and lower loading spiders, relative alignment between the test article and the load lines was measured using an inclinometer. However, the inclinometer measurements were relatively low precision (±0.1°) and the data appeared to be inconsistent with observed alignments via plumb bob. Subsequent tests on similar 8-foot-diameter cylinders included higher precision measurements using a laser-tracker-based position measurement system with ±0.001° accuracy.

These measurements indicated that the load lines were typically parallel to the axis of the test article to within 0.050° corresponding to a maximum misalignment of 0.18 inches from top to bottom.

2.5.2 Instrumentation

TA01 was instrumented with 270 strain gages and a typical pattern is shown for Panel A in Fig. 2.10 (Ref. 11). Strain gage locations and naming convention are summarized in Table A1 in Appendix A. Twenty-four Electronic Displacement Indicators (EDIs), also referred to as LVDTs, were placed at various locations on the specimen to measure axial, radial, and tangential displacements. Schematic views of the EDI measurement locations and orientations are shown in Figs. 2.11 and 2.12. In particular, axial displacements measurement locations are indicated by open circle symbols and radial and tangential measurements are indicated by arrows in Figure 2.12. EDI locations and naming convention are summarized in Table A2 in Appendix A.

The axial end-shortening of TA01 was measured at four locations around the circumference of the test article and correspond to the relative displacement measurements between the upper and lower test article attachment rings at the 0°, 90°, 180°, and 270° locations around the circumference of the test article. End-shortening displacements at the four circumferential locations are defined as follows:

$$0°: \quad \delta_{D263AA} = \delta_{D239AA} - \delta_{D259AA}$$

$$90°: \quad \delta_{D264AA} = \delta_{D240AA} - \delta_{D260AA}$$

$$180°: \quad \delta_{D265AA} = \delta_{D241AA} - \delta_{D261AA}$$

$$270°: \quad \delta_{D266AA} = \delta_{D242AA} - \delta_{D262AA}$$

where δ_{D239AA}, δ_{D240AA}, δ_{D241AA}, δ_{D242AA} and δ_{D259AA}, δ_{D260AA}, δ_{D261AA}, δ_{D262AA} correspond to EDI measurements on the top and bottom attachment rings, respectively, and δ_{D263AA}, δ_{D264AA}, δ_{D265AA}, δ_{D266AA} correspond to the derived end-shortening displacements. Similarly, transverse shear displacement and twisting of the cylinder were determined from the relative radial and tangential displacements measured at the top and bottom attachment rings.

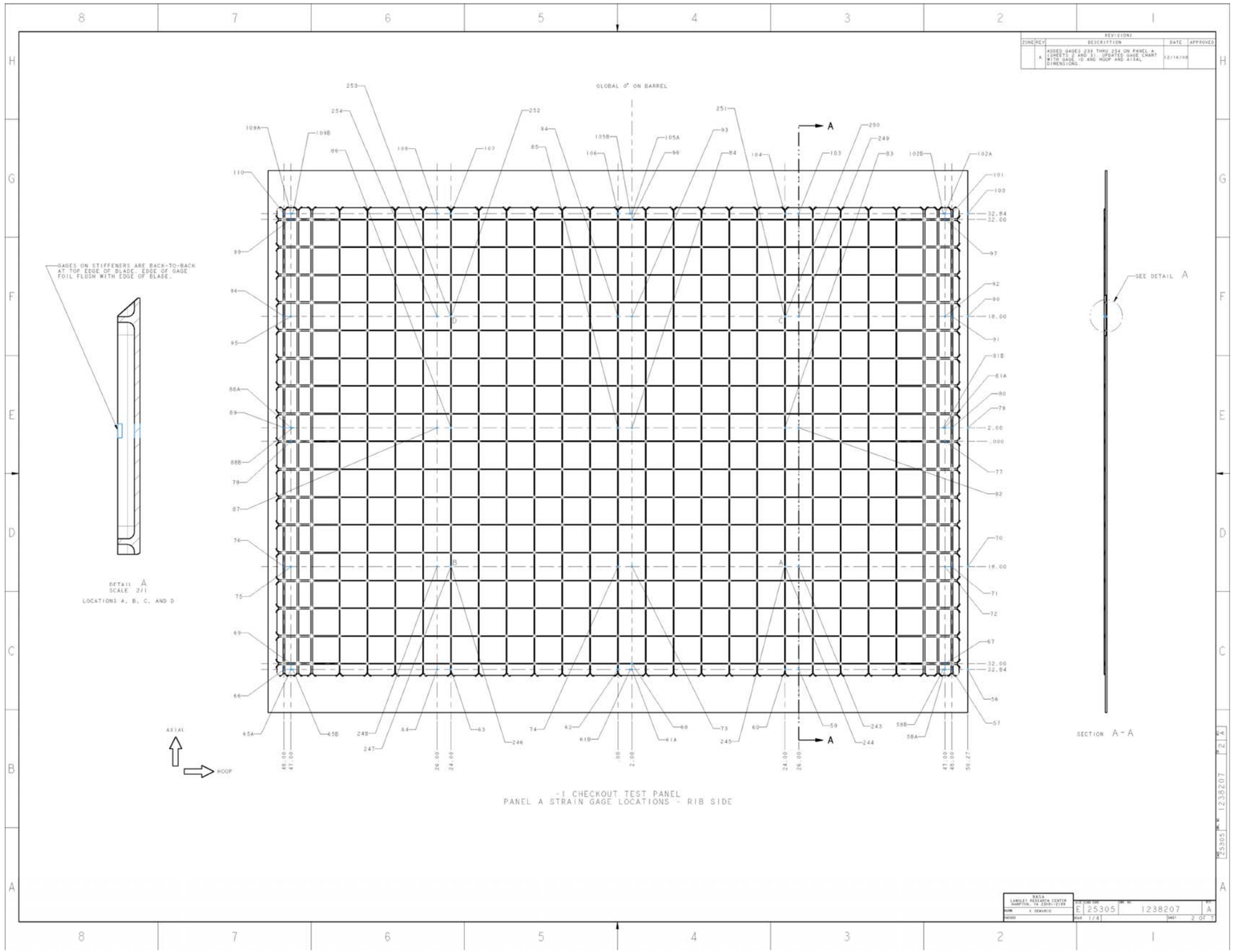

Figure 2.10. Typical IML strain gage pattern for one of the TA01 panel segments.

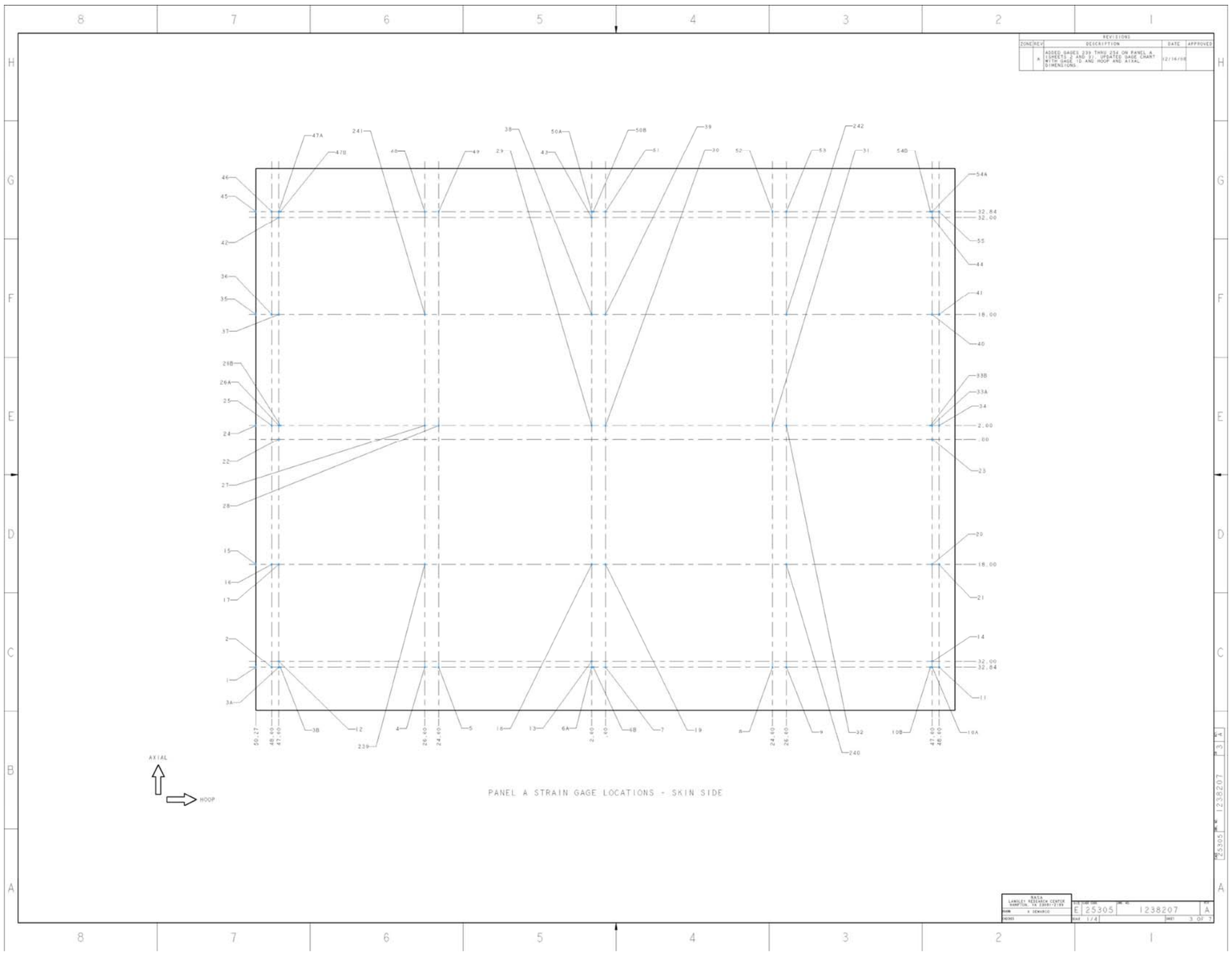

Figure 2.10. Concluded.

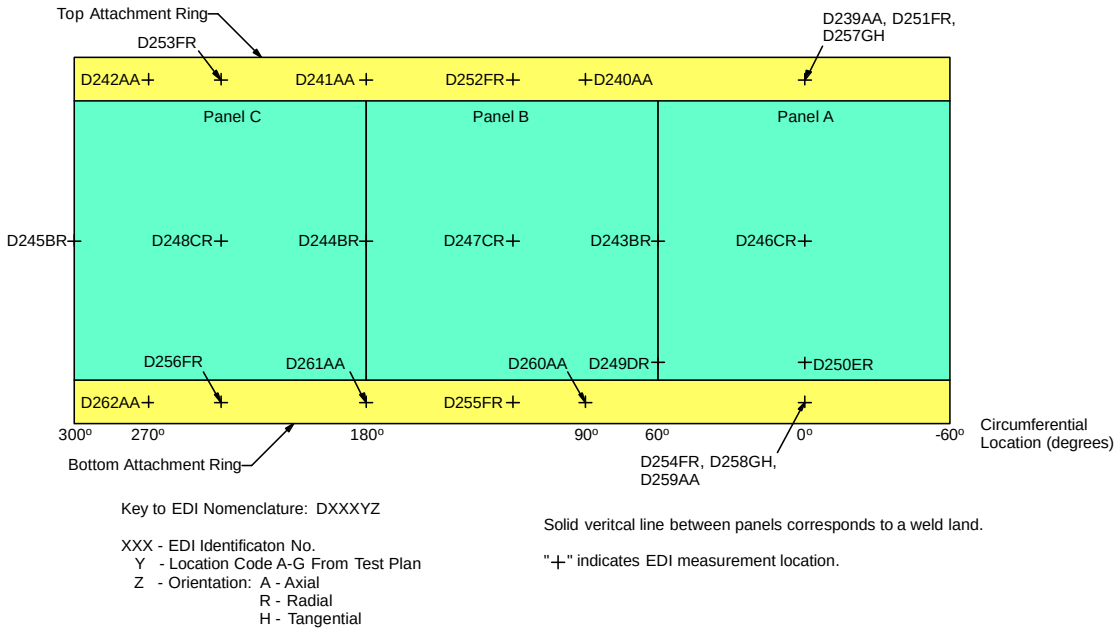

Y – EDI Location Code

A	axial displacement measurements at four places on the top and bottom attachment rings
B	radial displacment measurements at the mid-length of each weld land
C	radial displacment measurements at the center of each panel
D	radial displacement measurement of weld land AB (weld land between panel A and panel B) 5 inches up from the bottom attachement ring
E	radial displacement measurement at mid-arc-width of panel A (0 degree circumferential location) and 5 inches up from the bottom attachment ring
F	radial displacement measurements at three points on both the bottom and top attachment rings, located at the mid-arc-width of each panel
G	tangential displacement measurements on both the bottom and top attachement rings, located at the 0 degree circumferential location

Figure 2.11. Schematic view showing locations of EDIs (view from outer surface) and EDI location table.

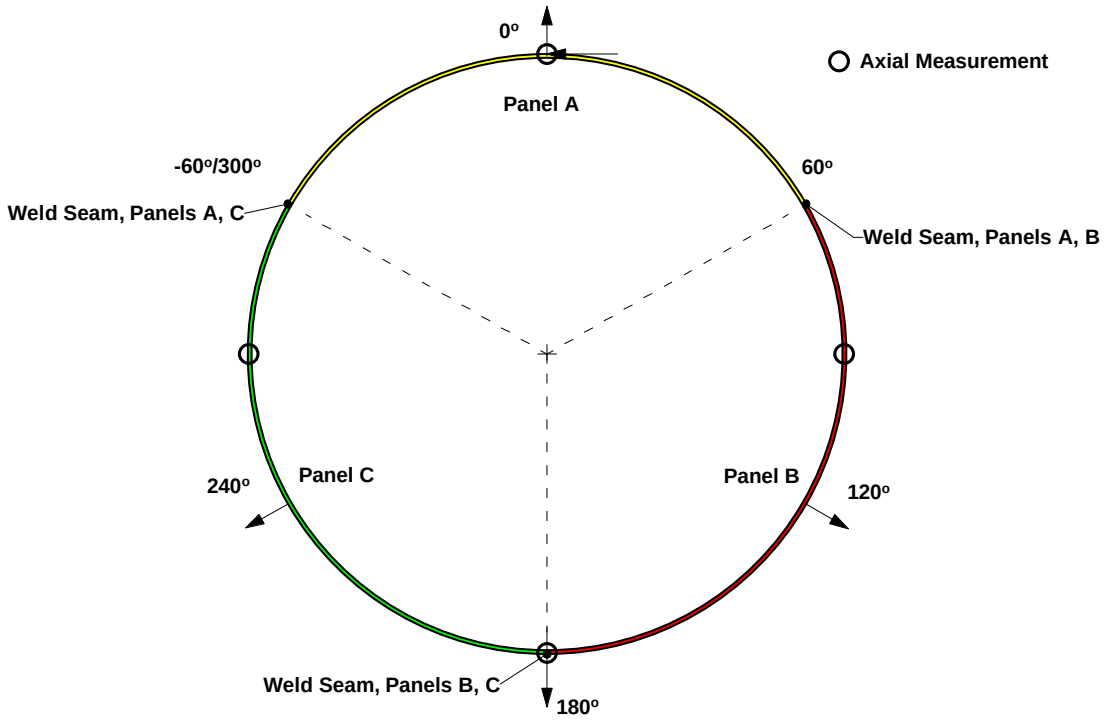

a) Axial, radial and tangential displacement measurement locations on the top and bottom attachment rings.

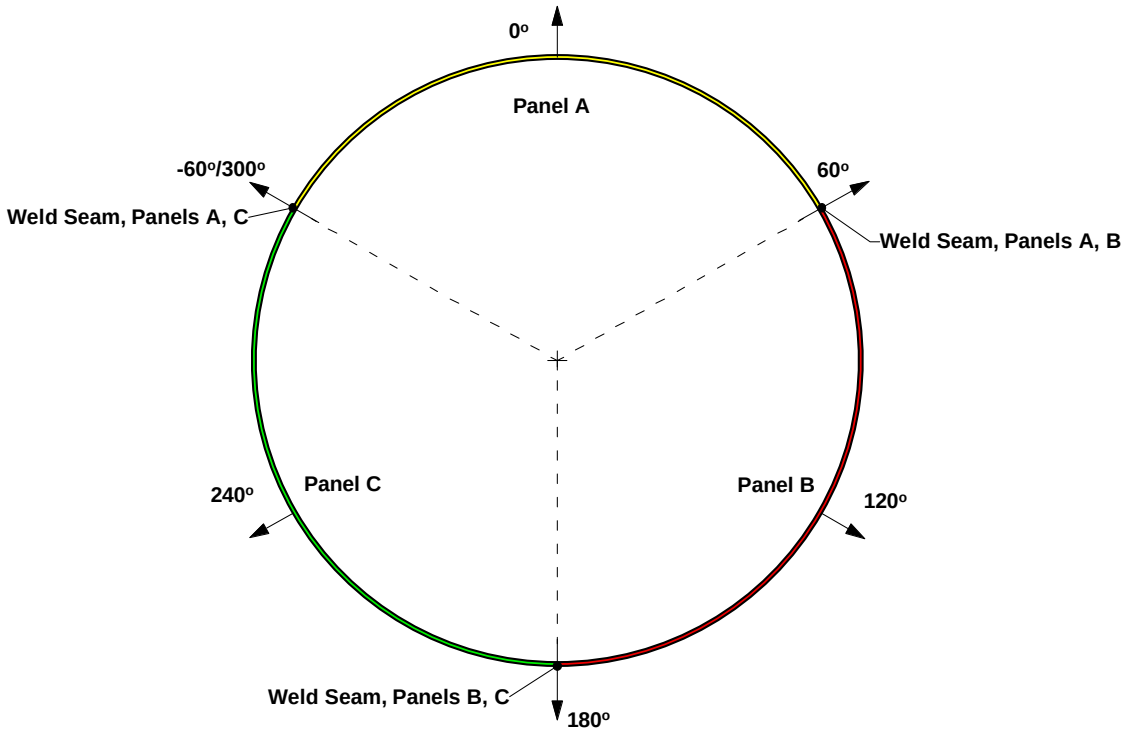

b) Radial displacement measurement locations at the test article mid-length.

Figure 2.12. Schematic view showing locations and orientations of EDIs, top view.

2.5.3 Low-Speed Digital Image Correlation

DIC was used to obtain full-field three-dimensional (3D) displacement data on approximately 85% of the test article OML surface. Schematics of the DIC coordinate system and fields of view (FOV) are presented in Figs. 2.7 and 2.13, respectively. Complete coverage of the TA01 OML could not be achieved due to four of the eight load lines obstructing the views of the DIC system cameras, specifically, load lines 2, 4, 6, and 8 as illustrated in Fig 2.13. Note: the camera locations and FOV indicated in Fig. 2.13 are notional and are not to scale.

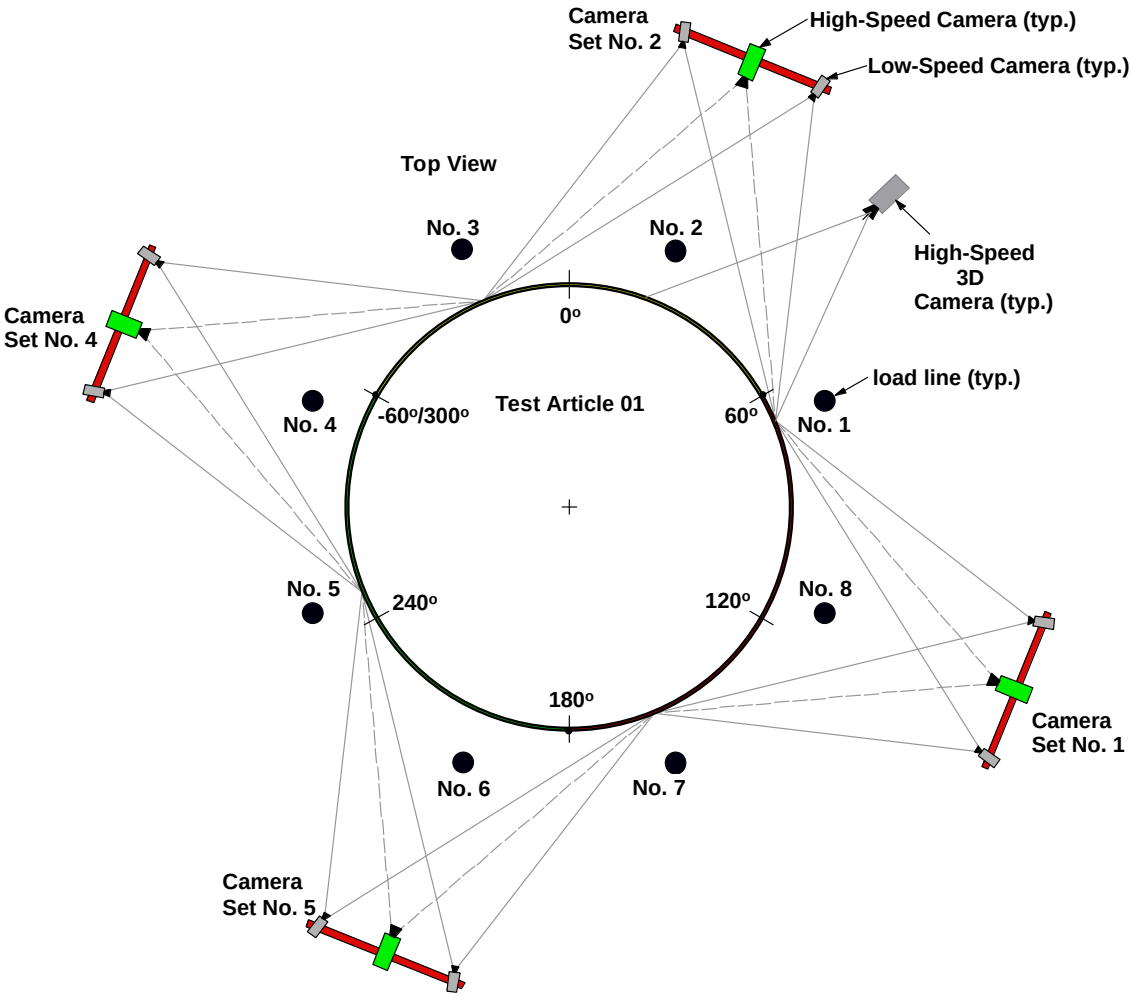

Figure 2.13. Location of load lines 1–8 and low-speed and high-speed DIC systems.

The DIC system was also used to measure a pretest OML surface geometry for correlation with previous white-light geometry measurements (described in Section 2.3) in order to verify that no significant changes in geometry had occurred between manufacturing and test integration. DIC data (images) were acquired every 5 seconds throughout each load sequence using the 2007 Correlated Solutions Vic-Snap software[iv].

[iv] www.correlatedsolutions.com

The DIC requirements and setup information are presented in more detail in Section 3.0 of Ref. 1.

Displacement data were post-processed by using the 2007 Correlated Solutions VIC-3D™ software[v] and converted into cylindrical coordinates (coordinate system defined in Fig. 2.7). In addition, the VIC-3D™ session files, all calibration information, and all acquired images have been archived to enable further detailed processing at a later date. See Appendix A for archival information.

2.5.4 High-speed Digital Image Correlation

Four single-camera, two-dimensional (2D) high-speed DIC systems were co-located with the four low-speed 3D DIC systems around the circumference of the test article as shown in Fig. 2.13. Notional FOV of the high-speed DIC systems are shown in Fig 2.13. The high-speed DIC systems used Vision Research Phantom 7.1 digital cameras with a resolution of 400 × 400 pixels and recorded images at 10000 fps. The cameras were synchronized using an inter-range instrumentation group (IRIG) option and used a manual post-trigger to capture images of the buckling event. The FOV of each high-speed camera is indicated in Fig. 2.14 with a shaded rectangle superposed on the low-speed DIC FOV images for reference. Unfortunately, the high-speed camera FOVs were not properly verified before testing and only limited regions of the test article OML were imaged. However, the high-speed images would still be useful in observing the initiation and propagation of buckling in the TA.

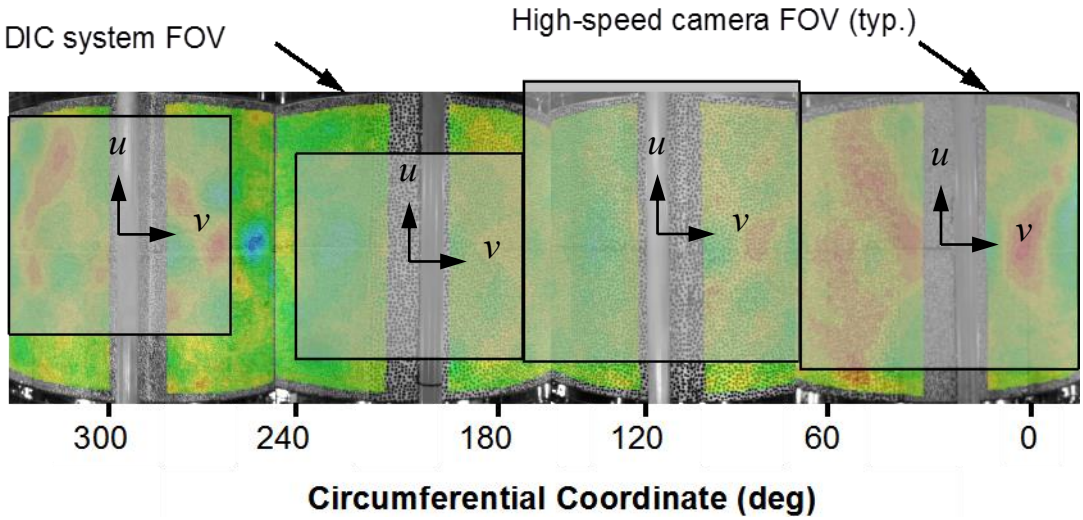

Figure 2.14. High-speed camera FOVs.

The images captured from each of the high-speed cameras were post-processed by using the 2007 Correlated Solutions VIC-2D™ software to calculate *u* and *v* displacements in the plane of each FOV. The *u* and *v* displacements are used to qualitatively observe the radial deformations w of the test article OML, as illustrated in Fig. 2.15, by calculating $\sqrt{u^2 + v^2}$.

[v] www.correlatedsolutions.com

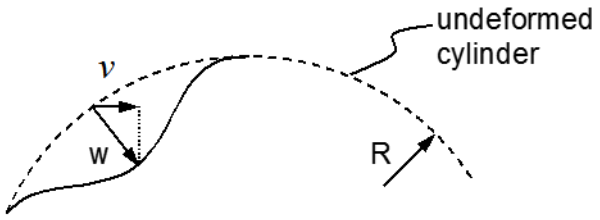

Figure 2.15. Using 2D DIC technique to qualitatively assess the radial deformations of TA01.

In addition, data from one high-speed 3D DIC system were also obtained and are presented herein. The 3D DIC system was positioned between load lines 1 and 2 with a FOV from approximately 15° to 70°, as shown in Fig. 2.13.

2.5.5 Load Sequences

TA01 was subjected to five loading sequences: four subcritical load sequences (i.e., load levels that do not induce test article buckling/failure) and one final loading sequence to buckling and collapse. These load cases include three uniform axial compression load cases and two combined axial compression and bending load cases as follows:

Load Sequence 1: Uniform axial compression to 0.2 P_{cr}
Load Sequence 2: Combined axial compression and bending to 0.1 P_{cr} + 0.1 M_{cr}
Load Sequence 3: Uniform axial compression to 0.4 P_{cr}
Load Sequence 4: Combined axial compression and bending to 0.2 P_{cr} + 0.2 M_{cr}
Load Sequence 5: Uniform axial compression to failure.

P_{cr} and M_{cr} correspond to the predicted linear bifurcation buckling loads for a geometrically perfect, uniform cylinder (i.e., uniform geometry and does not include the weld lands) subjected to uniform compression and uniform bending. P_{cr} = 726,800 lb and M_{cr} = 36.35e6 inch-lb. The load sequences are defined in more detail in the TA01 test plan (Ref. 1) and test procedure (Ref. 2).[vi]

3.0 Analysis Description

Pretest predictions of the buckling response of TA01 were used to determine testing and instrumentation requirements and are presented in this test report for reference. These pretest predictions include many simplifying assumptions and should be viewed as preliminary in nature. Final post-test predictions will be presented in a separate series of NASA technical publications in which refined modeling and analysis approaches and results will be discussed in detail.

Pretest predictions of the buckling response of TA01 were obtained using the STAGS (STructural Analysis of General Shells) nonlinear shell-analysis code (Ref 12). STAGS is a finite-element code developed for the static and dynamic analysis of general shells, and

[vi] TA01 was subjected to combined axial compression and bending during some of the sub-critical load sequences. However, the test to failure, in which the test article was subjected to axial compression only, was the primary load sequence used to verify the performance of the test system. TA02 would be tested at a later date and would be subjected to combined axial compression and bending until buckling and collapse in order to verify the performance of the system under combined loading conditions.

includes the effects of geometric nonlinearities in the analysis. The finite-element model included representations of the entire test assembly including the steel load introduction structure, load lines, test article attachment rings, and the test article (see Fig. 3.1). A combination of beam and shell elements was used to generate the model. The standard 410 quadrilateral shell element from the STAGS element library was used in the model and is a four-noded flat facet-type element that is based on the Kirchoff-Love shell hypothesis and the nonlinear Lagrangian strain tensor. The element nodes include three translational degrees of freedom and three rotational degrees of freedom. Large element rotations are accounted for by using a corotational algorithm. The STAGS 210 beam element was also used and is based on the Timoshenko beam theory.

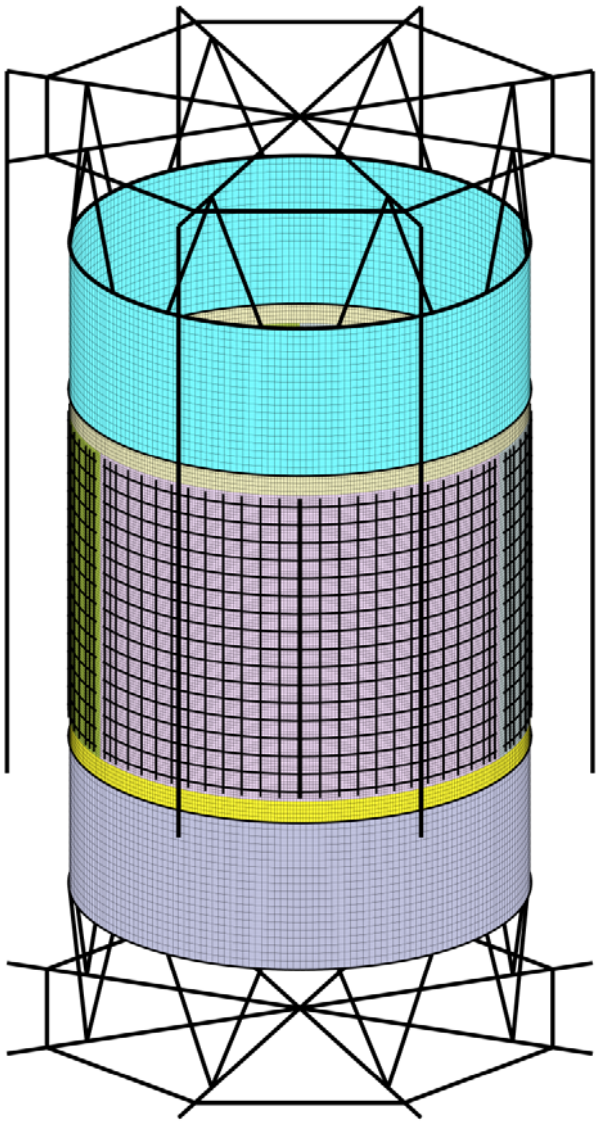

Figure 3.1. Finite-element model of test assembly.

The model was constructed such that the load-introduction fixtures, attachment rings, and TA were separate entities and joined at each interface with multi-point constraints. The load introduction structure was included in the analysis to ensure that the boundary stiffness and kinematics were modeled accurately. The TA01 model included the three

longitudinal weld land details, and beam elements were used to represent the stiffeners. The nominal as-designed TA dimensions were used to define the model. The as-measured initial TA geometry (Fig. 2.6) was then used to modify the geometrically perfect nominal geometry of the test article mesh to accurately represent the as-built geometrically imperfect TA. Specifically, a user-written subroutine was used to read in the measured geometry of the TA OML and adjust or perturb the OML geometry of the finite-element mesh at each nodal location.

The load was introduced into the structure by applying eight point loads at the ends of beams representing the load lines in the test configuration and the bottom-loading spider was held fixed at its base. The connections between each of the components of the test assembly were assumed to be perfect, that is, the bolted connections were assumed to be uniform rigid attachments with no relative movement between each component. It should be noted that the pretest analyses reported in Ref. 13 assumed all eight point loads were equal, achieving uniform compression. However, since that time, the analyses have been updated to include the actual measured load line load values, which produced a small amount of nonuniformity of loading. The results from these updated analyses are presented along with the test data but do not show any significant variation from the original pretest analysis results.

Al-Li 2195-T8M4 plate material properties from MSFC-HDBK-3513 (Ref. 14) were used in the analysis and included an elastic modulus of 11.0e6 psi, a Poisson ratio of 0.33, density of 0.098 lbm/in^3, and a yield stress of 66.0e3 psi. Material data obtained from Ref. 14 indicate that the material exhibits slight differences in the longitudinal and transverse stiffness properties but this was not considered during the preliminary test article design and pretest analysis. Standard A36 steel properties were used for all the test fixture components. Detailed modeling information and results are presented in Refs. 3 and 13.

4.0 Results and Discussion

Results from the testing of TA01 are presented in this section. First, geometric imperfection data obtained from the DIC system are presented and compared to the photogrammetry/white-light geometry measurement in Section 4.1. Then, selected results from load sequence 5 (LS5) test to failure are presented and compared to pretest predictions in Section 4.2. The test results include, load versus end-shortening, and load versus radial displacement response curves. Then, low-speed and high-speed DIC displacement contours are presented for selected prebuckling, buckling and postbuckling load levels. Finally, load versus axial strain response curves are presented along with plots of the axial strain distribution around the circumference of the test article for selected prebuckling load levels and incipient buckling.

4.1 Initial Geometric Imperfection Data

The initial OML geometry of TA01 was measured prior to its installation into the test facility by using a photogrammetry/white-light metrology technique as described in Section 2.3. The measurement accuracy was ±0.001 inches. The deviation of the measured data from a best-fit cylinder was calculated and defined as the initial geometric imperfection (*imp*) and is shown in Fig. 2.6. The three longitudinal weld lands are located at –60°, 60°, and 180°. The measured data indicate that TA01 was, for the most part,

circular to within ±0.10 inches with some additional deviations near the lower boundary. The weld lands do not appear to have a strong influence on or correlation with the imperfection pattern.

DIC geometry measurements were taken after TA01 was installed in the test facility, immediately prior to testing and are shown in Fig. 4.1. The DIC measurements were obtained to determine if any additional geometric distortions developed in TA01 during handling and installation into the test fixtures as compared to the geometry measurements shown in Fig. 2.6. The accuracy of the measurement was approximately ±0.020 inches and thus only gross geometric distortions could be observed. For the most part, the DIC pretest geometry measurement shares similar characteristics as the high-resolution white-light/photogrammetry measurement including the circumferential periodic variation in the geometry and no significant differences were observed.

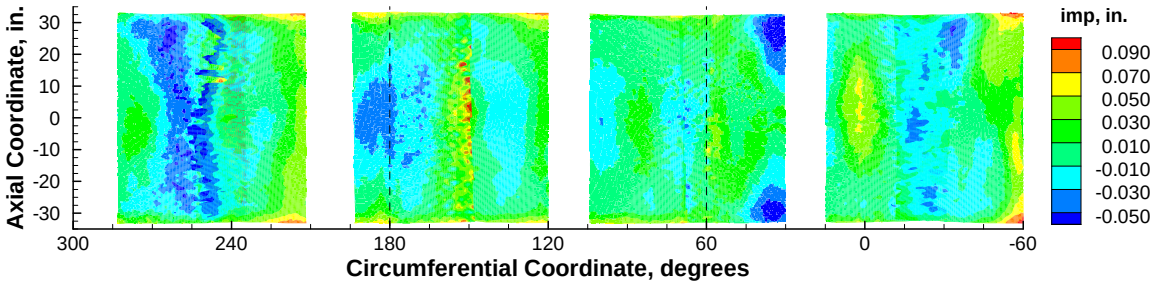

Figure 4.1. Geometric imperfection for TA01 from DIC measurement.

4.2 Buckling Response of TA01

Selected test results are presented to illustrate the overall buckling response of TA01 subjected to uniform axial compression. In addition, pretest analysis results are presented and compared to the test results.

4.2.1 Load versus Displacement Response

Predicted and measured load versus end-shortening response curves for TA01 are shown in Fig. 4.2 and are indicated by the solid and dashed curves, respectively. TA01 exhibits a linear prebuckling response up to a maximum load of 689 Kips (1 Kip = 1000 lb force) during the test. The maximum load is followed by the buckling and collapse of TA01 and is characterized by a sudden reduction in the axial load of approximately 61% to a postbuckling load of 270 Kips. In addition, the measured load versus end-shortening response curve indicates a significant increase in the end-shortening displacement during the buckling response from 0.12 to 0.20 inches. This increase in end-shortening is associated with the release of elastic strain energy in the test fixtures coupled with the reduced stiffness of the test article during the buckling response and in the postbuckling range of loading. Note that the oscillation of the predicted axial load in the initial postbuckling range is attributed to the structural damping parameters used in the finite element simulation.

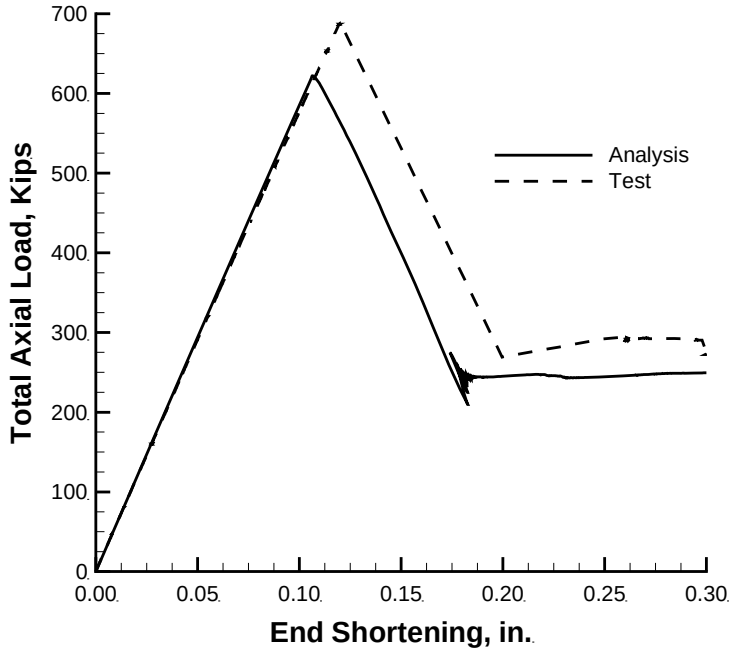

Figure 4.2. Measured and predicted load versus end-shortening response of TA01 subjected to axial compression.

Overall, the character of the load versus end-shortening response is predicted well, including the prebuckling and postbuckling axial stiffness; however, the predicted maximum load of 620 Kips is approximately 10% lower than the measured maximum load of 689 Kips.

Predicted and measured prebuckling load versus radial displacement response curves are presented in Figs. 4.3 and 4.4 and include displacements measured at the cylinder mid-length at the center of each panel segment and at the center of each weld land, respectively. Positive displacements correspond to outward radial displacements. The buckling and postbuckling data are omitted from these figures so that the small-magnitude prebuckling displacements could be seen more clearly. The results indicate that both the weld lands and the panel centers move radially outward during the prebuckling response. As the loading approaches the buckling point (maximum load), the measured radial displacements in panel C and at weld land BC increase at a higher rate than at the other measurement locations and are associated with the onset of buckling in panel C. The predicted results indicate similar response trends overall; however, the displacements exhibit rapid growth in panel A and correspond to the initiation of buckling in panel A. In addition, the predicted radial displacements are in all cases larger than the corresponding measured displacements.

It is noted that, the measured displacement response at weld land AB indicates a sudden increase in the radial displacements between a load level of 415 Kips and 435 Kips. After 435 Kips, the slope of the displacement response curve reverts back to its previous value. However, measured data from other nearby strain gages (e.g., see data in Section 4.2.3) and digital image correlation data do not indicate any type of local change in behavior. In addition, previous testing with these particular LVDT instruments indicated similar anomalies. After review of these measurement anomalies, it was determined that the LVDT interface connection with the test article could become partially detached. Thus,

based on these previous observations, it is very likely that this measurement anomaly is due to a faulty LVDT interface connection.

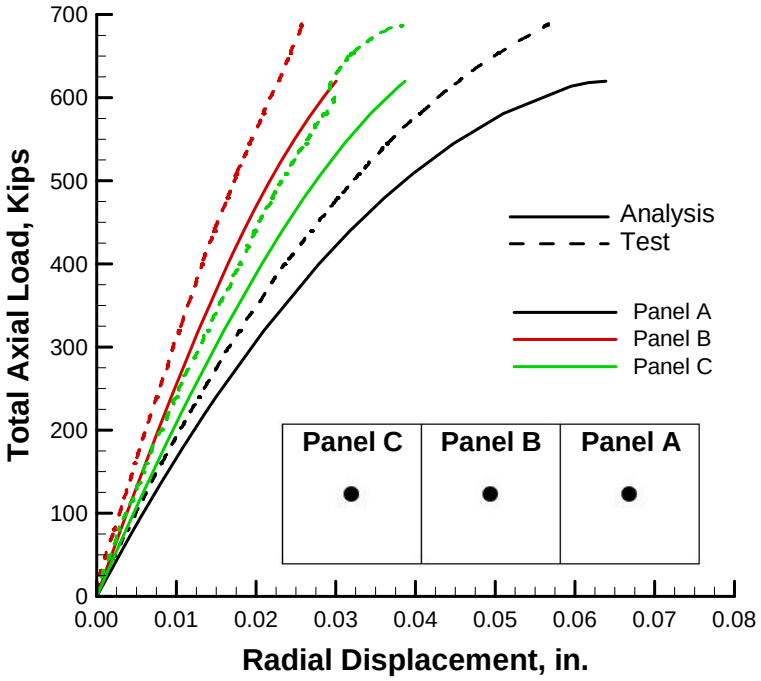

Figure 4.3. Measured and predicted load versus radial displacement response of TA01 at the center of each panel.

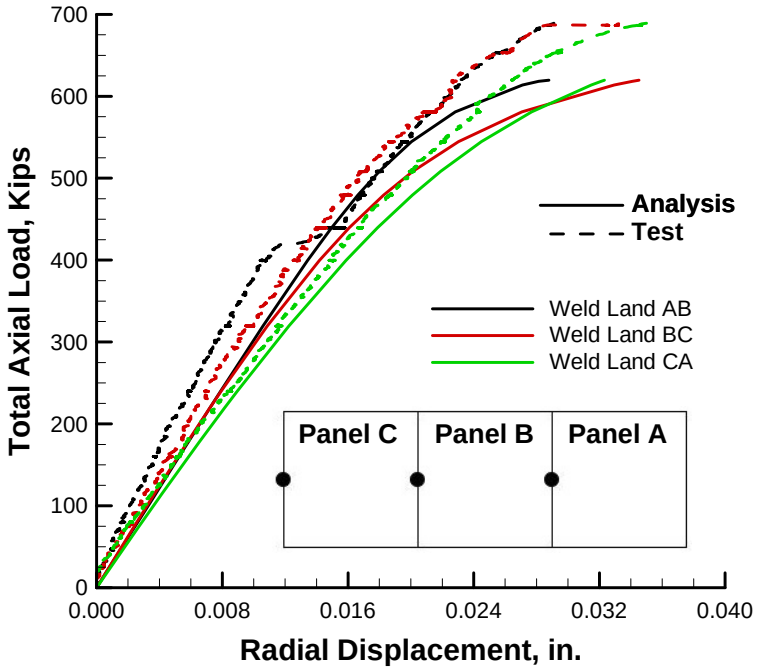

Figure 4.4. Measured and predicted load versus radial displacement response of TA01 at the center of each longitudinal weld land.

Typical predicted and measured prebuckling, buckling, and postbuckling radial displacement response curves for the center of panel A and at the center of weld land AB are shown in Fig. 4.5 to illustrate the typical displacement response characteristics during the buckling event and postbuckling range of loading. Predicted and measured buckling, initial postbuckling, and deep post buckling (end of test) points are indicated on the curves with filled and open square, circle, and triangle symbols, respectively. The results indicate a sudden reversal in the displacements from radially outward at buckling (square symbols) to radially inward at initial postbuckling (circle symbols), and correspond to the buckling of the test article wall. Upon further loading into the postbuckling range, the predicted displacements increase with maximum inward displacements of 2.0 inches occurring at the AB weld land and are accompanied by a significant change in the full-field displacement pattern (shown in Section 4.2.2). In contrast, the corresponding measured postbuckling displacements indicate little to no change in displacements. The difference in the postbuckling full-field displacement response will be presented in Section 4.2.2. A photo of the buckled test article is shown in Fig. 4.6.

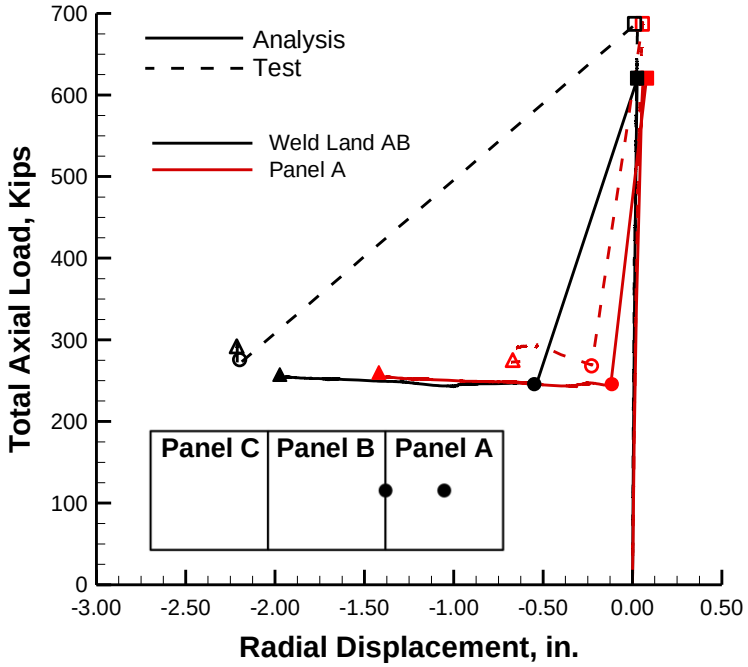

Figure 4.5. Measured and predicted load versus radial displacement response of TA01 at the center of panel A (D246CR) and at the center of weld land AB (D243BR).

Overall, the predicted load versus radial displacement response characteristics are similar to the measured results. However, the predicted prebuckling radial displacements are, in many cases, larger than the corresponding measured displacements.

Figure 4.6. TA01 after global buckling.

4.2.2 Full-Field Displacement Contours

Predicted and measured full-field prebuckling, buckling, and postbuckling displacement contours are presented in this section. First, selected axial and radial full-field prebuckling, buckling, and postbuckling displacement contours obtained from low-speed DIC systems are presented and compared to initial pretest predictions. Dashed vertical lines are shown in the contour plots at 60°, 180°, and 300° and correspond to weld lands AB, BC, and CA, respectively. Then, high-speed DIC contours obtained during the collapse response of the test article are presented. Finally, measured radial displacement versus time response curves are presented that illustrate the transient deformation response and structural damping characteristics of the test article.

Low-Speed Digital Image Correlation Displacement Measurements

Estimates of the low-speed DIC measurement error for the axial, u, and radial, w, displacement measurements are presented in Figs. 4.7-a and 4.7-b, respectively, and are estimated from a DIC measurement noise of ±0.006 inches in the axial u displacements and ±0.015 inches in the radial w displacements. These levels of noise are typical for this type of DIC system, set-up parameters, and calibration method used. Note that data are missing in four locations around the circumference of the test article due to load lines obstructing the FOV.

Selected axial u and radial w displacement contours are presented in Figs. 4.8 through 4.14 and include predicted and measured results from three prebuckling load levels and two postbuckling load levels. Prebuckling u and w displacements at 159.9 Kips (approximately 22% P_{cr}) are shown in Figs. 4.8 and 4.9, respectively. The predicted u displacements indicate a relatively uniform distribution with slightly lower displacements near the weld lands. Overall, the corresponding measured displacements show a similar uniform distribution, however, slight discontinuities in the data exist between adjacent DIC systems due to a camera synchronization error. In addition, some localized variation is observed and is attributed to the inherent measurement noise (see Fig. 4.7-a). The predicted w displacements, Fig. 4.9-a, indicate the development of a periodic distribution of inward and outward radial deformations that are somewhat symmetric within each panel segment. In addition, a pronounced inward ellipse-shaped dimple appears at the mid-length of panel A at the 18° circumferential location. The corresponding measured displacements in Fig. 4.9-b are within the measurement noise for the magnitude of these displacements and thus no correlation can be made.

Predicted radial displacement contours at 319.8 Kips (approximately 44% P_{cr}) are shown in Fig. 4.10-a and indicate further growth of the ellipse-shaped inward dimple in panel A with a maximum amplitude of 0.006 inches. The corresponding measured displacement contours in Fig. 4.10-b still remain within the noise of the DIC measurement. The u displacement pattern at this load level is similar to those shown in Fig. 4.8.

As the applied axial load increases up to the buckling load of the test article, the predicted and measured axial displacement continues to exhibit a relatively uniform distribution around the circumference with slight variations near the weld land (see Fig 4.11). The predicted and measured radial displacement contours indicate significant localization of the deformations near the location of buckling initiation. In particular, the predicted radial displacements in Fig. 4.12a show a marked increase in the amplitude of the inward

dimple to 0.070 inch. The analysis results predict the initiation of buckling to occur at this single dimple in panel A. The measured results indicate the formation of a second ellipse-shaped inward dimple at the mid-length of panel C at the 260° circumferential location where initiation of buckling was observed during the test (high-speed DIC contours will be presented herein that confirm this result). The amplitude of this dimple is approximately 0.05 inch.

The difference in the location of buckling initiation is not unexpected based on the fact that the buckling response of compression loaded cylinders can be extremely sensitive to a multitude of variables including initial geometric imperfections, variations in loading and boundary conditions, and variations in material properties and as-built versus as-designed dimensions. More importantly, the results do indicate good agreement in the overall character of the prebuckling displacement response.

Initial postbuckling and deep postbuckling radial displacement contours are shown in Figs. 4.13 and 4.14, respectively. The results indicate large-magnitude inward buckles have developed throughout the test article during the collapse response with maximum postbuckling displacements on the order of –1.4 to –1.6 inches near the weld lands. The predicted initial postbuckling displacements exhibit a uniform periodic distribution of buckles as compared to a nonuniform distribution of buckles observed in the measured results. This difference in behavior is attributed to the use of linear elastic material properties in the finite-element model that cannot account for the material yielding that occurred in the test article. More specifically, the predicted transient buckling response (results not presented herein) exhibited a short-wavelength displacement pattern similar to the one observed in Fig. 4.13-b during the initial stages of the transient collapse response but as the transient collapse continued, these small buckles were predicted to coalesce into larger buckles as shown in Fig. 4.13-a. In contrast, the test article experienced material yielding in regions that exhibit large magnitude bending strains associated with the short-wavelength buckles during the early stages of collapse, which appears to have prohibited the movement and coalescence of these buckles.

As loading continues into the deep postbuckling range of loading, the predicted radial displacement response exhibits a coalescence of some of the smaller buckles into larger buckles and a significant increase in the magnitude of the inward displacements as shown in Fig. 4.14-a. In contrast, the measured displacement pattern remains unchanged from the initial postbuckling pattern shown in Fig. 4.13-b with only a slight increase in the amplitude of the inward displacements. Post-test inspection of the test article indicated permanent deformations associated with material yielding in the areas of large bending strains.

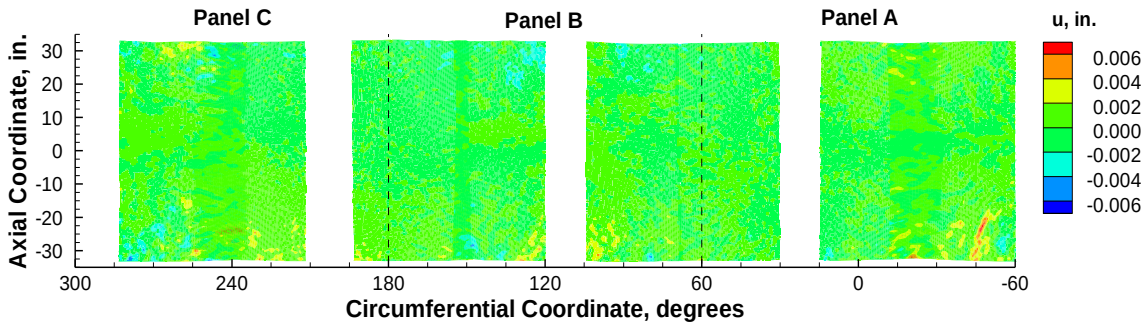

a) Axial displacement *u* measurement noise.

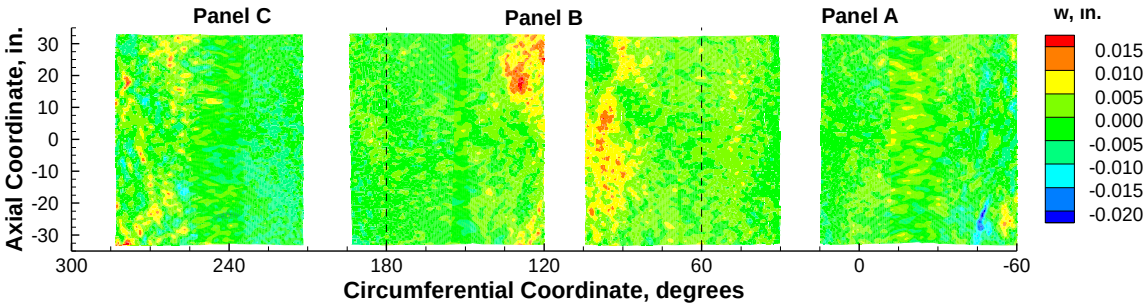

b) Radial displacement *w* measurement noise.

Figure 4.7. DIC noise signature for *u* and *w* displacement measurements.

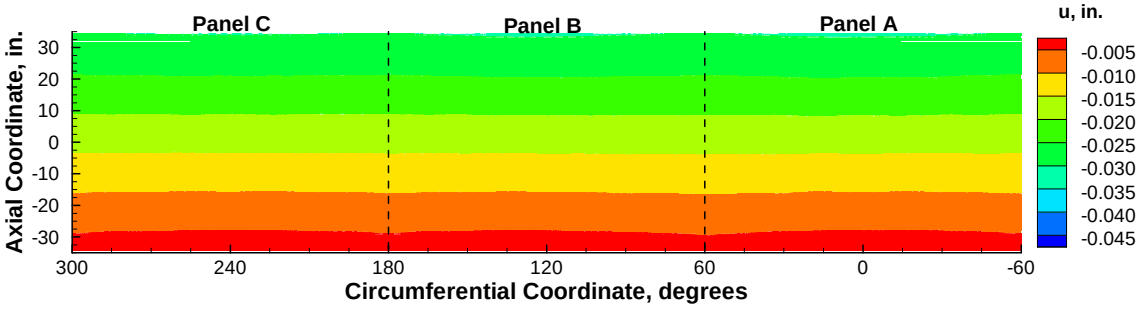

a) Finite-element prediction.

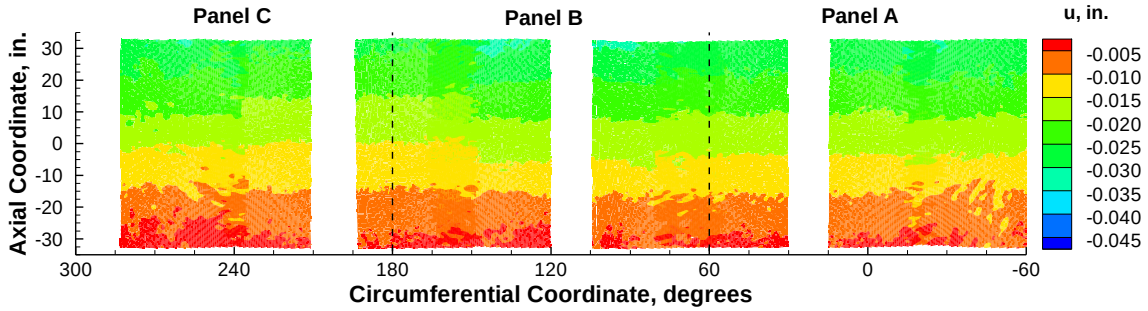

b) DIC.

Figure 4.8. Predicted and measured axial displacement (*u*) contours at 159.9 Kips (22.0% P_{cr}).

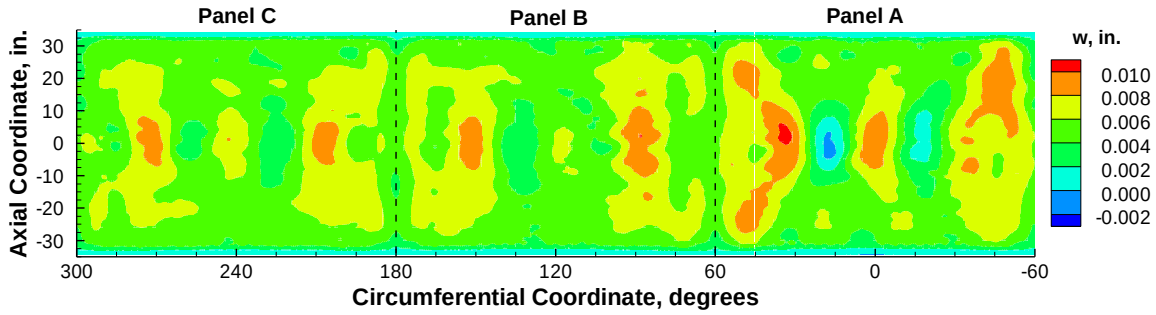

a) Finite-element prediction.

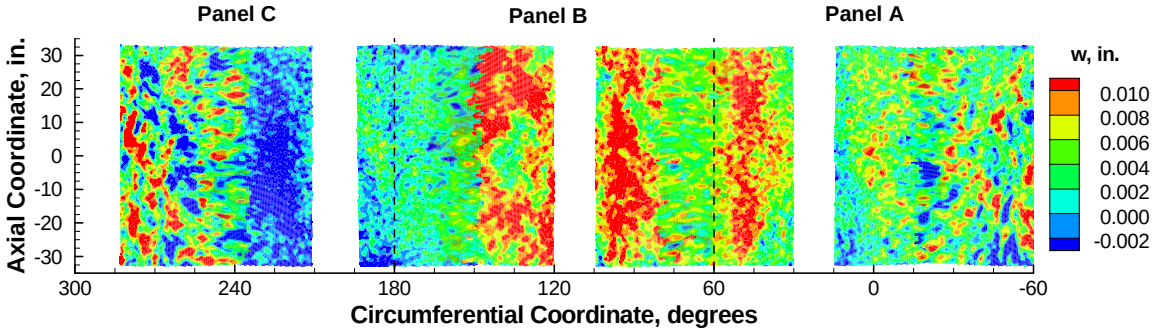

b) DIC.

Figure 4.9. Predicted and measured radial displacement (w) contours at 159.9 Kips (22.0% P_{cr}).

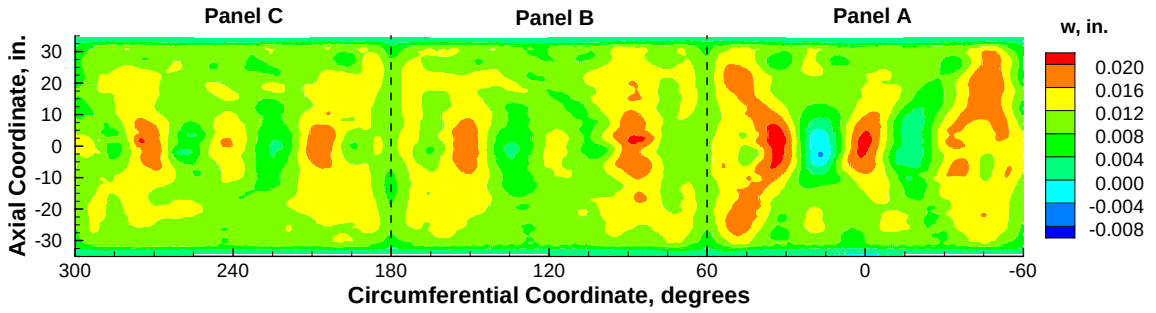

a) Finite-element prediction.

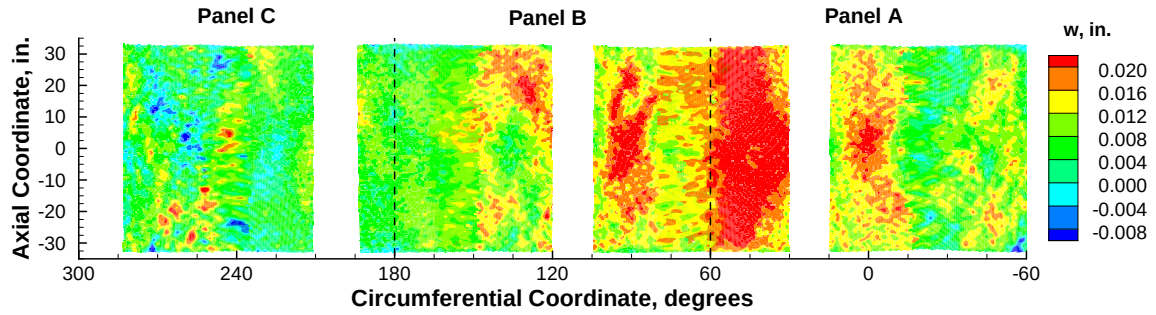

b) DIC.

Figure 4.10. Predicted and measured radial displacement (w) contours at 319.8 Kips (44.0% P_{cr}).

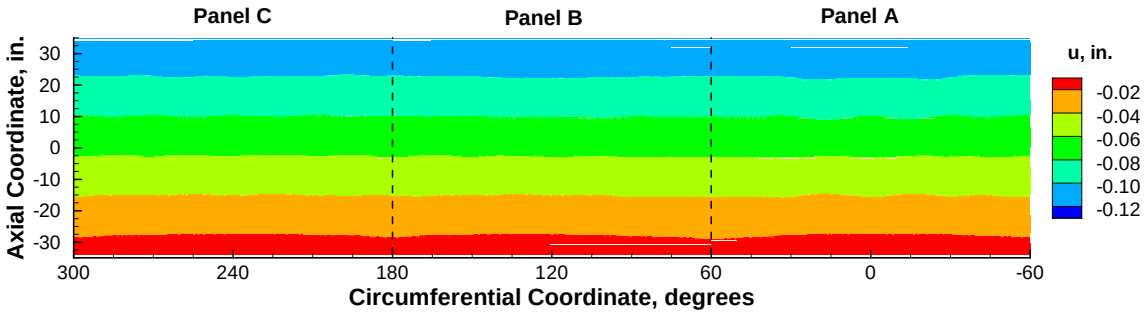

a) Finite-element prediction at buckling load of 619.8 Kips (85.3% P_{cr}).

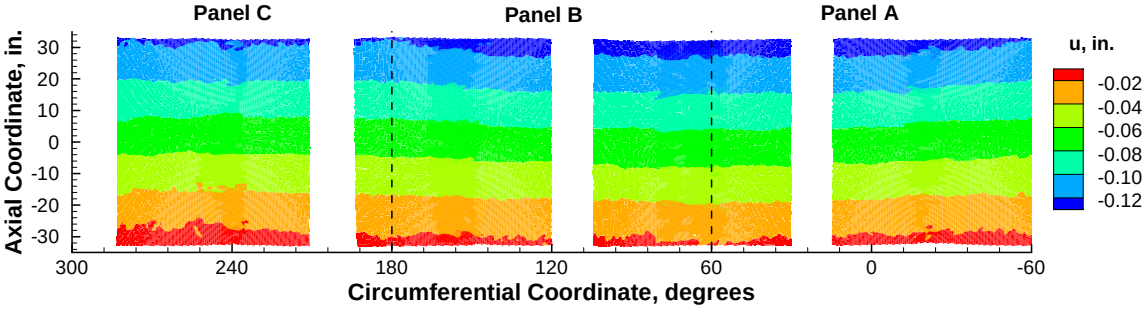

b) DIC at buckling load of 689.2 Kips (94.8% P_{cr}).

Figure 4.11. Predicted and measured axial displacement (u) contours incipient to buckling.

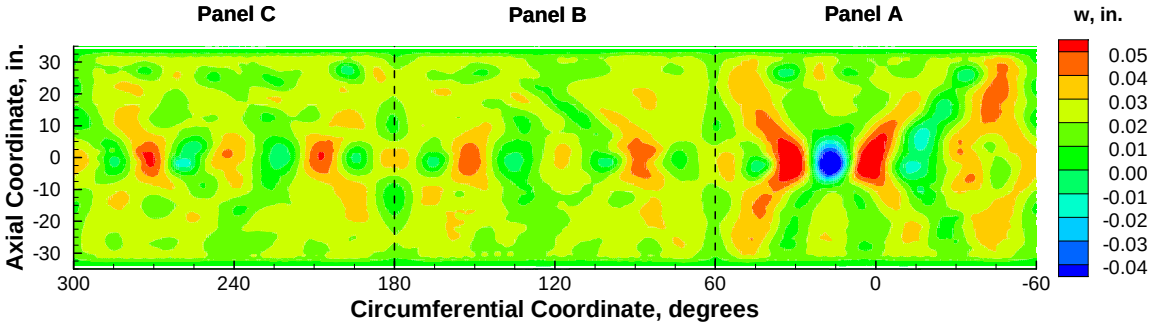

a) Finite-element prediction at buckling load of 619.8 Kips (85.3% P_{cr}).

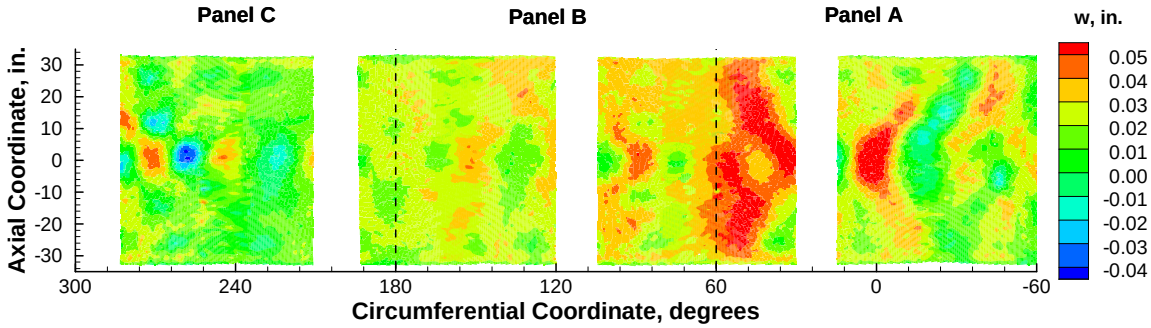

b) DIC at buckling load of 689.2 Kips (94.8% P_{cr}).

Figure 4.12. Predicted and measured radial displacement (w) contours incipient to buckling.

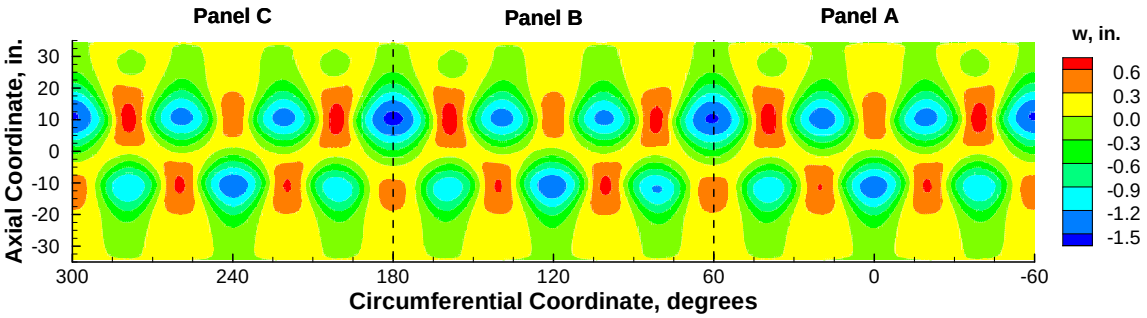

a) Finite-element prediction at initial postbuckling load of 241.4 Kips (33.2% P_{cr}).

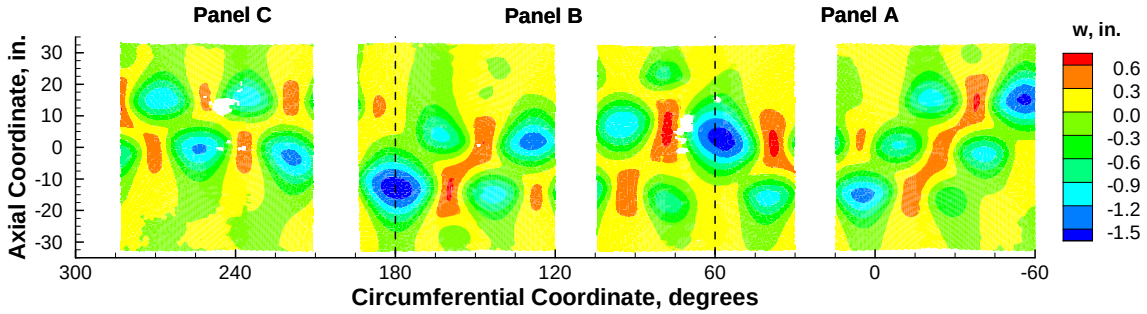

b) DIC at initial postbuckling load of 265.5 Kips (36.5% P_{cr}).

Figure 4.13. Predicted and measured initial postbuckling radial displacement (w) contours.

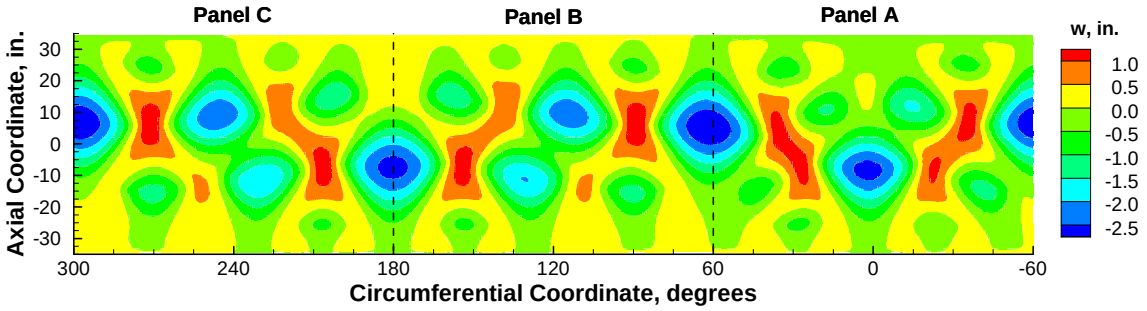

a) Finite-element prediction at deep postbuckling load of 207.2 Kips (28.5% P_{cr}).

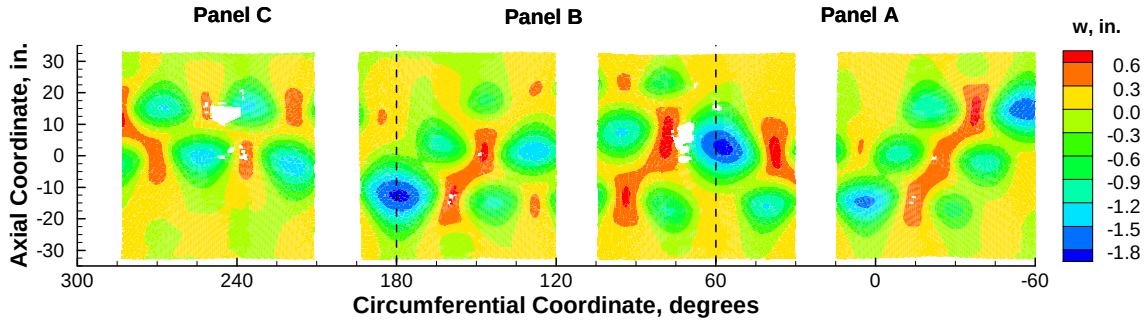

b) DIC at deep postbuckling load of 251.5 Kips (34.6% P_{cr}).

Figure 4.14. Predicted and measured deep postbuckling radial displacement (w) contours.

High-Speed Digital Image Correlation Displacement Measurements

Selected high-speed DIC displacement contours are presented to illustrate the initiation of buckling and unstable transient collapse response of the test article. First, *u*-*v*-based displacement magnitudes are shown from four 2D high-speed DIC systems. The *u* and *v* components of the displacement are used to give a qualitative indication of where the buckling deformations develop and how they propagate over time as described in Section 2.5.4. Then, data from one high-speed 3D DIC system are presented. The 3D DIC system was positioned between load lines 1 and 2 with a FOV from approximately 15° to 70° around the circumference of the test article, as shown in Fig. 2.13.

The displacement contours are presented in Fig. 4.15 with contours superposed on DIC reference images of the test article. Blue/purple contours correspond to maximum amplitude radial displacements and the red/orange contours correspond to minimum amplitude radial deformations. Incipient buckling contours are shown for $t = 0.0$ sec and shows a single ellipse-shaped buckle at the 260° circumferential location in Fig. 4.15-a and corresponds to the initial dimple shown in Fig. 4.12-b from the low-speed DIC.[vii] The other high-frequency variations in the displacement contours are associated with the inherent measurement noise. At time $t = 0.0009$ sec, the single ellipse-shaped buckle begins to grow in size and amplitude. After 0.0049 seconds have elapsed, additional buckles have formed in panel C. The formation and propagation of additional buckles into panels A and B continues throughout the global collapse event (e.g., Figs. 4.15-c–4.15-e) until a stable postbuckling configuration is obtained as shown in Fig. 4.15-f. The postbuckling contours shown in Fig 4.15-f correlate well with the corresponding low-speed DIC contours presented in Fig. 4.13-b.

Radial displacement data were obtained from one high-speed 3D DIC system and were used to characterize displacement versus time response for six locations on panel A as shown in Fig. 4.16-a. Points A and D are located on the AB weld land (60° circumferential location) and points C and F are at the 22.2° circumferential location. The corresponding radial-displacement versus time response curves are shown in Fig. 4.16-b. Buckling initiated in panel C, as described previously, and rapidly propagated around the circumference of the test article. From this camera view, the buckling first appears at the right side of the FOV (e.g., points C and F) and propagates to the left of the image towards the AB weld land (e.g., points A and D). This can be seen in the displacement-time history curves in which displacements first appear at measurement points C and F followed by B and E, and finally at A and D. The displacement pattern and magnitudes correlate well with the low-speed contour data and indicate maximum radial displacements on the order of 1.75 inches at the AB weld land. The propagation speed of the buckling deformations can be estimated based on the phase difference between the various measurement points. Specifically, the data indicate that it took approximately 0.001 seconds for the buckling deformations to propagate from point C to point A, a distance of approximately 31.8 inches, corresponding to a propagation speed of 31,800 in/sec.

[vii] Note: $t = 0.0$ sec. is an arbitrary time reference used to determine elapsed time throughout the transient collapse response.

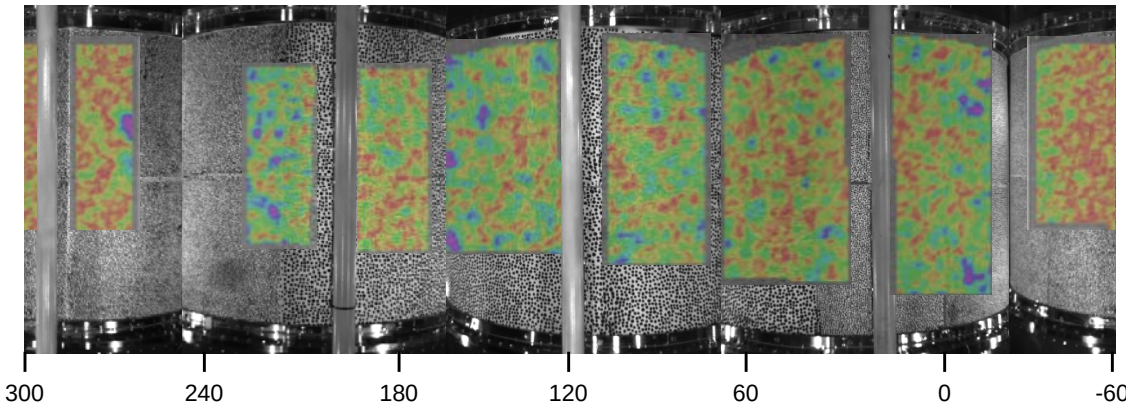

a) Incipient buckling t = 0.0 sec.

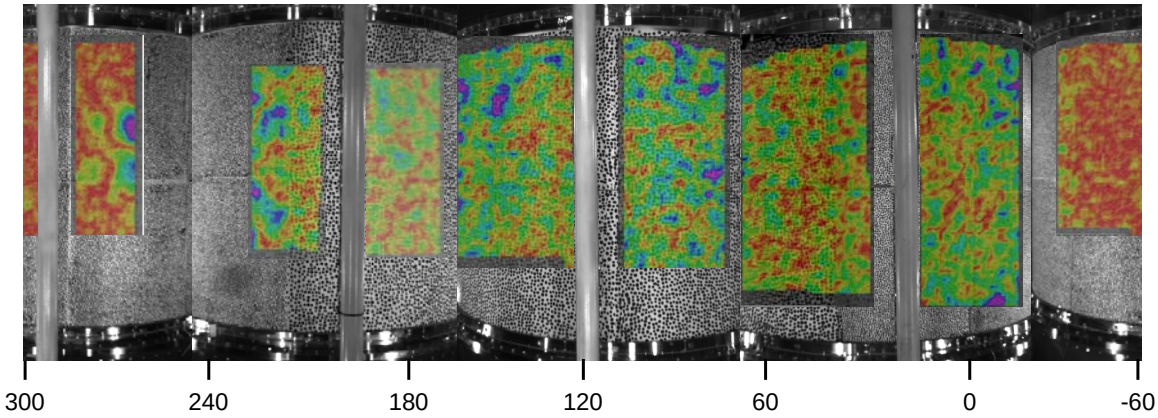

b) Initial buckling t = 0.0009 sec.

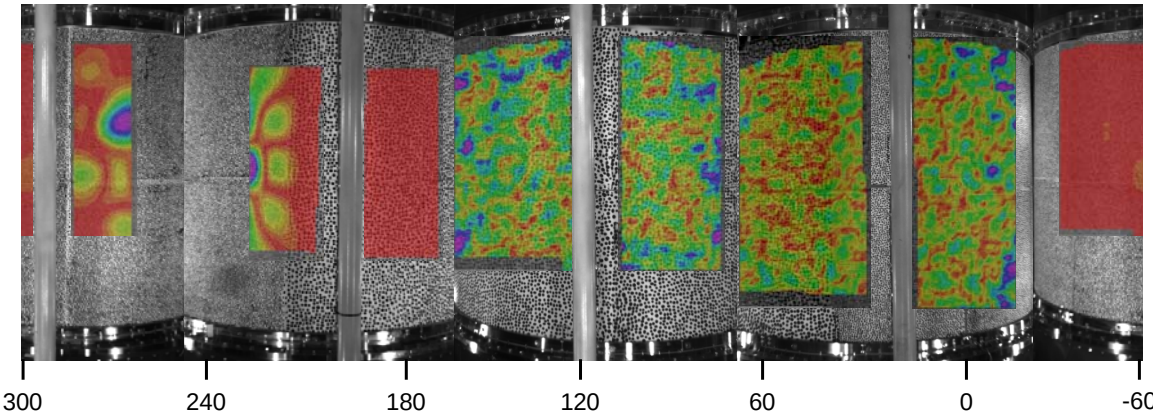

c) Buckling t = 0.0049 sec.

Figure 4.15. Displacement contours from 2D high-speed DIC indicating the initiation and propagation of buckling deformations in TA01.

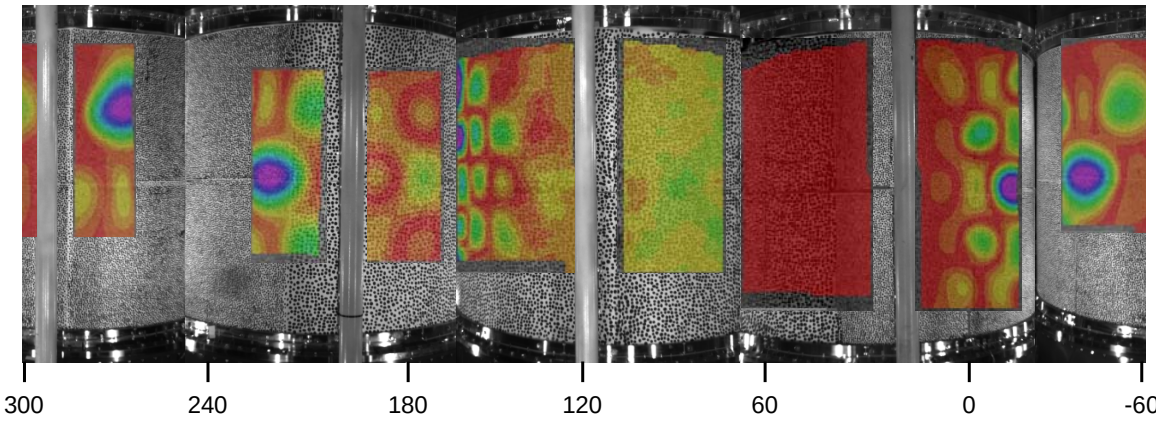

d) Buckling t = 0.0121 sec.

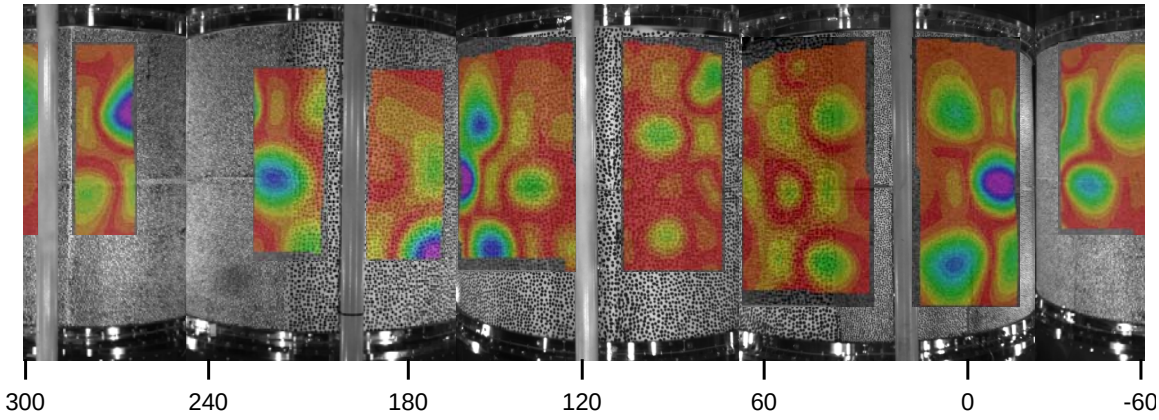

e) Buckling t = 0.0191 sec.

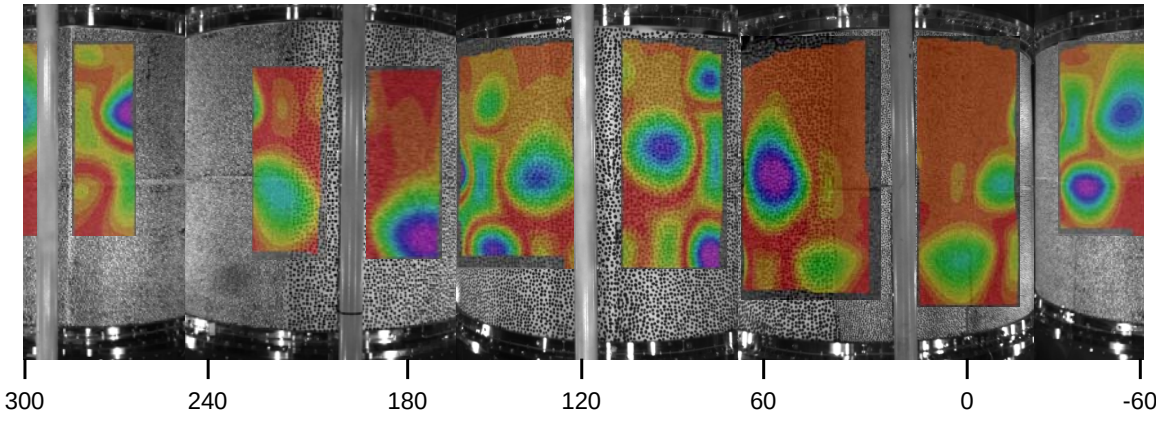

f) Postbuckling t = 0.0360 sec.

Figure 4.15. Concluded.

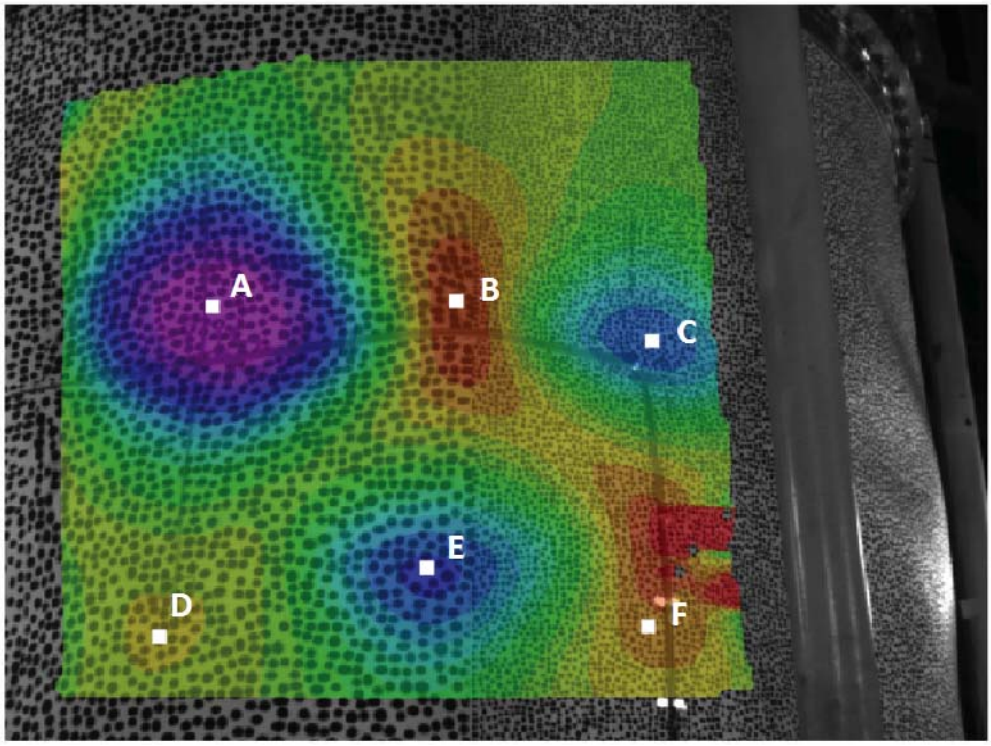

a) Radial displacement contour plot from 3D DIC and measurement points.

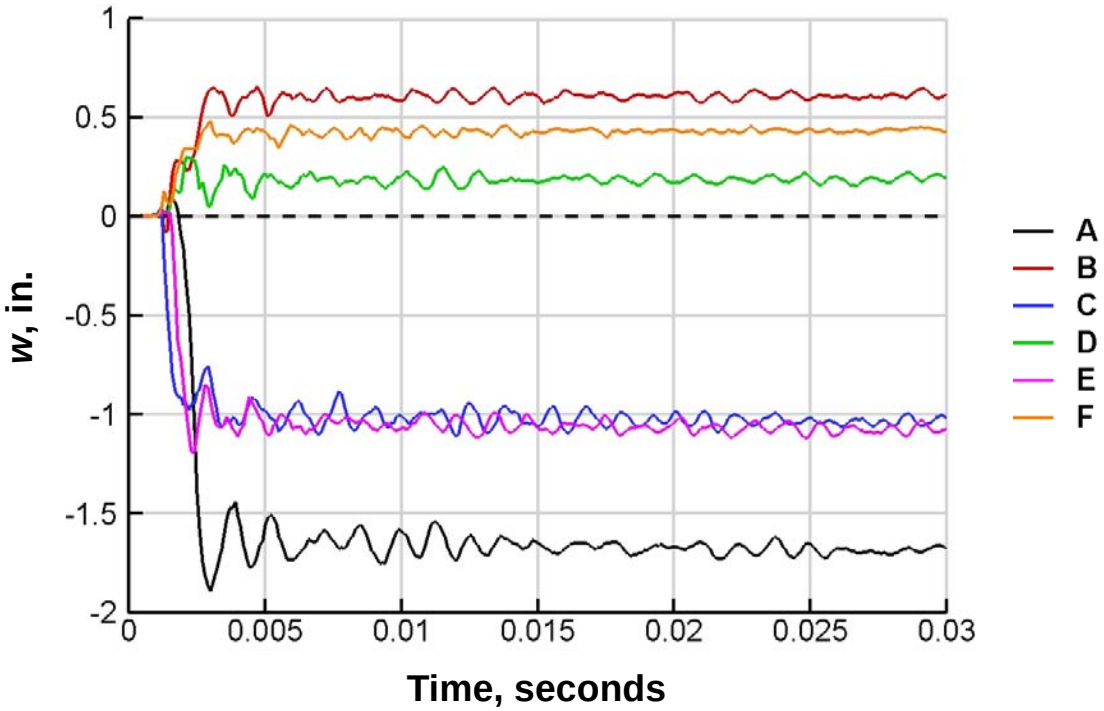

b) Radial displacement versus time response.

Figure 4.16. Measured radial displacements at selected locations on panel A of TA01 during the collapse response.

4.2.3 Load versus Axial Strain Response

Predicted and measured load versus axial prebuckling strain response curves are presented in Figs. 4.17 through 4.24. The buckling and postbuckling strains have been omitted from the figures for clarity. In addition, schematics of strain gage locations are provided in each figure.

Back-to-back strain gage results from skin pockets and axial stiffeners near the centers of panels A, B, and C, are shown in Figs. 4.17, 4.18, and 4.19, respectively. Each figure contains analysis and test results from the center of a skin pocket near the center of each panel, corresponding to the green and blue lines, and results from an axial stiffener adjacent to each of these skin pockets, corresponding to the red and black lines in the figures. The results indicate that the strain response is, for the most part, linear up to buckling with average strains that range from −1550 micro-strain ($\mu\varepsilon$) to −2010 $\mu\varepsilon$. A slight amount of bending is observed in panels A and C as indicated by the divergent load versus strain response curves, and this behavior is predicted accurately in the preliminary analysis. However, the predicted results show a rapid increase in bending strain in panel A at the maximum load, corresponding to the initiation of buckling near the center of the panel as seen in the predicted displacement contours presented in Fig 4.12-a.

Back-to-back strain gage results from weld lands AB, BC, and CA and from axial stiffeners adjacent to the weld lands, are shown in Figs. 4.20, 4.21 and 4.22, respectively. Each figure contains analysis and test results from the center of each weld land, corresponding to the red and black lines, and results from longitudinal stiffeners adjacent to each of the weld lands, corresponding to the green and blue lines in the figures. The results indicate similar strain behavior as was seen in the skin pockets and stiffeners presented in Figs. 4.17–4.19 previously. In particular, the strain response curves are linear up to the buckling point and range from −1520 $\mu\varepsilon$ to −1910 $\mu\varepsilon$.

Two additional load versus axial strain plots are shown in Figs. 4.23 and 4.24 in order to investigate further the initiation of buckling in the test article. More specifically, the preliminary analysis results predicted buckling to initiate near the mid-length of panel A as shown in Fig. 4.12-a, however, the low-speed and high-speed DIC contours indicate that buckling initiated in panel C as shown in Figs. 4.12-b and 4.15-b. Thus, strain gage data close to these two regions of interest are presented next. Predicted results from panel A near the predicted buckling initiation sight are presented in Fig. 4.23 and show strain reversal in several of the skin and stiffener gages which is consistent with the onset of buckling in that panel. In contrast, the measured strains exhibit only slight change in the rate of divergence in this region prior to the maximum load. Similar results are presented for skin pocket strains near the mid-length of panel C in Fig. 4.24. The measured results exhibit a strain reversal in the outer-surface skin pocket gage and the measured bending strains are slightly larger than the corresponding predicted strains.

For the most part, the predicted strain results correlate well with the measured results and indicate that the load introduction into the test article is predicted accurately. However, predicted stiffener strain near weld land AB (gage 080IRA) is approximately 20–25% greater than the corresponding measurement. Several factors may contribute to this difference and include simplifying assumptions used to model the stiffeners as well as the sensitivity of strain measurements in the presence of local bending gradients. Recall that

in the preliminary analyses the stiffeners were modeled with beam elements and thus accurate strain predictions can be difficult to obtain when local bending and twisting of the stiffener is present. In addition, variations in strain gage position and strain gradients along the stiffener could result in significant differences in strain measurements. Detailed model refinement and sensitivity studies with improved stiffener models shall be conducted in the future to better understand this behavior and modeling sensitivities.

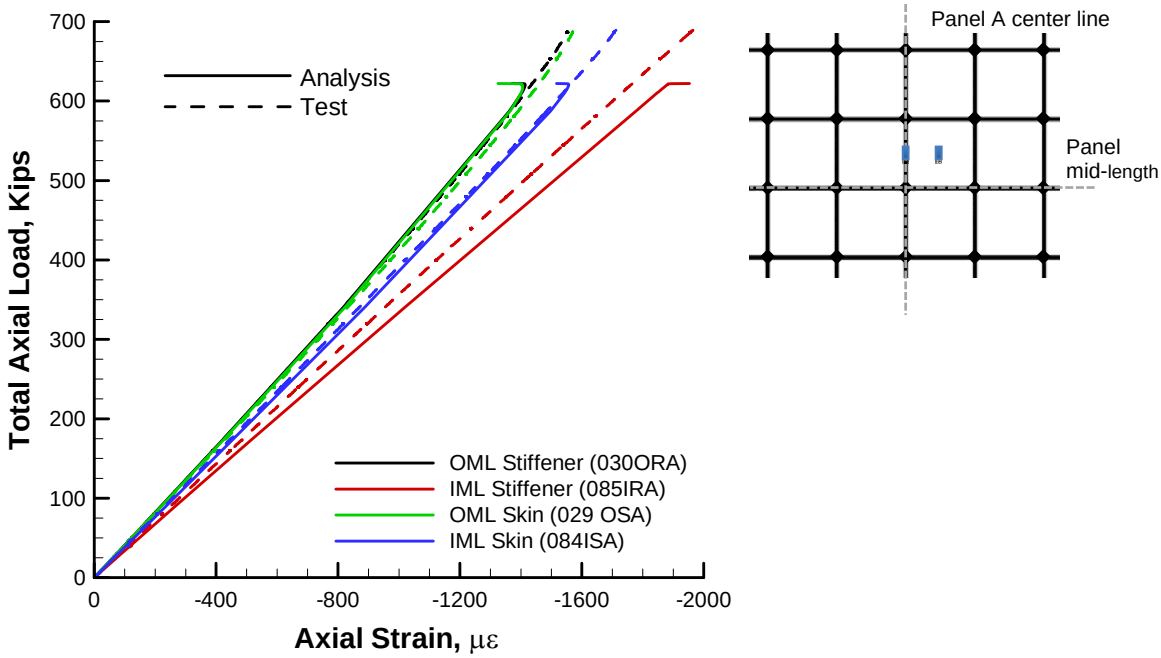

Figure 4.17. Test/analysis correlation of back-to-back axial strains, skin, and adjacent axial stiffener near center of panel A.

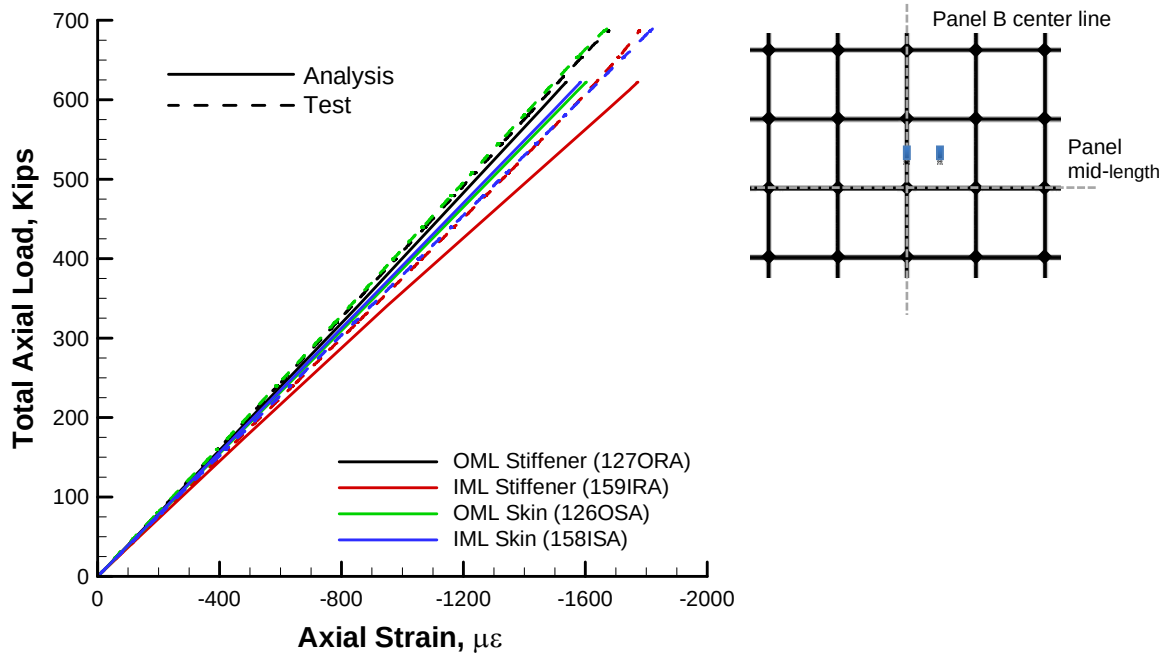

Figure 4.18. Test/analysis correlation of back-to-back axial strains, skin, and adjacent

axial stiffener near center of panel B.

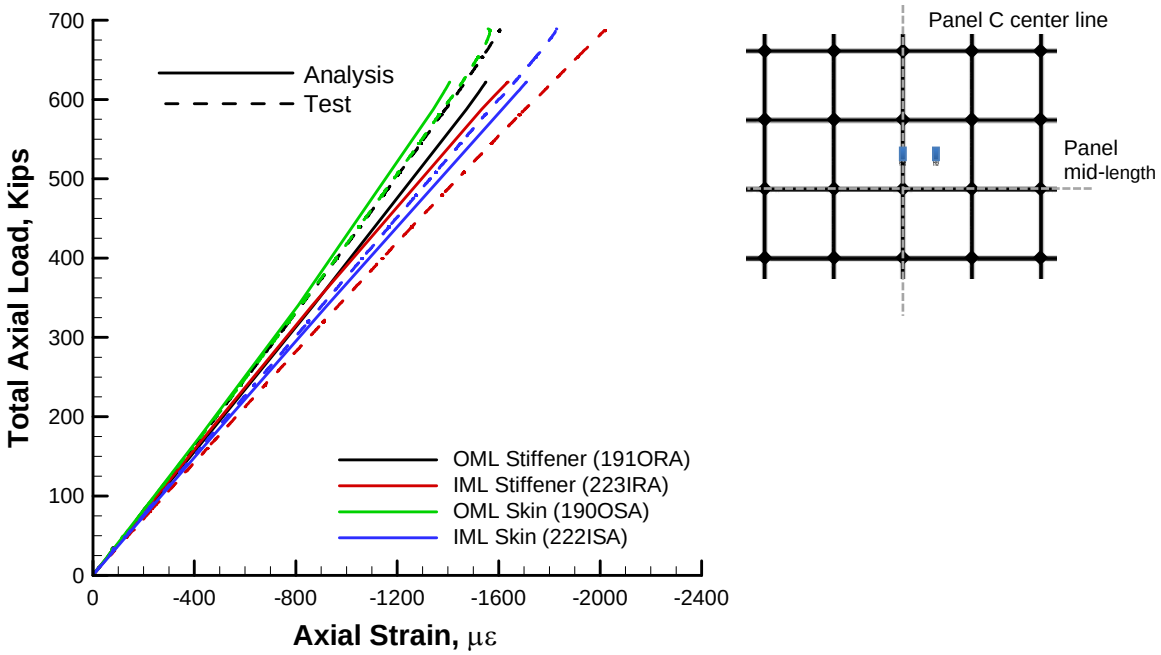

Figure 4.19. Test/analysis correlation of back-to-back axial strains, skin, and adjacent axial stiffener near center of panel C.

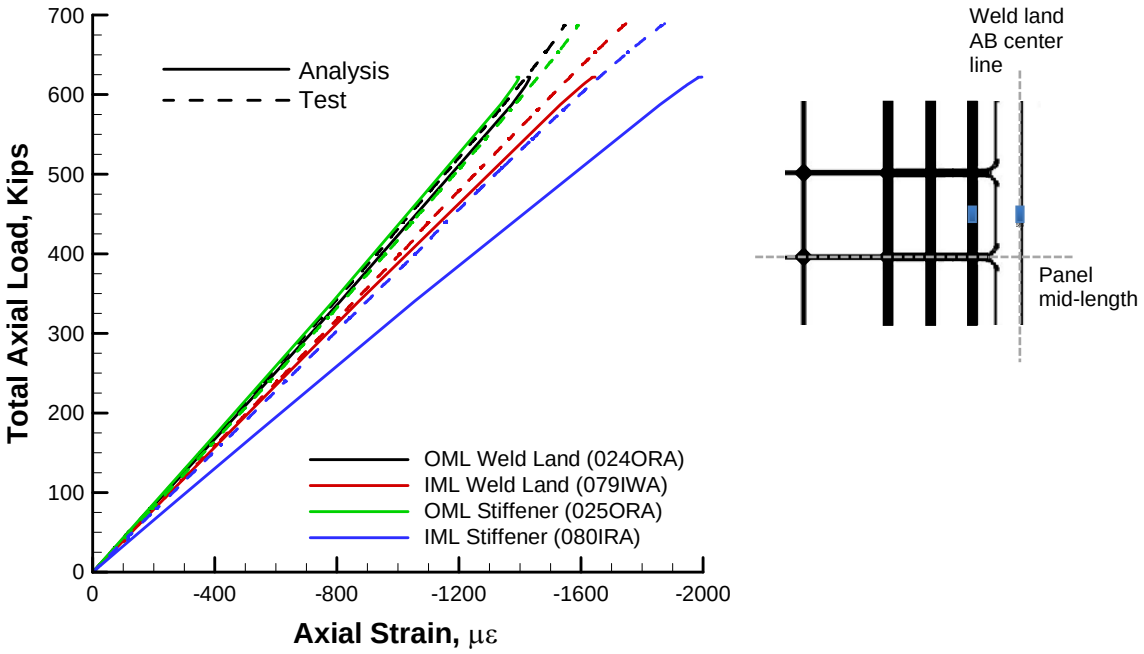

Figure 4.20. Test/analysis correlation of back-to-back axial strains, centers of weld land AB, and adjacent axial stiffener.

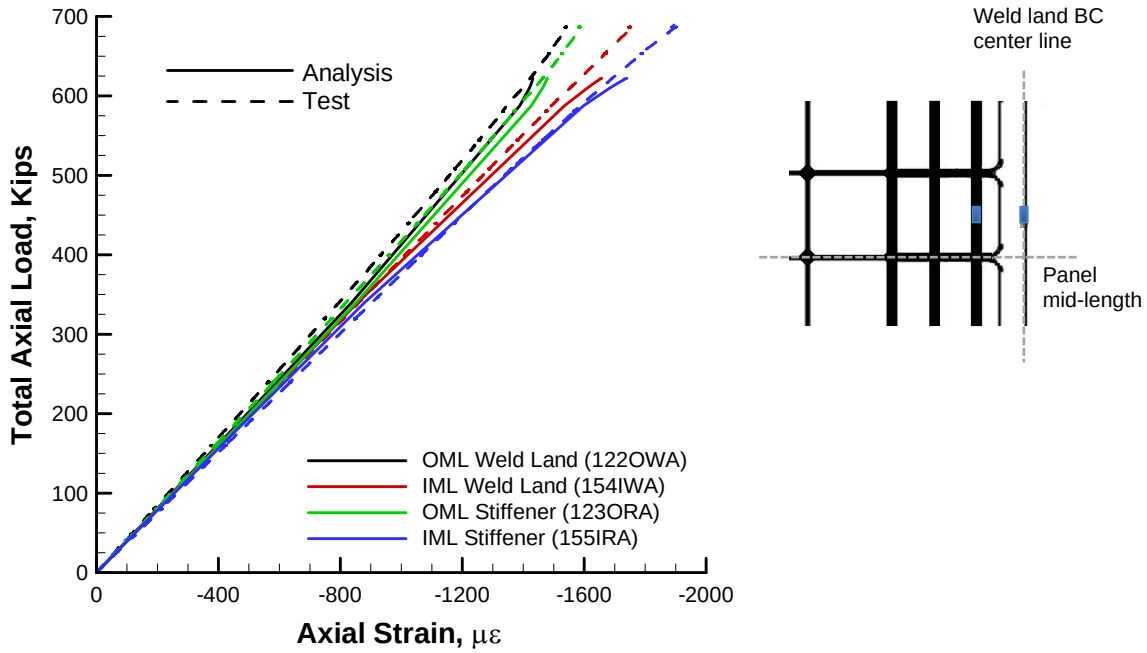

Figure 4.21. Test/analysis correlation of back-to-back axial strains, centers of weld land BC, and adjacent axial stiffener.

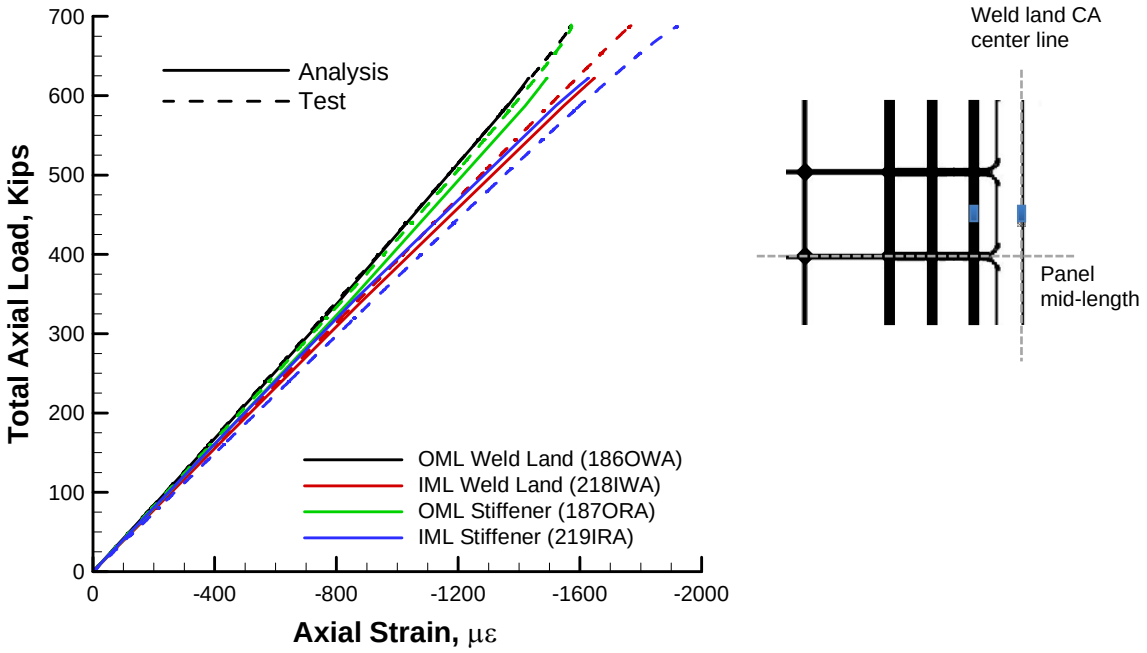

Figure 4.22. Test/analysis correlation of back-to-back axial strains, centers of weld land CA, and adjacent axial stiffener.

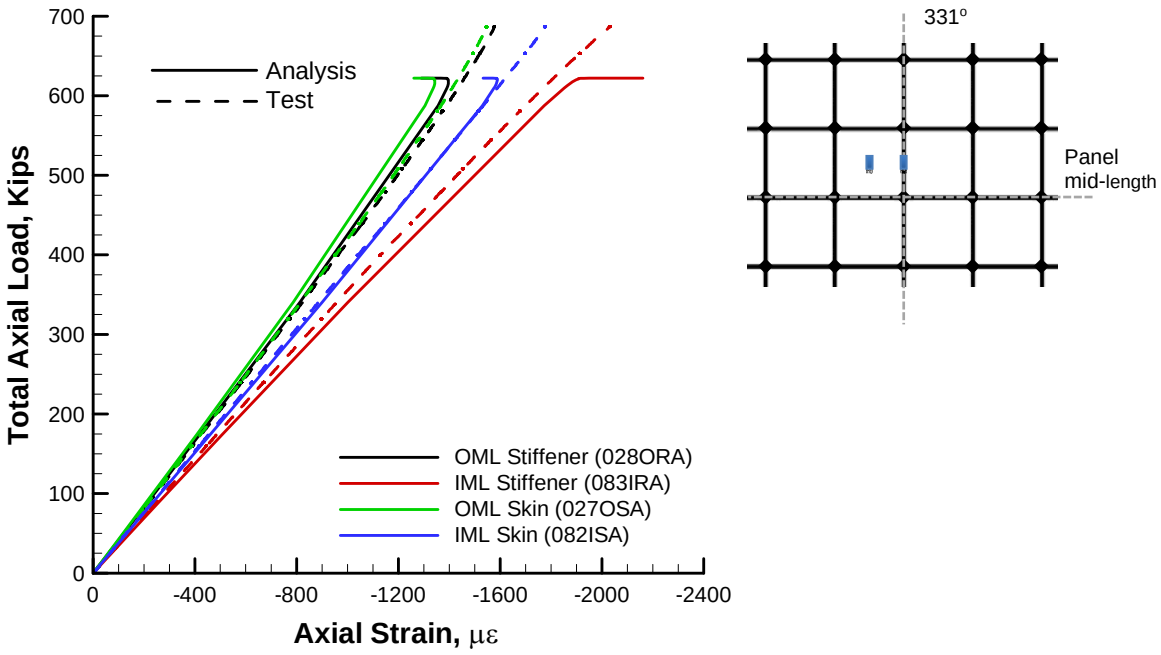

Figure 4.23. Test/analysis correlation of back-to-back axial strains, skin, and adjacent axial stiffener near the predicted buckling initiation site in Panel A.

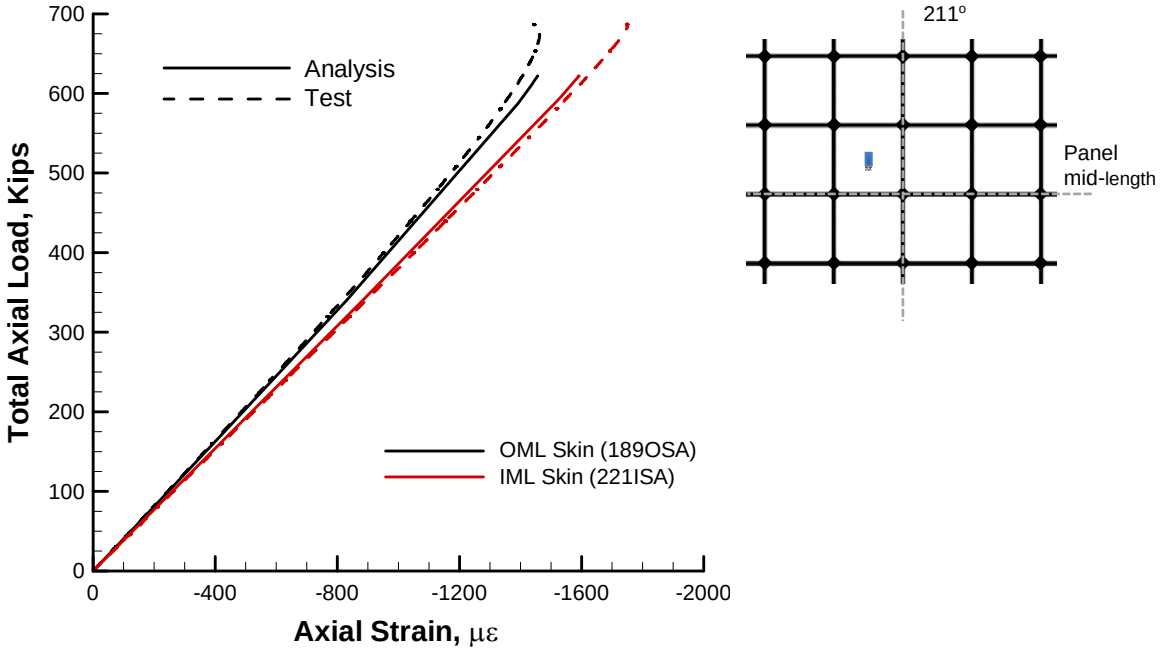

Figure 4.24. Test/analysis correlation of back-to-back axial strains in a skin pocket near the buckling initiation sight in Panel C.

4.2.4 Axial Strain Distribution

Selected plots of the predicted and measured axial membrane strain distribution around the circumference of the test article are presented for selected prebuckling load levels and incipient buckling in Figs. 4.25 through 4.28. Each plot includes data from five different axial stations along the length of the test article including +32.84, +18.0, +2.0, –18.0, and –32.84 inches. The predicted membrane strains are displayed as a solid line and the measured membrane strains from individual strain gages are plotted with open circle symbols. The measured membrane strains are obtained by taking the average of the back-to-back strain gage pairs. The dashed vertical lines at 60°, 180°, and 300° mark the weld land locations. The primary objective of this strain data comparison is to assess the load distribution in the test article and to verify test predictions.

Strain data at load levels of 159.9 Kips (22% P_{cr}), 319.8 Kips (44.0% P_{cr}), 581.4 Kips (79.9% P_{cr}), and incipient buckling are presented in Figs. 4.25 through 4.28. At a load level of 159.9 Kips, the measured strains near the ends of the test article, ±32.84 inches, are uniform across the panel width with an average value of –260 $\mu\varepsilon$ and with small periodic variations of ±10 $\mu\varepsilon$ associated with the alternating skin and stiffener construction. The strains increase in magnitude near the weld lands by approximately 28% to –325 $\mu\varepsilon$. Toward the mid-length of the test article, the strain distribution changes significantly. In particular, the stiffened acreage exhibits larger magnitude strains of –425 $\mu\varepsilon$ as compared to average weld land strains of –390 $\mu\varepsilon$. As loading increases up to 79.9% P_{cr} (581.4 Kips), the strain distributions and correlation trends remain similar to those at 22% P_{cr} (see Figs. 4.26 and 4.27).

Finally, strain distributions at the predicted and the measured buckling load are presented in Fig. 4.28. The predicted strains at 619.8 Kips (predicted buckling load) are displayed as a solid line and the corresponding measured strains are plotted with open circle symbols. In addition, the measured buckling strains at 689.2 Kips (measured buckling load) are presented and displayed as filled square symbols. The strain distributions, for the most part, continue to follow the trends observed at lower prebuckling load levels.

In general, the overall character of the axial strain distribution is predicted accurately, and indicates a periodic distribution associated with the periodic displacement response (see Fig. 4.9-a). However, the predicted incipient buckling axial strains in the weld lands near the ends of test article are between 7% greater (weld land CA) and 18% greater (weld land AB) than the corresponding measured strains (e.g., Figs. 4.28-a and 4.28-e), and may suggest a slight difference between the predicted and as-tested load introduction into the test article in that region.

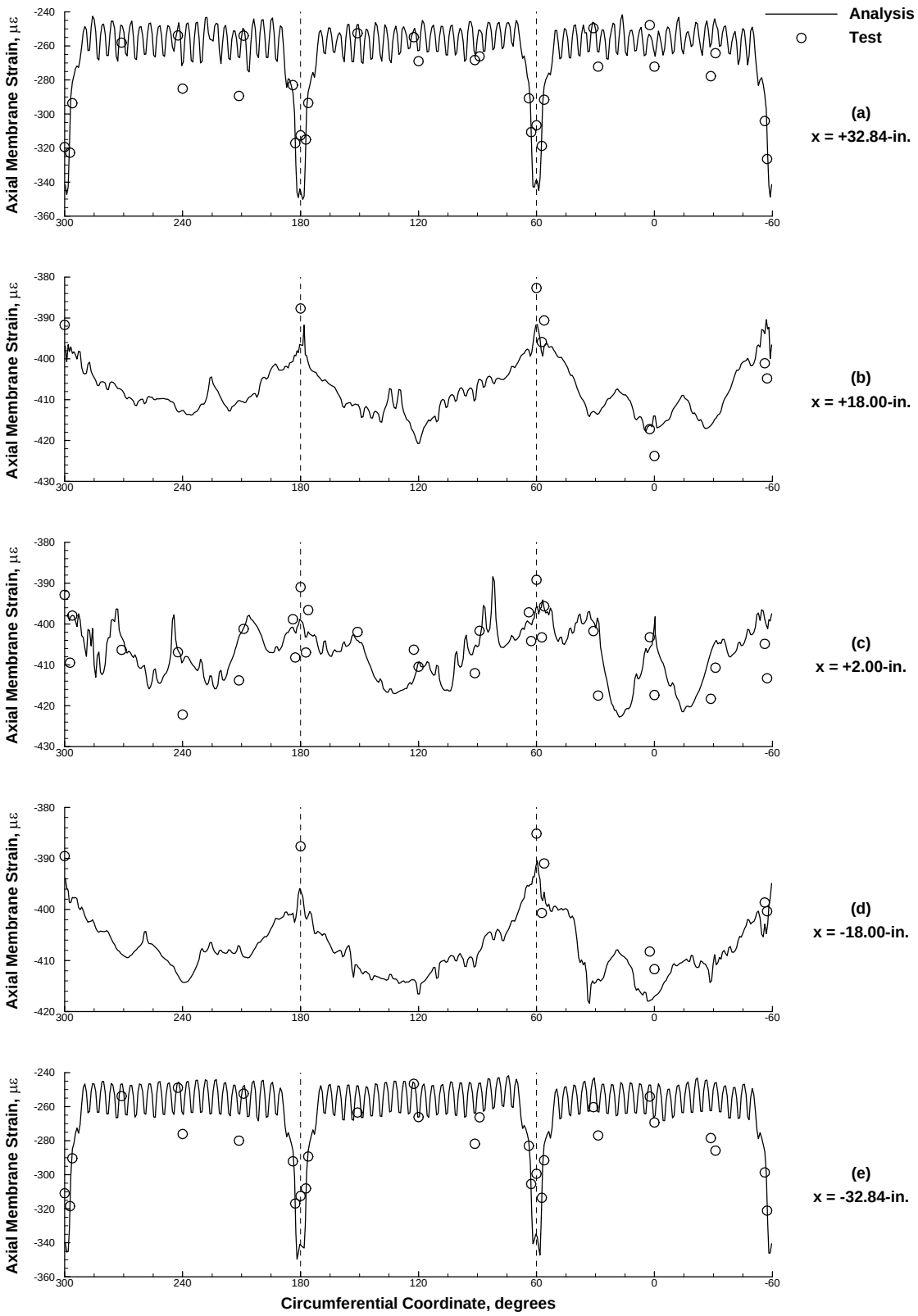

Figure 4.25. Predicted and measured axial membrane strain distribution around circumference, 159.9 Kips (22.0% P_{cr}).

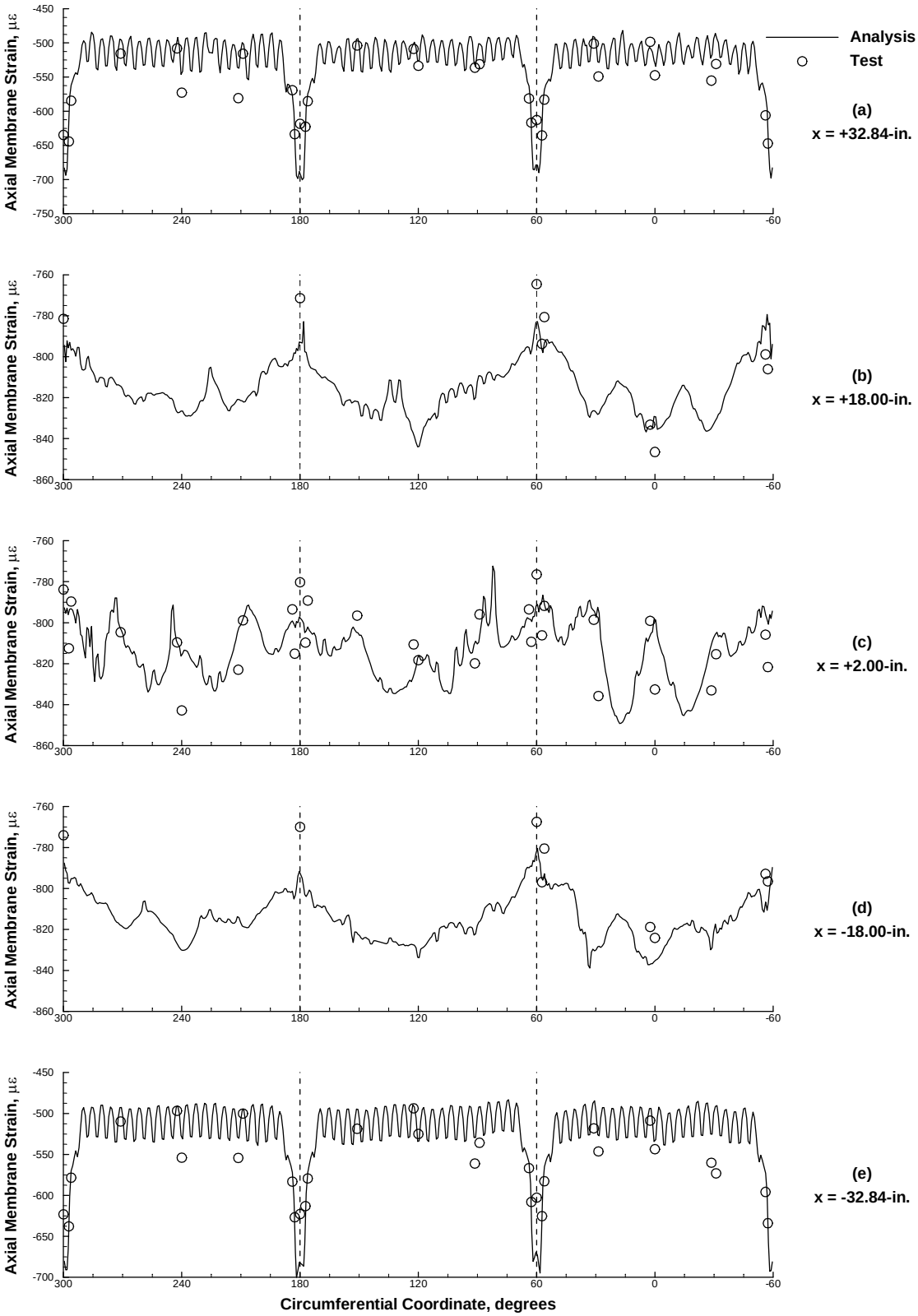

Figure 4.26. Predicted and measured axial membrane strain distribution around circumference, 319.8 Kips (44.0% P_{cr}).

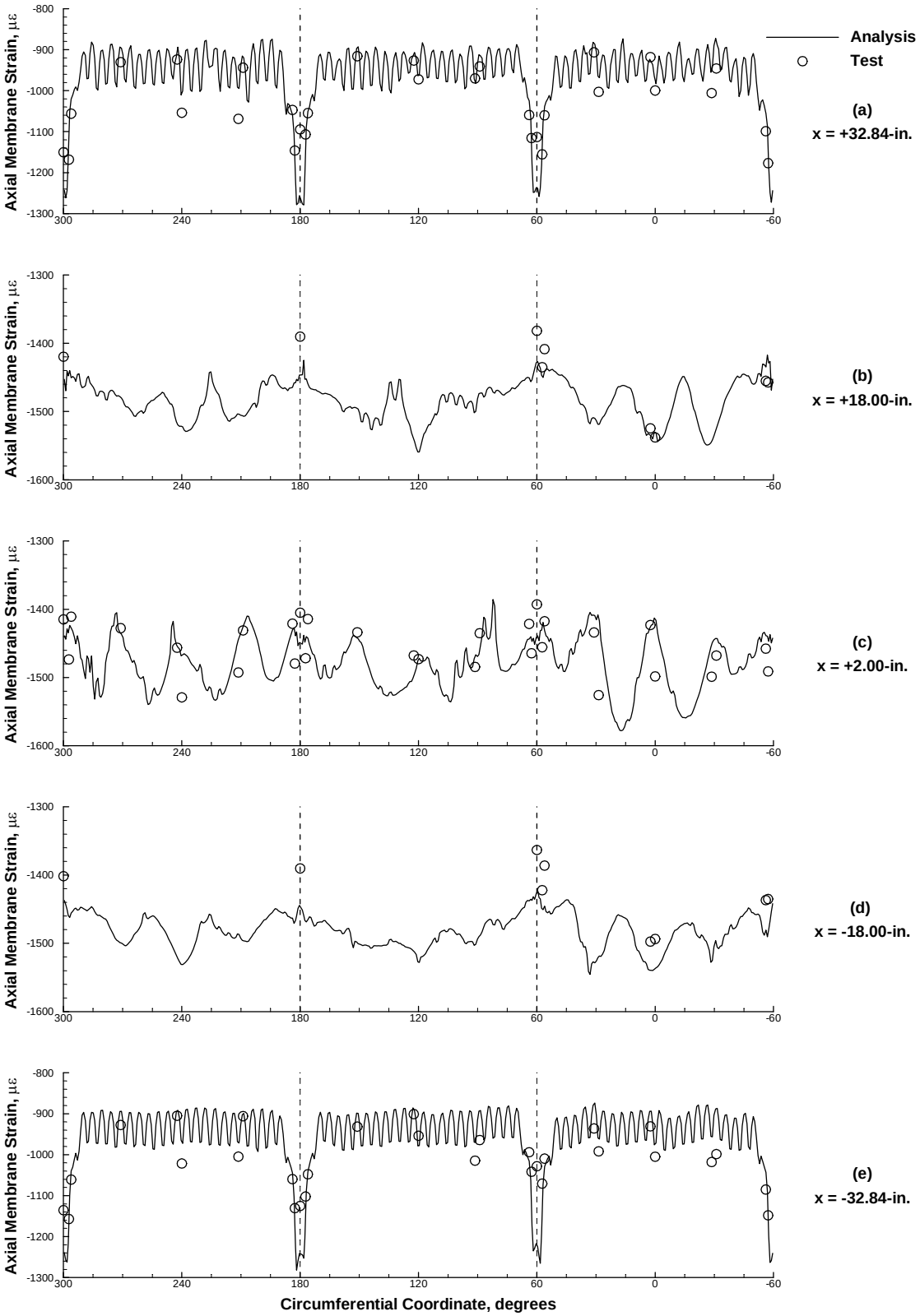

Figure 4.27. Predicted and measured axial membrane strain distribution around circumference, 581.4 Kips (79.9% P_{cr}).

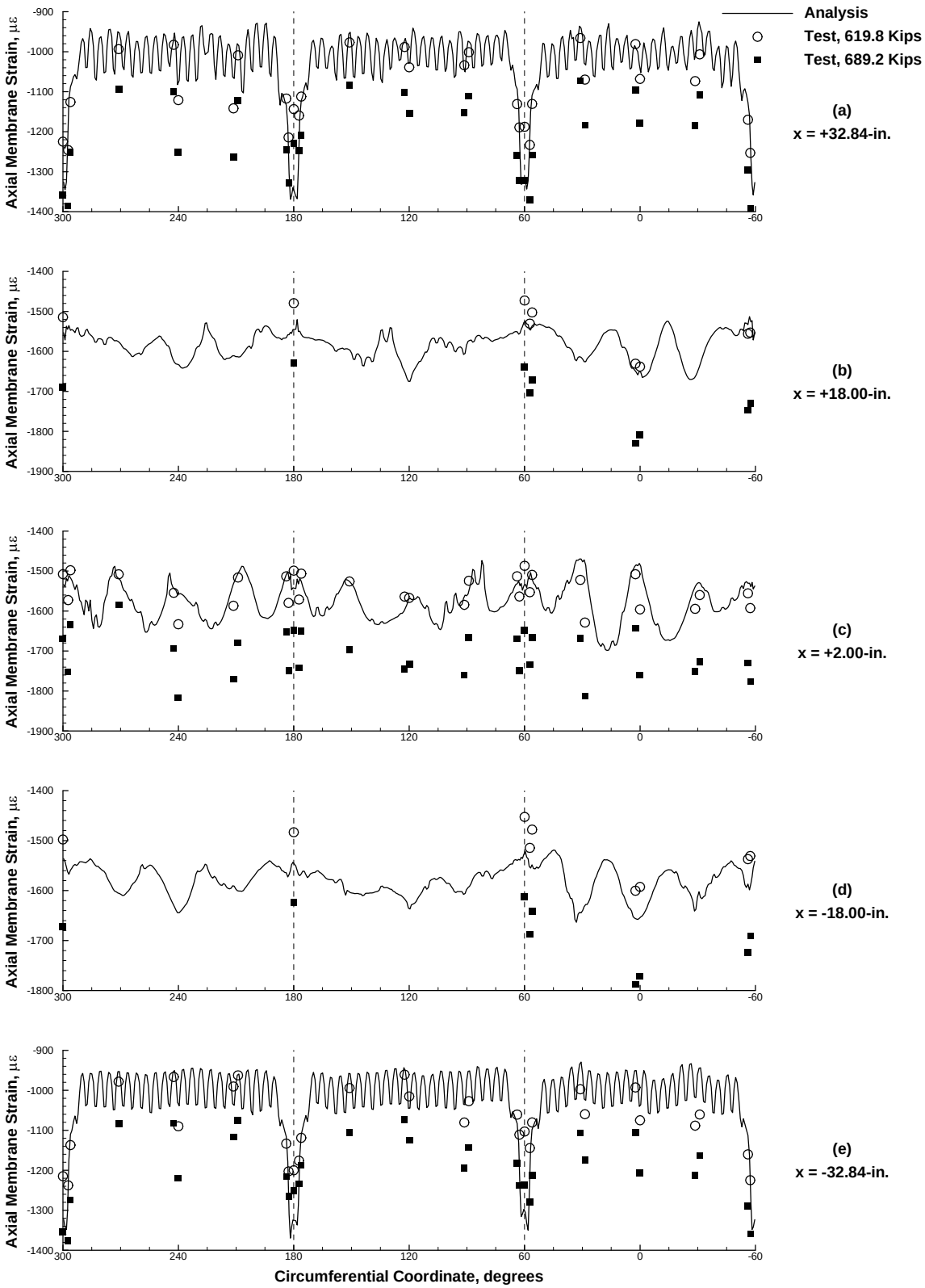

Figure 4.28. Predicted and measured axial membrane strain distribution around circumference, predicted buckling strains and measured data at 619.8 Kips (85.3% P_{cr}), measured buckling strains at 689.2 Kips (94.8% P_{cr}).

5.0 Concluding Remarks

Results from testing of the 8-foot-diameter Al-Li orthogrid-stiffened cylinder test article TA01 were presented. TA01 was the first in a series of nine subscale, integrally stiffened barrel tests defined in the SBKF test program. The test was conducted on November 19–21, 2008, at MSFC. The primary objectives of this test were to verify the performance of a new purpose-built test facility, and verify the adequacy of the test procedures, and test article design and analysis approach through detailed test and analysis correlation. To this end, selected results from the testing of TA01 were presented herein. First, descriptions of the test article design, fabrication, and test were presented and pretest analysis predictions were briefly described. Then, selected test results were presented and compared to pretest predictions.

Test Objectives and Success Criteria

All test objectives were successfully achieved and, for the most part, the test was executed as defined by the test plan and test procedure. Specifically, the test system and instrumentation operated as desired and the test article was tested to buckling and into the postbuckling range of loading. In addition, all test data necessary to verify the test article design and analysis approach were obtained; however, two minor discrepancies were identified in the data after testing. First, load line alignment verification measurements were made using a low-fidelity inclinometer, which did not have the accuracy necessary to verify the vertical alignment of the load lines to the specified tolerances. However, plum bob measurements and displacement and strain data obtained during the testing of TA01 indicated that the compression and bending loads were applied as desired and that no alignment-induced loads were present. Second, the high-speed DIC FOVs were not properly verified before the test and did not provide the full-field coverage as defined in the test plan. Fortunately, the high-speed DIC data that were obtained, and presented herein, were sufficient to characterize the initiation and propagation of the buckling response as required.

Test Results and Pretest Predictions

During testing, TA01 was subjected to uniform axial compression until buckling failure occurred. TA01 exhibited a linear prebuckling load-end-shortening response and achieved a maximum load of 689.2 Kips prior to buckling. Low-speed and high-speed digital image correlation displacement data indicated that buckling initiated as a single ellipse-shaped dimple in the cylinder wall and led to the sudden global collapse of the test article. The buckling and collapse of TA01 resulted in a significant reduction in axial load carrying capability and axial stiffness, and an initial postbuckling load level of 270 Kips. In addition, the test article exhibited material yielding due to the development of large-magnitude bending deformations in the shell wall during the buckling and collapse response.

Overall, the pretest predictions showed good correlation with the measured prebuckling, buckling, and postbuckling behavioral characteristics of TA01 and indicate that the modeling approach used can produce physically meaningful results that are suitable for pretest predictions and test planning.

In particular, the pretest predictions indicated similar load versus displacement and load versus strain response trends including an accurate representation of the axial stiffness and axial strain distribution around the circumference of the cylinder (±5% difference or better). In addition, the overall character of the prebuckling full-field radial displacements agreed well with the measured digital image correlation displacements including the development of a single ellipse-shaped dimple that initiated a transient buckling response. However, the predicted prebuckling radial displacement amplitudes were typically greater than the corresponding measured displacements. It is not known at this time what has caused the differences between the predicted and measured radial displacement amplitudes and buckling loads; however, it is likely that several of the modeling assumptions used in the pretest analysis may have some influence. For example, the fillets between the stiffeners and the skin and the fillets at the intersections between circumferential and longitudinal stiffeners (often referred to as nodes; see Section 2.2) were omitted from the model for simplicity. These fillet details would contribute additional bending and torsional stiffness to the stiffener and skin, which could reduce the predicted prebuckling radial displacements in the shell wall. In addition, the models assume idealized boundary conditions in which the ends of the test article are rigidly clamped in the attachment rings. The actual as-tested boundary conditions consisted of the test article potted in a low-melting-temperature alloy (see Section 2.3) that may allow some rotation of the test article in the attachment ring due to the relatively low stiffness of the potting and thus change the load introduction into the test article.

Future detailed analysis studies shall be performed to determine the effects of selected modeling assumptions on the predicted response and improve the test and analysis correlation. In addition, the effects of manufacturing tolerances associated with the as-built skin and stiffener dimensions should be investigated.

Archival Information

A complete listing of all test and analysis data, data files, and drawings is provided in Appendix A and includes archival directory names, file names and file format descriptions, and example data plots. All data, reports, drawings, and other supporting materials for TA01 design, fabrication, and testing is located in the SBKF_TA01_Archive directory in the SBKF Archive Directory on the NASA Langley central storage system (CSS).

6.0 References

1. Hilburger, M. W.; and Thornburgh, R. P.: "Shell Buckling Knockdown Factor Program SBKF-P2-CYL-TA01 Test Plan v1.2," 6 November 2008.
2. Roberts, M. G.: "Test and Checkout Procedure: Shell Buckling Knockdown Factor (SBKF) Test #1," TCP-ED30.1.MGR.102708, November 10, 2008.
3. Thornburgh, R. P.; and Hilburger, M. W.: "Design of Orthogrid Cylinder Test Articles for the Shell Buckling Knockdown Factor Assessment," NASA/TM–2010-216866 and ARL-TR-5122, November 2010.
4. Weingarten, V.; Seidi, P.; Peterson, J. P.; *Buckling of Thin-Walled Circular Cylinders.* NASA SP-8007, September 1965, revised August 1968.
5. Drawing No. 1167189, Revision B: "Panels Checkout Test Panel," NASA Langley Research Center, Hampton, Virginia, 19 March 2008.
6. Bjorkman, G.: "TD 6456F NASA LaRC Shell Buckling Knockdown Factor Assessment Support: Task 3 - Barrel Fabrication," ETTP-3913-08-001, June 11, 2008.
7. Drawing No. 1238206: "NESC Shell Buckling Test Barrel Assembly," NASA Langley Research Center, Hampton, Virginia, 17 March 2009.
8. Drawing No. 1238205, Revision B: "NESC Shell Buckling Test Panel Mounting Ring," NASA Langley Research Center, Hampton, Virginia, 17 March 2009.
9. Drawing 90M12370: "Test Assembly," NASA Marshall Space Flight Center, Huntsville, Alabama, 28 October 2008.
10. Drawing 90M12375: "Load Structure Assembly," NASA Marshall Space Flight Center, Huntsville, Alabama, 20 February 2008.
11. Drawing No. 1238207, Revision B: "NESC Shell Buckling Test Checkout Test Panel Instrumentation," NASA Langley Research Center, Hampton, Virginia, 22 July 2008.
12. Rankin, C. C.; Brogan, F. A.; Loden, W. A.; Cabiness, H. D.; *STAGS Users Manual, Version 5.0.* Lockheed Martin Missiles & Space Co., Inc., Advanced Technology Center, Report LMSC P032594, January 2005.
13. Thornburgh, R. P.; and Hilburger, M. W.: "Pre-Test Analysis Predictions for the Shell Buckling Knockdown Factor Checkout Tests – TA01 and TA02," NASA/TM–2011-216875 ARL-TR-5123, January 2011.
14. Hastings, K.; and Malone, T. W.: "Design Allowables Handbook for Aluminum-Lithium 2195 Plates, Extrusions, Forgings, & Welds," MSFC-HDBK-3513, December 2007.

Appendix A Archival Information

All electronic files associated with the testing of TA01 are stored in the SBKF Data Archive located on the NASA Langley Central Storage System (CSS) and the NESC NASA Safety Center Knowledge Now (NSCKN) storage site. These files include all test data, manufacturing plan, test plan, test procedure, test article and test facility drawings, quality assurance reports and data, finite element results, and selected processed data and plots. The electronic files are listed in this section along with a short description of the format of the files. File names and directory paths are indicated in Arial font throughout the Appendix for clarity.

Plans, Procedures, Drawings, and Reports

TA01 plans, procedures, drawing files, and reports are found in SBKF_TestData_Archive > TA01 > TA01_Docs. Files include:

Plans and Procedures

TA01 Test Plan: SBKF-P2-CYL-SD01-TestPlan_v1.2.pdf
TA01 Test Procedure: TCP-ED30.1-MGR-111008.pdf
TA01 Manufacturing Plan: ETTP-3913-08-001.pdf

Drawings

Barrel Panel Design Drawing: Drawing_1167189_Rev._B.pdf
Barrel Test Article Attachment Ring Drawing: Drawing_1238205_Rev._A.pdf
Barrel Test Article Assembly Drawing: Drawing_1238206_Rev._A.pdf
Instrumentation Pattern Drawing: Drawing_1238207_Rev._B.pdf
Load Structure Assembly Drawing: Drawing_90M12375.pdf
Test Assembly Drawing: Drawing_90M12370.pdf

Quality and Manufacturing Reports

Material Requirements Report: EC-012200_STM11A1-4.pdf
Material Qualification Report: SBKF_Material_Qualification.pdf

TA01 Measured Geometry

The initial geometry of TA01 was measured after fabrication was complete and before instrumentation was installed. The raw data were provided in global Cartesian coordinates and was converted to cylindrical coordinates. The data were then fit to a best-fit circular cylinder and the deviations from the perfect OML cylinder radius were calculated and denoted by the variable *imp* as shown in Fig. 4.1. The resulting test-article geometry data are reported in x, θ, *imp* column format, where x and θ are the OML coordinates as defined in Fig. 4.2 and *imp* is the measured deviation. The measured data are found in SBKF_ TestData Archive > TA01 > TA01_MeasuredGeometry_Data. Files include:

TA01 measured imperfection data file: TA01_cmm.dat
Fortran subroutine used to input the measured imperfection data into the FEM: TA01_dimp.F
TA01 measured imperfection plot (Fig. 2.6): TA01_imp.jpg

Test Data

Test data for all load sequences conducted during the testing of TA01 have been archived. Archived test data and plots for Load Sequence 5 (LS_5) are described in this section; however, similar data are available for the other load sequences in the archives and follows a similar directory and file name format. The data can be found in the following directories:

Load Sequence 1 Data: SBKF_TestData_Archive > TA01 > TA01_LS_1
Load Sequence 2 Data: SBKF_TestData_Archive > TA01 > TA01_LS_2
Load Sequence 3 Data: SBKF_TestData_Archive > TA01 > TA01_LS_3
Load Sequence 4 Data: SBKF_TestData_Archive > TA01 > TA01_LS_4
Load Sequence 5 Data: SBKF_TestData_Archive > TA01 > TA01_LS_5

Raw Test Data Files

The raw test data for LS_5 are in Microsoft® Excel® format and in standard text format in the SBKF Data Archive in the following directory:

SBKF_ TestData Archive > TA01 > TA01_LS5 > TA01_LS5_Raw_Test_Data >

Excel® files:

TA01_LS5_Raw_Test_Data-EU1of3-11-20-2008.xls
TA01_LS5_Raw_Test_Data-EU2of3-11-20-2008.xls
TA01_LS5_Raw_Test_Data-EU3of3-11-20-2008.xls
TA01_LS5_Raw_Test_Data-LPS1of3-11-20-2008.xls
TA01_LS5_Raw_Test_Data-LPS2of3-11-20-2008.xls
TA01_LS5_Raw_Test_Data-LPS3of3-11-20-2008.xls

Text files:

TA01_LS5_Raw_Test_Data-EU1of3-11-20-2008.txt
TA01_LS5_Raw_Test_Data-EU2of3-11-20-2008.txt
TA01_LS5_Raw_Test_Data-EU3of3-11-20-2008.txt
TA01_LS5_Raw_Test_Data-LPS1of3-11-20-2008.txt
TA01_LS5_Raw_Test_Data-LPS2of3-11-20-2008.txt
TA01_LS5_Raw_Test_Data-LPS3of3-11-20-2008.txt

The "EU" (Engineering Units) series files are full test data sets and are separated into three files due to the size limitations of the software. The "LPS" (Load Point Scans) series files contain the tagged scan data. Tagged scan data refers to a subset of the full data set in which data from all channels are saved at specific times during the test, typically at prescribed load levels defined in the test plan and after prominent response events during the test such as buckling. All data channels are clearly labeled in the files and are consistent with the name and labeling convention in drawings and other related documents.

Processed Test Data Files and X-Y Data and Plots

The raw test data have been processed into usable data for plotting and correlation with predicted results. The corresponding analysis results were obtained from nonlinear finite-element analyses (Ref. 13) and were taken from the appropriate locations in the cylinder model to correlate directly with the test data. The processed test data files and corresponding nonlinear finite-element analysis data files are provided in Tecplot format

(.plt, similar to tab-delimited text) and are listed here along with selected data plots in .pdf format for quick reference. In addition, Tecplot layout files (.lay) are provided and can be used to plot the test and analysis data in Tecplot. All files are located in the SBKF Data Archive in the following directory:

SBKF_TestData _Archive > TA01 > TA01_LS5 > TA01_LS5_Formatted_ Data _Files.

Data files:
Test data: TA01_LS5_Experiment.plt (also called TA01_LS5_Experiment_20130712-001.dat)
Predicted STAGS nonlinear transient analysis data: TA01_LS5_STAGS_data.plt (also called ta1_ax12_Stags_analysis_20090117-1.dat)
Predicted displacement data: TA01_LS5_STAGS_Disp.data.plt (merged with above file)

Tecplot Layout files:
Normalized axial load P/P_{cr} versus a back-to-back strain gage pair: TA01_LS5_B2B_Strains.lay
Normalized axial load P/P_{cr} versus a displacement transducer: TA01_LS5_Displacements.lay

Processed Tagged Scan Data Files and Plots

Predicted and measured axial strain distributions around the circumference of the test article have been obtained from five axial locations, x = –32.84-in., –18.00-in., –2.00-in., 18.00-in., and 32.84-in. (see Figs. 4.28–4.31). These data are available for several tagged scan points that correspond to normalized load levels of P/P_{cr} = 0.220, 0.440, 0.799 and limit loads (for both test and analysis). P_{cr} corresponds to the predicted linear bifurcation buckling load for the corresponding geometrically perfect, uniform cylinder subjected to compression and equals 726,800 lb. A summary of the tag scan data files is given in Table A3. All files are located in the SBKF Data Archive in the following directory: SBKF_TestData _Archive > TA01 > TA01_LS5 > TA01_LS5_Formatted_Data_Files > TA01_LS5_Tagged_Scans.

Digital Image Correlation Data Files and Contour Plots

A subset of the total DIC images were processed into data due to the extensive number of images collected during the testing. However, all images, calibration, and data files have been retained for future processing if necessary. Selected files for DIC data and predicted data are listed in Table A.4 and include finite-element model analysis load step, DIC photo number, raw test data scan number, and corresponding data file names. The raw image files (.tiff files), processed digital image correlation data are located in the SBKF Data Archive in the following directory:

SBKF_TestData_Archive > TA01 > TA01_LS5 > TA01_LS5_DIC-3D_Data.

Within the TA01_LS5_DIC-3D_Data directory there is a directory for each DIC system following the convention:

Test Article name-DIC system number-DIC system location-load sequence number (e.g., TA01-sys1-east-LS5)

Image files and output files within each directory have image number and camera number.

Examples are:

TA01-sys1-east-LS5-0001_0.tif
TA01-sys2-north-LS5-0123_1.tif
TA01-sys4-west-LS5-0024_0.out (processing output file)

VIC project files and data reports are also included such as:

TA01-sys5-south-LS5.z3d (VIC-3D project file)
TA01-sys5-south-LS5-report.csv (projection error report file)
TA01-sys1-east-LS5.csv (analog data file)

Similar calibration data and files are included and have a "-cal" appended after the LS# in the directory and file name.

Image files (.jpg) containing contour plots of the *u*, *v*, and *w* displacements were generated (e.g., Figs 4.9–4.16). The prebuckling images are stored on the SBKF Data Archive in the following directory: SBKF_TestData _Archive > TA01 > TA01_LS5 > TA01_LS5_DIC-3D_Data > TA01_LS5_DIC_Prebuckling_Plots. The postbuckling images are stored on the SBKF Data Archive in the following directory: SBKF_TestData_Archive > TA01 > TA01_LS5 > TA01_LS5_DIC-3D_Data > TA01_LS5_DIC_Postbuckling_Plots.

High-speed video info

High-speed camera files are stored on the SBKF Data Archive in the following directory: SBKF_TestData_Archive > TA01 > TA01_LS5 > TA01_LS5_DIC-3D_Data > TA01_LS5_High-Speed_Video.

The directory and file naming convention is the same as the low-speed DIC systems as described above except the sys# portion of the file name will be replaced with a hscam#. The project file for the single cameras will be a *.z2d instead of a *.z3d file.

Photos and Video

Low-resolution and high-resolution photos and video of the test setup and test control room were taken November 19–21 2008 during testing. The photos can be found in the following directory: SBKF_TestData _Archive > TA01 > Photos in the following sub-directories:

4619-11-08-lowres
4619-11-19-08
4619-11-20-08
4619-11-21-08
4619-11-21-08-posttest

Video is found in the following directory: SBKF_TestData _Archive >TA01 > Video.

Finite-Element Models and Analysis Data

Finite-Element Models and Analysis Data are found in the following directory: SBKF_TestData Archive >TA01 > TA01_LS5 > TA01_LS5_FEM

Model input file: TA01_LS5.inp (also known as ta1_ax12p.inp)
Model run file: TA01_LS5.bin (also known as ta1_ax12p.bin)
Geometric imperfection data: TA01_imp.dat (also known as cmm.dat)
Geometry definition subroutine: dimp.F (also known as dimp.F)
Wall definition subroutine: wall.F
Subroutine to use with initial geometric imperfection data: cmm.F

Table A1. Electronic Displacement Indicator (EDI) Locations

EDI	EDI ID	Angular Location, deg.	x, in.	Component Location	Orientation	IML/OML Location
239	D239AA	0°	36.313	Top Attachment Ring	Axial	IML
240	D240AA	90°	36.313	Top Attachment Ring	Axial	IML
241	D241AA	180°	36.313	Top Attachment Ring	Axial	IML
242	D242AA	270°	36.313	Top Attachment Ring	Axial	IML
243	D243BR	60°	0.00	Panel A/B Weld Land	Radial	IML
244	D244BR	180°	0.00	Panel B/C Weld Land	Radial	IML
245	D245BR	300°	0.00	Panel C/A Weld Land	Radial	IML
246	D246CR	0°	0.00	Panel A	Radial	IML
247	D247CR	120°	0.00	Panel B	Radial	IML
248	D248CR	240°	0.00	Panel C	Radial	IML
249	D249DR	60°	-29.375	Panel A/B Weld Land	Radial	IML
250	D250ER	0°	-29.375	Panel A	Radial	IML
251	D251FR	0°	36.313	Top Attachment Ring	Radial	IML
252	D252FR	120°	36.313	Top Attachment Ring	Radial	IML
253	D253FR	240°	36.313	Top Attachment Ring	Radial	IML
254	D254FR	0°	-36.313	Bottom Attachment Ring	Radial	IML
255	D255FR	120°	-36.313	Bottom Attachment Ring	Radial	IML
256	D256FR	240°	-36.313	Bottom Attachment Ring	Radial	IML
257	D257GH	0°	36.313	Top Attachment Ring	Tangential	OML
258	D258GH	0°	-36.313	Bottom Attachment Ring	Tangential	OML
259	D259AA	0°	-36.313	Bottom Attachment Ring	Axial	IML
260	D260AA	90°	-36.313	Bottom Attachment Ring	Axial	IML
261	D261AA	180°	-36.313	Bottom Attachment Ring	Axial	IML
262	D262AA	270°	-36.313	Bottom Attachment Ring	Axial	IML
263	D263AA	0°	(1)	(1)	Axial	IML
264	D264AA	90°	(2)	(2)	Axial	IML
265	D265AA	180°	(3)	(3)	Axial	IML
266	D266AA	270°	(4)	(4)	Axial	IML

(1) $\delta_{D263AA} = \delta_{D239AA} - \delta_{D259AA}$
(2) $\delta_{D264AA} = \delta_{D240AA} - \delta_{D260AA}$
(3) $\delta_{D265AA} = \delta_{D241AA} - \delta_{D261AA}$
(4) $\delta_{D266AA} = \delta_{D242AA} - \delta_{D262AA}$

Table A2. Strain Gage Locations and Orientations for TA01

OML GAGE NUMBER	OML GAGE ID	IML GAGE NUMBER	IML GAGE ID	HOOP DIMENSION, (in.)	AXIAL DIMENSION, (in.)	PANEL	LOCATION	ORIENTATION
1	001OWA	56	056IWA	50.27	-32.84	A	Weld	Axial
2	002ORA	57	057IRA	48.00	-32.84	A	Stiffener	Axial
3a	003OSA	58a	058ISA	47.00	-32.84	A	Pocket	Axial
3b	003OSH	58b	058ISH	47.00	-32.84	A	Pocket	Hoop
4	004OSA	59	059ISA	26.00	-32.84	A	Pocket	Axial
5	005ORA	60	060IRA	24.00	-32.84	A	Stiffener	Axial
6a	006OSA	61a	061ISA	2.00	-32.84	A	Pocket	Axial
6b	006OSH	61b	061ISH	2.00	-32.84	A	Pocket	Hoop
7	007ORA	62	062IRA	0.00	-32.84	A	Stiffener	Axial
8	008ORA	63	063IRA	-24.00	-32.84	A	Stiffener	Axial
9	009OSA	64	064ISA	-26.00	-32.84	A	Pocket	Axial
10a	010OSA	65a	065ISA	-47.00	-32.84	A	Pocket	Axial
10b	010OSH	65b	065ISH	-47.00	-32.84	A	Pocket	Hoop
11	011ORA	66	066IRA	-48.00	-32.84	A	Stiffener	Axial
12	012OSH	67	067IRH	47.00	-32.00	A	Rib	Hoop
13	013OSH	68	068IRH	2.00	-32.00	A	Rib	Hoop
14	014OSH	69	069IRH	-47.00	-32.00	A	Rib	Hoop
15	015OWA	70	070IWA	50.27	-18.00	A	Weld	Axial
16	016ORA	71	071IRA	48.00	-18.00	A	Stiffener	Axial
17	017OSA	72	072ISA	47.00	-18.00	A	Pocket	Axial
18	018OSA	73	073ISA	2.00	-18.00	A	Pocket	Axial
19	019ORA	74	074IRA	0.00	-18.00	A	Stiffener	Axial
20	020OSA	75	075ISA	-47.00	-18.00	A	Pocket	Axial
21	021ORA	76	076IRA	-48.00	-18.00	A	Stiffener	Axial
22	022ORH	77	077IRH	47.00	0.00	A	Rib	Hoop
23	023ORH	78	078IRH	-47.00	0.00	A	Rib	Hoop
24	024OWA	79	079IWA	50.27	2.00	A	Weld	Axial
25	025ORA	80	080IRA	48.00	2.00	A	Stiffener	Axial

Table A2. Continued

OML GAGE NUMBER	OML GAGE ID	IML GAGE NUMBER	IML GAGE ID	HOOP DIMENSION, (in.)	AXIAL DIMENSION, (in.)	PANEL	LOCATION	ORIENTATION
26a	026OSA	81a	081ISA	47.00	2.00	A	Pocket	Axial
26b	026OSH	81b	081ISH	47.00	2.00	A	Pocket	Hoop
27	027OSA	82	082ISA	26.00	2.00	A	Pocket	Axial
28	028ORA	83	083IRA	24.00	2.00	A	Stiffener	Axial
29	029OSA	84	084ISA	2.00	2.00	A	Pocket	Axial
30	030ORA	85	085IRA	0.00	2.00	A	Stiffener	Axial
31	031ORA	86	086IRA	-24.00	2.00	A	Stiffener	Axial
32	032OSA	87	087ISA	-26.00	2.00	A	Pocket	Axial
33a	033OSA	88a	088ISA	-47.00	2.00	A	Pocket	Axial
33b	033OSH	88b	088ISH	-47.00	2.00	A	Pocket	Hoop
34	034ORA	89	089IRA	-48.00	2.00	A	Stiffener	Axial
35	035OWA	90	090IWA	50.27	18.00	A	Weld	Axial
36	036ORA	91	091IRA	48.00	18.00	A	Stiffener	Axial
37	037OSA	92	092ISA	47.00	18.00	A	Pocket	Axial
38	038OSA	93	093ISA	2.00	18.00	A	Pocket	Axial
39	039ORA	94	094IRA	0.00	18.00	A	Stiffener	Axial
40	040OSA	95	095ISA	-47.00	18.00	A	Pocket	Axial
41	041ORA	96	096IRA	-48.00	18.00	A	Stiffener	Axial
42	042ORH	97	097IRH	47.00	32.00	A	Rib	Hoop
43	043ORH	98	098IRH	2.00	32.00	A	Rib	Hoop
44	044ORH	99	099IRH	-47.00	32.00	A	Rib	Hoop
45	045OWA	100	100IWA	50.27	32.84	A	Weld	Axial
46	046ORA	101	101IRA	48.00	32.84	A	Stiffener	Axial
47a	047OSA	102a	102ISA	47.00	32.84	A	Pocket	Axial
47b	047OSH	102b	102ISH	47.00	32.84	A	Pocket	Hoop
48	048OSA	103	103ISA	26.00	32.84	A	Pocket	Axial
49	049ORA	104	104IRA	24.00	32.84	A	Stiffener	Axial
50a	050OSA	105a	105ISA	2.00	32.84	A	Pocket	Axial

Table A2. Continued

OML GAGE NUMBER	OML GAGE ID	IML GAGE NUMBER	IML GAGE ID	HOOP DIMENSION, (in.)	AXIAL DIMENSION, (in.)	PANEL	LOCATION	ORIENTATION
50b	050OSH	105b	105ISH	2.00	32.84	A	Pocket	Hoop
51	051ORA	106	106IRA	0.00	32.84	A	Stiffener	Axial
52	052ORA	107	107IRA	-24.00	32.84	A	Stiffener	Axial
53	053OSA	108	108ISA	-26.00	32.84	A	Pocket	Axial
54a	054OSA	109a	109ISA	-47.00	32.84	A	Pocket	Axial
54b	054OSH	109b	109ISH	-47.00	32.84	A	Pocket	Hoop
55	055ORA	110	110IRA	-48.00	32.84	A	Stiffener	Axial
111	111OWA	143	143IWA	50.27	-32.84	B	Weld	Axial
112	112ORA	144	144IRA	48.00	-32.84	B	Stiffener	Axial
113	113OSA	145	145ISA	47.00	-32.84	B	Pocket	Axial
114	114OSA	146	146ISA	26.00	-32.84	B	Pocket	Axial
115	115OSA	147	147ISA	2.00	-32.84	B	Pocket	Axial
116	116ORA	148	148IRA	0.00	-32.84	B	Stiffener	Axial
117	117ORA	149	149IRA	-24.00	-32.84	B	Stiffener	Axial
118	118OSA	150	150ISA	-26.00	-32.84	B	Pocket	Axial
119	119OSA	151	151ISA	-47.00	-32.84	B	Pocket	Axial
120	120ORA	152	152IRA	-48.00	-32.84	B	Stiffener	Axial
121	121OWA	153	153IWA	50.27	-18.00	B	Weld	Axial
122	122OWA	154	154IWA	50.27	2.00	B	Weld	Axial
123	123ORA	155	155IRA	48.00	2.00	B	Stiffener	Axial
124	124OSA	156	156ISA	47.00	2.00	B	Pocket	Axial
125	125OSA	157	157ISA	26.00	2.00	B	Pocket	Axial
126	126OSA	158	158ISA	2.00	2.00	B	Pocket	Axial
127	127ORA	159	159IRA	0.00	2.00	B	Stiffener	Axial
128	128ORA	160	160IRA	-24.00	2.00	B	Stiffener	Axial
129	129OSA	161	161ISA	-26.00	2.00	B	Pocket	Axial
130	130OSA	162	162ISA	-47.00	2.00	B	Pocket	Axial
131	131ORA	163	163IRA	-48.00	2.00	B	Stiffener	Axial

Table A2. Continued

OML GAGE NUMBER	OML GAGE ID	IML GAGE NUMBER	IML GAGE ID	HOOP DIMENSION, (in.)	AXIAL DIMENSION, (in.)	PANEL	LOCATION	ORIENTATION
132	132OWA	164	164IWA	50.27	18.00	B	Weld	Axial
133	133OWA	165	165IWA	50.27	32.84	B	Weld	Axial
134	134ORA	166	166IRA	48.00	32.84	B	Stiffener	Axial
135	135OSA	167	167ISA	47.00	32.84	B	Pocket	Axial
136	136OSA	168	168ISA	26.00	32.84	B	Pocket	Axial
137	137OSA	169	169ISA	2.00	32.84	B	Pocket	Axial
138	138ORA	170	170IRA	0.00	32.84	B	Stiffener	Axial
139	139ORA	171	171IRA	-24.00	32.84	B	Stiffener	Axial
140	140OSA	172	172ISA	-26.00	32.84	B	Pocket	Axial
141	141OSA	173	173ISA	-47.00	32.84	B	Pocket	Axial
142	142ORA	174	174IRA	-48.00	32.84	B	Stiffener	Axial
175	175OWA	207	207IWA	50.27	-32.84	C	Weld	Axial
176	176ORA	208	208IRA	48.00	-32.84	C	Stiffener	Axial
177	177OSA	209	209ISA	47.00	-32.84	C	Pocket	Axial
178	178OSA	210	210ISA	26.00	-32.84	C	Pocket	Axial
179	179OSA	211	211ISA	2.00	-32.84	C	Pocket	Axial
180	180ORA	212	212IRA	0.00	-32.84	C	Stiffener	Axial
181	181ORA	213	213IRA	-24.00	-32.84	C	Stiffener	Axial
182	182OSA	214	214ISA	-26.00	-32.84	C	Pocket	Axial
183	183OSA	215	215ISA	-47.00	-32.84	C	Pocket	Axial
184	184ORA	216	216IRA	-48.00	-32.84	C	Stiffener	Axial
185	185OWA	217	217IWA	50.27	-18.00	C	Weld	Axial
186	186OWA	218	218IWA	50.27	2.00	C	Weld	Axial
187	187ORA	219	219IRA	48.00	2.00	C	Stiffener	Axial
188	188OSA	220	220ISA	47.00	2.00	C	Pocket	Axial
189	189OSA	221	221ISA	26.00	2.00	C	Pocket	Axial
190	190OSA	222	222ISA	2.00	2.00	C	Pocket	Axial
191	191ORA	223	223IRA	0.00	2.00	C	Stiffener	Axial

Table A2. Concluded

OML GAGE NUMBER	OML GAGE ID	IML GAGE NUMBER	IML GAGE ID	HOOP DIMENSION, (in.)	AXIAL DIMENSION, (in.)	PANEL	LOCATION	ORIENTATION
192	192ORA	224	224IRA	-24.00	2.00	C	Stiffener	Axial
193	193OSA	225	225ISA	-26.00	2.00	C	Pocket	Axial
194	194OSA	226	226ISA	-47.00	2.00	C	Pocket	Axial
195	195ORA	227	227IRA	-48.00	2.00	C	Stiffener	Axial
196	196OWA	228	228IWA	50.27	18.00	C	Weld	Axial
197	197OWA	229	229IWA	50.27	32.84	C	Weld	Axial
198	198ORA	230	230IRA	48.00	32.84	C	Stiffener	Axial
199	199OSA	231	231ISA	47.00	32.84	C	Pocket	Axial
200	200OSA	232	232ISA	26.00	32.84	C	Pocket	Axial
201	201OSA	233	233ISA	2.00	32.84	C	Pocket	Axial
202	202ORA	234	234IRA	0.00	32.84	C	Stiffener	Axial
203	203ORA	235	235IRA	-24.00	32.84	C	Stiffener	Axial
204	204OSA	236	236ISA	-26.00	32.84	C	Pocket	Axial
205	205OSA	237	237ISA	-47.00	32.84	C	Pocket	Axial
206	206ORA	238	238IRA	-48.00	32.84	C	Stiffener	Axial

Table A3. Data Files to Generate X-Y Plots of Axial Membrane Strain Distribution Around the Test Article Circumference (see Figures 4.27–4.30)

STAGS Load Step	P/P_{cr}[2]	Test Tag Scan No.	Axial Location, in.	STAGS Nonlinear Analysis(1)	Test
9	0.440	4257	-32.84	TA01_LS5_STAGS_Load_Step_09_-32.84.dat	TA01_LS5_Test_membrane_Step_09_4257_x-32.84.plt
			-18.00	TA01_LS5_STAGS_Load_Step_09_-18.00.dat	TA01_LS5_Test_membrane_Step_09_4257_x-18.00.plt
			2.00	TA01_LS5_STAGS_Load_Step_09_+02.00.dat	TA01_LS5_Test_membrane_Step_09_4257_x+02.00.plt
			18.00	TA01_LS5_STAGS_Load_Step_09_+18.00.dat	TA01_LS5_Test_membrane_Step_09_4257_x+18.00.plt
			32.84	TA01_LS5_STAGS_Load_Step_09_+32.84.dat	TA01_LS5_Test_membrane_Step_09_4257_x+32.84.plt
10	0.550	4609	-32.84	TA01_LS5_STAGS_Load_Step_10_-32.84.dat	TA01_LS5_Test_membrane_Step_10_4609_x-32.84.plt
			-18.00	TA01_LS5_STAGS_Load_Step_10_-18.00.dat	TA01_LS5_Test_membrane_Step_10_4609_x-18.00.plt
			2.00	TA01_LS5_STAGS_Load_Step_10_+02.00.dat	TA01_LS5_Test_membrane_Step_10_4609_x+02.00.plt
			18.00	TA01_LS5_STAGS_Load_Step_10_+18.00.dat	TA01_LS5_Test_membrane_Step_10_4609_x+18.00.plt
			32.84	TA01_LS5_STAGS_Load_Step_10_+32.84.dat	TA01_LS5_Test_membrane_Step_10_4609_x+32.84.plt
15	0.799	6308	-32.84	TA01_LS5_STAGS_Load_Step_15_-32.84.dat	TA01_LS5_Test_membrane_Step_15_6308_x-32.84.plt
			-18.00	TA01_LS5_STAGS_Load_Step_15_-18.00.dat	TA01_LS5_Test_membrane_Step_15_6308_x-18.00.plt
			2.00	TA01_LS5_STAGS_Load_Step_15_+02.00.dat	TA01_LS5_Test_membrane_Step_15_6308_x+02.00.plt
			18.00	TA01_LS5_STAGS_Load_Step_15_+18.00.dat	TA01_LS5_Test_membrane_Step_15_6308_x+18.00.plt
			32.84	TA01_LS5_STAGS_Load_Step_15_+32.84.dat	TA01_LS5_Test_membrane_Step_15_6308_x+32.84.plt
18	0.853[3]	6537[4]	-32.84	TA01_LS5_STAGS_Load_Step_18_-32.84.dat	TA01_LS5_Test_membrane_Step_18_6537_x-32.84.plt
			-18.00	TA01_LS5_STAGS_Load_Step_18_-18.00.dat	TA01_LS5_Test_membrane_Step_18_6537_x-18.00.plt
			2.00	TA01_LS5_STAGS_Load_Step_18_+02.00.dat	TA01_LS5_Test_membrane_Step_18_6537_x+02.00.plt
			18.00	TA01_LS5_STAGS_Load_Step_18_+18.00.dat	TA01_LS5_Test_membrane_Step_18_6537_x+18.00.plt
			32.84	TA01_LS5_STAGS_Load_Step_18_+32.84.dat	TA01_LS5_Test_membrane_Step_18_6537_x+32.84.plt
N/A	0.948[5]	6831	-32.84	N/A	TA01_LS5_Test_membrane_Step_18_6831_x-32.84.plt
			-18.00	N/A	TA01_LS5_Test_membrane_Step_18_6831_x-18.00.plt
			2.00	N/A	TA01_LS5_Test_membrane_Step_18_6831_x+02.00.plt
			18.00	N/A	TA01_LS5_Test_membrane_Step_18_6831_x+18.00.plt
			32.84	N/A	TA01_LS5_Test_membrane_Step_18_6831_x+32.84.plt

(1) Tecplot format.
(2) P_{cr} = 726,800-lb.
(3) Predicted limit load from STAGS nonlinear analysis.
(4) Test data tag scan corresponding to predicted limit load.

(5) Measured limit load from test.

Table A.4. Files Used to Generate Color Contour Plots (Tecplot Format)

Test Article 1	STAGS Load Step	DIC Photo Number From Test	Tagged Scan Number From Test	P/P_{cr} (1)	STAGS Data File (for contour plots)	DIC Data File From Test (for contour plots)
Load Sequence 5		6	663			SBKF-TA01-LS5-0006.dat
		22	3202			SBKF-TA01-LS5-0022.dat
	2	47	3452	0.1104	TA01_LS5_STAGS_Nonlinear_Load_Step_02.dat	SBKF-TA01-LS5-0047.dat
	6	70	3686	0.2202	TA01_LS5_STAGS_Nonlinear_Load_Step_06.dat	SBKF-TA01-LS5-0070.dat
	8	93	3919	0.3301	TA01_LS5_STAGS_Nonlinear_Load_Step08.dat	SBKF-TA01-LS5-0093.dat
	9	127	4257	0.4397	TA01_LS5_STAGS_Nonlinear_Load_Step09.dat	SBKF-TA01-LS5-0127.dat
	10	163	4609	0.5500	TA01_LS5_STAGS_Nonlinear_Load_Step10.dat	SBKF-TA01-LS5-0163.dat
	11	184	4823	0.6048	TA01_LS5_STAGS_Nonlinear_Load_Step11.dat	SBKF-TA01-LS5-0184.dat
		258				SBKF-TA01-LS5-0258.dat
	12	271	5698	0.6597	TA01_LS5_STAGS_Nonlinear_Load_Step12.dat	SBKF-TA01-LS5-0271.dat
	13	289	5871	0.6994	TA01_LS5_STAGS_Nonlinear_Load_Step13.dat	SBKF-TA01-LS5-0289.dat
	14	310	6088	0.7494	TA01_LS5_STAGS_Nonlinear_Load_Step14.dat	SBKF-TA01-LS5-0310.dat
	15	332	6308	0.7993	TA01_LS5_STAGS_Nonlinear_Load_Step15.dat	SBKF-TA01-LS5-0332.dat
		365	6632	0.8992		SBKF-TA01-LS5-0365.dat
		377				SBKF-TA01-LS5-0377.dat
		378	6831	0.9483		SBKF-TA01-LS5-0378.dat
		384	6940	0.4018		SBKF-TA01-LS5-0384.dat
		395				SBKF-TA01-LS5-0395.dat
		550	9809	0.3462		SBKF-TA01-LS5-0550.dat
		725	10238	-0.0009		SBKF-TA01-LS5-0725.dat
		741	10663	0.0476		SBKF-TA01-LS5-0741.dat
		798	10891	0.0536		SBKF-TA01-LS5-0798.dat

(1) P_{cr} = 726,800-lb.

REPORT DOCUMENTATION PAGE

Form Approved
OMB No. 0704-0188

1. REPORT DATE *(DD-MM-YYYY)*	2. REPORT TYPE	3. DATES COVERED *(From - To)*
01- 08 - 2015	Technical Publication	

4. TITLE AND SUBTITLE
Buckling Test Results from the 8-Foot-Diameter Orthogrid-Stiffened Cylinder Test Article TA01
Test Dates: 19?21 November 2008

5a. CONTRACT NUMBER

5b. GRANT NUMBER

5c. PROGRAM ELEMENT NUMBER

6. AUTHOR(S)
Hilburger, Mark W.; Waters, W. Allen, Jr.; Haynie, Waddy T.

5d. PROJECT NUMBER

5e. TASK NUMBER

5f. WORK UNIT NUMBER
869021.04.07.01.13

7. PERFORMING ORGANIZATION NAME(S) AND ADDRESS(ES)
NASA Langley Research Center
Hampton, VA 23681-2199

8. PERFORMING ORGANIZATION REPORT NUMBER
L-20490

9. SPONSORING/MONITORING AGENCY NAME(S) AND ADDRESS(ES)
National Aeronautics and Space Administration
Washington, DC 20546-0001

10. SPONSOR/MONITOR'S ACRONYM(S)
NASA

11. SPONSOR/MONITOR'S REPORT NUMBER(S)
NASA/TP-2015-218785

12. DISTRIBUTION/AVAILABILITY STATEMENT
Unclassified - Unlimited
Subject Category 39 Structural Mechanics
Availability: NASA STI Program (757) 864-9658

13. SUPPLEMENTARY NOTES

14. ABSTRACT

Results from the testing of cylinder test article SBKF-P2-CYL-TA01 (referred to herein as TA01) are presented. TA01 is an 8-foot-diameter (96-inches), 78.0-inch-long, aluminum-lithium (Al-Li), orthogrid-stiffened cylindrical shell similar to those used in current state-of-the-art launch-vehicle structures and was designed to exhibit global buckling when subjected to compression loads. The testing was conducted at the Marshall Space Flight Center (MSFC), November 19-21, 2008, in support of the Shell Buckling Knockdown Factor (SBKF) Project. The test was used to verify the performance of a newly constructed buckling test facility at MSFC and to verify the test article design and analysis approach used by the SBKF project researchers.

15. SUBJECT TERMS
Orthogrid, Cylinder, Buckling, Testing, Design, Knockdown Factors

16. SECURITY CLASSIFICATION OF:			17. LIMITATION OF ABSTRACT	18. NUMBER OF PAGES	19a. NAME OF RESPONSIBLE PERSON
a. REPORT	b. ABSTRACT	c. THIS PAGE			STI Help Desk (email: help@sti.nasa.gov)
					19b. TELEPHONE NUMBER *(Include area code)*
U	U	U	UU	72	(443) 757-5802